

PEPTIDOGLYCAN BINDING BY PGP2 AND APE1
DETERMINES CAMPYLOBACTER JEJUNI HELICAL CELL SHAPE

by

Chang Sheng-Huei Lin

M.Sc., National Cheng Kung University, 2012

A DISSERTATION SUBMITTED IN PARTIAL FULFILLMENT OF
THE REQUIREMENTS FOR THE DEGREE OF

DOCTOR OF PHILOSOPHY

in

THE FACULTY OF GRADUATE AND POSTDOCTORAL STUDIES
(Microbiology and Immunology)

THE UNIVERSITY OF BRITISH COLUMBIA
(Vancouver)

August 2021

© Chang Sheng-Huei Lin, 2021

The following individuals certify that they have read, and recommend to the Faculty of Graduate and Postdoctoral Studies for acceptance, the dissertation entitled:

Peptidoglycan binding by Pgp2 and Ape1 determines *Campylobacter jejuni* helical cell shape

submitted
by Chang Sheng-Huei Lin in partial fulfillment of the requirements
for

the
degree of Doctor of Philosophy

in Microbiology and Immunology

Examining Committee:

Michael Murphy, Microbiology and Immunology, UBC
Supervisor

**Martin Tanner, Chemistry, UBC
Supervisory Committee Member**

Harry Brumer, Chemistry, UBC
University Examiner

Katherine Ryan, Chemistry, UBC
University Examiner

Additional Supervisory Committee Members:

Rachael Fernandez, Microbiology and Immunology, UBC
Supervisory Committee Member

Natalie Strynadka, Biochemistry and Molecular Biology, UBC
Supervisory Committee Member

Abstract

The helical morphology of enteropathogenic *Campylobacter jejuni* is determined by the structure of the peptidoglycan (PG) layer. This structure is dictated by cleavages by the LD-carboxypeptidase Pgp2 and the *O*-acetyl esterase Ape1 within the periplasm. In this thesis, I used X-ray crystallography, biochemical and genetic methods to investigate the interaction interfaces between these two enzymes and PG to select sites for remodeling to generate a helical cell shape.

Pgp2 uses two PG binding sites for enzyme activity. The Pgp2 structure consists of LD-carboxypeptidase (LD-CPase) and NTF2 domains, each contains a pocket formed by conserved residues. The LD-CPase pocket also contains the catalytic triad. The nucleophile Cys174 is confirmed to be essential for Pgp2 activity and helical cell shape. The NTF2 pocket, ~40 Å away from the triad, is lined with charged and hydrophobic residues important for full Pgp2 activity and helical shape. Site-directed mutagenesis demonstrates that residues in both binding sites are required for generating helical cell shape. NMR spectroscopy and PG pull-down assays unequivocally demonstrate that both pockets are PG binding sites. Since Pgp2 is likely to form a dimer in *C. jejuni*, I expect up to four PG binding sites in the dimer. I propose Pgp2 recognizes the tertiary structure of PG involving both the LD-CPase domain and the accessory NTF2 domain to induce a helical cell shape.

The Ape1 crystal structure is composed of a SGNH hydrolase domain, a CBM35 domain, and bound acetate located next to the predicted oxyanion hole. Deacetylase activity by Ape1 is assisted by residues derived from loops on the adjacent CBM35 domain. Residues Gln105, Asn121 and Arg123 of the CBM35 domain are hydrogen bonded to the loop forming the oxyanion hole. A model of the an Ape1-hexasaccharide complex suggests an orientation of PG in the active site that diverges from other members of the SGNH superfamily. I propose

Ape1 activity is dependent on the length of the PG glycan strand to modulate cell wall homeostasis.

Collectively, my thesis contributes to the knowledge about selective PG binding by PG hydrolases as one mechanism to control cell wall remodeling for generating helical shape.

Lay Summary

Every year, over 96 million people worldwide contract campylobacteriosis, a bacterial food-borne gastroenteritis primarily caused by *Campylobacter jejuni*. The helical cell shape of *C. jejuni* aids in successful host colonization. Peptidoglycan (PG) trimmed by the enzymes Pgp2 and Ape1 are responsible for generating the cell's helical shape. This thesis aims to define the binding interfaces between these two enzymes and PG to selectively cleave PG and induce helical shape formation. Pgp2 has two PG binding pockets that cooperatively guide Pgp2 activity. The Ape1 catalytic cleft is formed by loops from both the catalytic domain and a previously uncharacterized accessory domain, forming a putative substrate binding groove for accommodating multiple PG saccharides. The models of these enzyme-PG complexes add to our understanding of the mechanism of PG digestion for helical shape generation and provides guidance for the design of inhibitors of Pgp2 and Ape1.

Preface

Part of the work presented in this thesis is drawn from a published paper and a draft manuscript. These studies would not have been possible without collaborative inputs. Below is a description of the contributions made by fellow scientists and collaborators.

A version of Chapter 3 has been published as:

Lin, C. S., Chan, A. C. K., Vermeulen, J., Brockerman, J., Soni, A. S., Tanner, M. E., Gaynor, E. C., McIntosh, L. P., Simorre, J. P., and Murphy, M. E. P. (2021) Peptidoglycan binding by a pocket on the accessory NTF2-domain of Pgp2 directs helical cell shape of *Campylobacter jejuni*. *J. Biol. Chem.*, 100528.

Dr. Anson Chan, Dr. Michael Murphy and I designed the study and wrote the manuscript. Jenny Vermeulen made the *C. jejuni* complementation strains. Dr. Jacob Brockerman and Dr. Jean-Pierre Simorre collected the NMR spectra and assisted with resonance assignments. Arvind Soni collected and analyzed muropeptide mass spectra. I performed all other experiments, processed and analyzed the data. Dr. Martin Tanner, Dr. Erin Gaynor, Dr. Lawrence McIntosh and Dr. Jean-Pierre Simorre discussed the results and commented on the manuscript.

Chapter 4 is drawn from a draft manuscript:

Lin, C. S., Yen, I., Chan, A. C. K., and Murphy, M. E. P. Mechanism of the CBM35 domain in assisting catalysis of Ape1, a *Campylobacter jejuni* O-acetyl esterase.

I collected, processed, and determined the Ape1 crystal structures, performed the *O*-acetyl esterase activity assay of Ape1 variants, and conducted HADDOCK docking. Ian Yen designed an Ape1 expression construct, purified recombinant Ape1, and grew Ape1 crystals. Dr. Anson Chan assisted with twinned crystal data process and performed the synergistic *O*-acetyl esterase activity assay of Ape1 with Slt (soluble lytic transglycosylase). Dr. Michael

Murphy conceived of the project and provided mentoring throughout the project. I wrote the first draft of the manuscript and all other authors edited the manuscript.

Table of Contents

Abstract	iii
Lay Summary	v
Preface	vi
Table of Contents	viii
List of Tables	xi
List of Figures	xii
List of Symbols and Abbreviations	xiv
Acknowledgements	xvii
Dedication	xix
CHAPTER 1: Introduction	1
1.1 <i>Campylobacter jejuni</i>	1
1.1.1 Campylobacteriosis	1
1.1.2 <i>Campylobacter jejuni</i> classification and characteristics	3
1.1.3 <i>Campylobacter jejuni</i> adaptation to an enteric life style	4
1.1.4 <i>Campylobacter jejuni</i> helical shape in pathogenesis	5
1.2 Peptidoglycan	10
1.2.1 Peptidoglycan structure	10
1.2.2 Peptidoglycan biosynthesis	12
1.2.3 Peptidoglycan maturation	15
1.3 Curved and helical shape maintenance mechanisms	17
1.3.1 MreB directs rod shape formation in bacteria	17
1.3.2 <i>Caulobacter crescentus</i> CreS	19
1.3.3 <i>Vibrio cholerae</i> CrvA	21
1.3.4 Multifactorial shape system in <i>Helicobacter pylori</i>	22
1.4 <i>C. jejuni</i> helical shape generation	26
1.4.1 The <i>C. jejuni</i> helical cell shape determining proteins	26
1.4.2 The LD-carboxypeptidase Pgp2	30

1.4.3 The <i>O</i> -acetyl-esterase Ape1	31
1.5 Objectives of this thesis	32
CHAPTER 2: Materials and methods.....	34
2.1 Bacterial strains and growth conditions	34
2.1.1 <i>E. coli</i>	34
2.1.2 <i>C. jejuni</i>	34
2.2 Strain construction	36
2.2.1 Complementation of $\Delta pgp2$	36
2.3 Protein expression vectors construction.....	39
2.3.1 Pgp2 and Pgp2 site-directed mutagenesis.....	39
2.3.2 Ape1 and Ape1 site-directed mutagenesis	39
2.4 Recombinant protein expression and purification	40
2.4.1 Pgp2	40
2.4.2 Pgp2 labeled with ^{15}N , ^{13}C , ^2H	41
2.4.3 Csd6	42
2.4.4 Ape1	43
2.5 Crystallization and Structure determination	44
2.5.1 Pgp2 and K307A variant.....	44
2.5.2 Ape1	45
2.6 Microscopy and Celltool shape analysis.....	47
2.7 Immunoblotting.....	47
2.8 Peptidoglycan isolation.....	48
2.9 Muropeptide preparation and HPLC analysis.....	48
2.10 NMR.....	49
2.10.1 NMR spectra assignment	49
2.10.2 NMR titration experiment.....	49
2.11 Peptidoglycan pull-down	50
2.12 <i>O</i> -acetylesterease activity on 4-Nitrophenyl acetate	51
2.13 HADDOCK docking.....	51
2.13.1 Pgp2-PG	51
2.13.2 Ape1-PG	52

CHAPTER 3: PG recognition of Pgp2 determines <i>C. jejuni</i> helical shape	54
3.1 Introduction.....	54
3.2 Results.....	54
3.2.1 Two clusters of conserved residues are identified in the Pgp2 structure	54
3.2.2 The LD-CPase and NTF2 domains are required for helical shape	58
3.2.3 The NTF2 domain is required for Pgp2 catalytic activity in <i>C. jejuni</i>	60
3.2.4 The NTF2 domain binds PG	61
3.2.5 Strands β 9- β 10 form a flexible lip of the NTF2 domain binding pocket	62
3.2.6 Identifying PG-binding interfaces of Pgp2 by NMR-monitored titrations.....	63
3.2.7 NMR data-driven docking to identify binding modes between Pgp2 and PG.....	72
3.3 Discussion	76
CHAPTER 4: Role of the CBM35 domain in the <i>O</i> -acetyl esterase Ape1	83
4.1 Introduction.....	83
4.2 Results.....	84
4.2.1 Structure determination of <i>C. jejuni</i> Ape1	84
4.2.2 The overall structure of acetate-bound CjApe1	87
4.2.3 Two CBM35 loops promote Ape1 <i>O</i> -acetyl esterase activity	91
4.2.4 Ape1-PG binding mode by mechanism-guided HADDOCK docking.....	95
4.3 Discussion	103
CHAPTER 5: Concluding remarks.....	107
5.1 Role of Pgp2 in helical shape generation.....	107
5.1.1 Overview.....	107
5.1.2 Future directions	107
5.2 Mechanism of Ape1 in cell wall turnover.....	111
5.2.1 Overview.....	111
5.2.2 Future directions	112
References.....	114

List of Tables

Table 1-1. <i>C. jejuni</i> helical shape determining genes	6
Table 2-1. Bacterial strains used in this study	35
Table 2-2. List of primers used in this study	37
Table 2-3. List of plasmids used in this study	38
Table 3-1. Data collection and refinement statistics for Pgp2 and Pgp2 ^{K307A}	55
Table 3-2. HADDOCK calculation statistics of Pgp2-murotetrapeptide complexes.....	74
Table 4-1. Data collection and model refinement statistics of <i>C. jejuni</i> Ape1	86
Table 4-2. H-bond network between the CBM35 loop and the oxyanion hole	90
Table 4-3. <i>O</i> -acetyl esterase activity of CBM35 loop variants on <i>p</i> NPAc	94
Table 4-4. HADDOCK calculation statistics of CjApe1-PG complex.....	97

List of Figures

Figure 1-1. Schematic structure of cell wall in bacteria	10
Figure 1-2. Core structure of PG in Gram-negative bacteria.....	11
Figure 1-3. PG biosynthesis pathway	14
Figure 1-4. Sites of peptidoglycan structure remodeling.....	15
Figure 1-5. Cellular positions of divisome and elongasome complexes	18
Figure 1-6. Regions of a cell with measured Gaussian curvatures	23
Figure 1-7. Comparison of cell shape determining proteins in curved and helical bacteria... <i>C. jejuni</i>	28
Figure 1-8. Schematic of cell shape maintenance proteins used by <i>C. jejuni</i>	29
Figure 3-1. The conserved residues of Pgp2 are focused in two clusters: the active site of the LD-CPase domain and the pocket of NTF2 domain.....	57
Figure 3-2. Helical shape restoration of $\Delta pgp2$ by complementation with wild-type <i>pgp2</i> and point mutants of the catalytic triad and within the NTF2 pocket	59
Figure 3-3. HPLC muropeptide profile of <i>C. jejuni</i> wild-type, $\Delta pgp2$ and $\Delta pgp2$ complemented with point mutations of the catalytic triad and within the NTF2 pocket.....	60
Figure 3-4. Binding of Pgp2 mutants to $\Delta pgp2$ PG	61
Figure 3-5. Superimpositions of the Pgp2, Pgp2 ^{K307A} and Csd6 structures.....	62
Figure 3-6. HSQC spectra of Pgp2 assignment of backbone amide ¹⁵ N and ¹ H cross resonances	64
Figure 3-7. Overlaid HSQC spectra of ² H- ¹³ C- ¹⁵ N labeled and ² H- ¹⁵ N labeled Pgp2	65
Figure 3-8. Overlaid ¹⁵ N-BEST-TROSY spectra of ¹⁵ N-labeled Pgp2 titrated with muramidase-digested PG from <i>C. jejuni</i> $\Delta pgp2$	66
Figure 3-9. Relative intensity analysis of ¹⁵ N-labeled Pgp2 interacting with a panel of PG derived ligands	67
Figure 3-10. Chemical shift perturbation (CSP) analysis of ¹⁵ N-labeled Pgp2 interacting with a panel of PG-derived ligands.....	70
Figure 3-11. Interaction surfaces of Pgp2 with PG ligands identified from NMR-monitored titrations	71
Figure 3-12. HADDOCK models of the Pgp2-murotetrapeptide complexes driven by NMR spectral perturbations	75
Figure 3-13. The Pgp2-PG binding model.....	76

Figure 3-14. Superimpositions of active sites of Pgp2 and Csd6 structures.....	78
Figure 3-15. $\Delta pgp2$ PG digestion by Csd6	78
Figure 4-1. The crystal structure of <i>C. jejuni</i> Ape1	85
Figure 4-2. Active site arrangement and electrostatic potential properties of Ape1 ⁴¹⁻³⁹²	89
Figure 4-3. Structural comparison of CBM35 structural homologs	90
Figure 4-4. Assays of <i>O</i> -acetyl esterase activity and PG binding of CBM35 loop variants... <td>93</td>	93
Figure 4-5. $\Delta ape1$ PG pull-down assay	94
Figure 4-6. Seven clusters of Ape1- <i>O</i> -acetyl hexasaccharide docking models from HADDOCK.....	98
Figure 4-7. HADDOCK model of the CjApe1- <i>O</i> -acetyl hexasaccharide complex.....	98
Figure 4-8. Comparison of proposed substrate binding orientations within the SGNH hydrolase superfamily	100
Figure 4-9. Structure of the SNGHL2 loop and sequence alignment	101
Figure 4-10. Ape1 phylogenetic tree showing the evolution of the intramolecular disulfide bond of loop SGNHL2.....	102
Figure 4-11. <i>O</i> -acetyl esterase activity of CjApe1 and Slt	105

List of Symbols and Abbreviations

Å: Angstrom ($1 \text{ \AA} = 0.1 \text{ nm}$)

AIR: Ambiguous Interaction Restraint

Ala: alanine

B-factor: Crystallographic thermal factor

CBM: carbohydrate binding module

CFU: colony forming units

C₅₅P: undecaprenyl phosphate

cP: centipoise

D₂O: Deuterium oxide

DAP: Diaminopimelic acid

DTT: Dithiothreitol

D-Glu: D-glutaminic acid

EDTA: Ethylenediamine tetra-acetic acid

FCC: Fraction of common contacts

GBS: Guillain-Barré Syndrome

GlcNAc: *N*-acetyl glucosamine

GTase: transglycosylase

His₆: Poly-histidine affinity purification tag

HPLC: High Performance Liquid Chromatography

IF: intermediate filament

IL-8: Interleukin-8

IPTG: Isopropyl β -D-thiogalactopyranoside

LB: Luria Bertani

Lipid I: undecaprenyl-pyrophosphoryl-MurNAc-pentapeptide

Lipid II: undecaprenyl-pyrophosphoryl-MurNAc-(pentapeptide)-GlcNAc

Lpp: Braun's lipoprotein

LPS: lipopolysaccharide

LT: Lytic transglycosylase

MALDI-TOF: Matrix-assisted laser desorption/ionization-time of flight mass spectrometry

MDP: Muramyl dipeptide

m-Dap: *meso*-diaminopimelic acid

MH: Mueller-Hinton

MH-TV: Mueller-Hinton containing trimethoprim and vancomycin

MurNAc: *N*-acetyl muramic acid

MW: Molecular weight

NMR: Nuclear magnetic resonance

OAP: O-acetylation of peptidoglycan

OD₆₀₀: Optical density at 600 nm wavelength

PBS: Phosphate buffered saline

PBP: Penicillin binding protein

PCR: Polymerase chain reaction

PDB: Protein data bank

PEG: Polyethylene glycol

PG: Peptidoglycan

PMSF: Phenylmethylsulfonyl fluoride

*p*NPAc: *p*-nitrophenol acetate

RMSD: Root mean squared deviation

SAD: Single-wavelength anomalous dispersion

SDS-PAGE: Sodium dodecyl sulfate-polyacrylamide gel electrophoresis

SEC-MALS: Multi-angle light scattering coupled with size exclusion chromatography

SEDS: Shape, Elongation, Division, and Sporulation

SeMet: Seleno-methionine

SGNH domain: SGNH consensus catalytic motif (serine, glycine, asparagine, histidine)

SIGRR: single-IgG-IL-1-related receptor

Slt: soluble lytic transglycosylase

SSRL: Stanford Synchrotron Radiation Lightsource

TBS-T: Tris-buffered saline, 0.1% Tween 20

TIRFM: total internal reflection fluorescence microscopy

TM: Transmembrane

TPase: Transpeptidase

Tris: Tris(hydroxymethyl)aminomethane

TROSY: Transverse relaxation-optimized spectroscopy

UDP: uridine diphosphate

Acknowledgements

This research is funded by Canadian Institute of Health Research Grants to Dr. Michael Murphy. Funding of this work is provided by Directions of subsidiary funding of Aboriginal Commoner scholar, Taiwanese Council of Indigenous Peoples.

I would like to express my thanks to Dr. Michael Murphy for his mentoring, supervisions, and financial support over the years. I am also grateful that Michael helped me start *in silico* modeling works. I would like to thank my committee, Dr. Rachael Fernandez, Dr. Natalie Strynadka and Dr. Martin Tanner for their guidance and feedback on my thesis. Thanks also to Dr. Erin Gaynor for providing lab resources to perform *C. jejuni* studies. Thanks to Jenny Wallace for making *C. jejuni* complementation strains and assisting microscopy studies. Thanks to Dr. Jean-Pierre Simorre for designing the NMR project of Pgp2 and peptidoglycan interaction. Thanks to Dr. Lawrence McIntosh and his lab members, Dr. Jacob Brockerman, Dr. Mark Okon, Dr. Cecilia Perez-Borrajero and Karlton Scheu for their help with NMR data collection and data analysis. I cannot learn NMR from scratch without your mentoring and support. Thanks to Dr. Martin Tanner and Arvind Soni for synthesizing Pgp2 substrate analogues and performing MALDI-TOF mass spectrometry studies. Thanks to Dr. Jason Rogalski for performing protein ESI-MS analysis. Thanks to Dr. Seemay Chou for providing the Tse1 and Tae2 expression construct. Thanks to Dr. Emilisa Frirdich for project discussions and critically reviewing the Pgp2 manuscript. Special thanks to Pauline, Darlene and Parvin for the administrative assistance in the M&I graduate program. Thanks to Eric and Patrick for the department computer technology support.

Surely, I would like to thank all of the past and present members of the Murphy lab. Particular thanks to Dr. Anson Chan for being a wonderful mentor. I am always encouraged when talking to Anson about science. Thanks to the best lab manager Angele for sharing her

knowledge and experiences. Thanks to Emily and Maxim for being lovely friends. I always have fun when you are around. Thanks to Ian for the excellent work and input in the Apel project. Thanks to Jason, Slade, Marek, Meghan, and Mariko for helping me start in the lab. Thanks to Brigid, Jen, Daniela, Tom and Brianne for the help in the lab and for giving feedback on my projects.

Lastly, I would like to thank my family, my Master program supervisor Dr. Sherry Wang, and my friends Jane, Anna, Lok and Brian. I could not get the degree without your love and support.

*To my parents:
Chin-Lai and Guei-Yin*

CHAPTER 1: Introduction

1.1 *Campylobacter jejuni*

1.1.1 Campylobacteriosis

Campylobacteriosis is one of the most common foodborne gastroenteritis in the world. It develops after ingestion of food contaminated with *Campylobacter* sp.. The World Health Organization (WHO) reported 600 million gastroenteritis cases caused by the 31 foodborne pathogens in 2010, of which campylobacteriosis accounts for 96 million (1). Campylobacteriosis in the United States, is estimated to affect a million people a year (2). In the European Union, it was the most reported zoonotic disease since 2005 and the confirmed number of illnesses was 246,571 in 2018 (3). In Canada, it is in the top three acquired foodborne diseases with an annual number of cases estimated to be 145,000 (4). The primary transmission route of human campylobacteriosis is through food (5). Specific food sources are: undercooked poultry, unpasteurized milk and contaminated water. Another concerning transmission cause is through animal contact. An outbreak involving customers and staff occurred in a pet store in the United States because of contact with dogs carrying *C. jejuni* (6).

Campylobacteriosis patients develop acute gastroenteritis with symptoms including watery diarrhea, bloody stool, abdominal pain, vomiting, fever and dehydration. Most cases recover within 5 to 7 days post infection, but in some cases, gastrointestinal inflammation leads to dysregulated immune responses in the gastrointestinal tract (i.e., inflammatory bowel disease) and joints (i.e., reactive arthritis). There is a positive correlation between these immune diseases and gastroenteritis caused by *Campylobacter* sp. (7). Guillain-Barré Syndrome (GBS) is another serious sequela of campylobacteriosis, characterized by weakness

of peripheral muscles caused by autoimmune attack on peripheral nerves. Paralysis of respiratory muscles leads to a 3%–13% mortality rate (8). It is estimated that GBS affects one person in 100,000 each year in the world (9). Efforts to understand the link between campylobacteriosis and GBS suggests that molecular mimicry between the lipooligosaccharide antigen of *C. jejuni* and the carbohydrate antigen of nerve gangliosides as a possible cause of GBS (10).

Gastroenteritis caused by *Campylobacter* sp. and its sequelae have added economic burden to global society. The annual cost of campylobacteriosis in the United States was estimated at US \$1.5–8.0 billion in 1995 (11). High healthcare expenses are also reported in Europe, Canada, Australia and New Zealand (12). Furthermore, emergence of antibiotic resistant strains of *Campylobacter* sp. has worsened the global burden. Abuse of antibiotics in clinical treatment and in farming correlate with the occurrence of clinical resistant strains (13). The European Union and the United States have issued animal feed directives that control clinical antibiotics (e.g., macrolides) used as growth promoters in food animals (14,15).

Some countries have mitigated the prevalence of campylobacteriosis by promoting food safety. In New Zealand, a 54% decline in campylobacteriosis was observed from 2007 to 2008 (16). The reduction is attributed to processing meat under standard hygiene protocols and freezing of fresh poultry meat. Biocontrol measures to decrease *Campylobacter* sp. load on chickens include: use of feed additives, probiotics, bacteriophages and bacteriocins; and vaccination of chickens (17). These methods reduce the viability of *C. jejuni* *in vitro*, but their efficacy in animal models is not fully studied. Proposed approaches are also challenged by the high titer used, compound instability at low pH, and developed resistance by *C. jejuni*. Prolonged colonization of chickens by *Campylobacter* sp. causes weight loss in the animals, a

concern of the food production industry (18). Taken together, despite efforts being made, new methods to reduce bacterial load in chickens remain of primary importance to attenuate the global health and economic burden of campylobacteriosis.

1.1.2 *Campylobacter jejuni* classification and characteristics

The *Campylobacter* genus belongs to the family Campylobacteraceae, the order Campylobacterales, the class Epsilonproteobacteria and the phylum Proteobacteria. The genus consists of 47 species and 16 subspecies (as of January 2021; <https://www.bacterio.net>). *Campylobacter* sp. are zoonotic bacteria usually found in farm animals (e.g., chickens, cows, pigs and dogs) as asymptomatic colonizers. However, in humans, ingestion of as little as 500–800 cells can cause diarrheal diseases (19,20). *C. jejuni* is the primary species responsible for gastroenteritis in humans, and *C. coli* accounts for 1–25% of the cases (21).

C. jejuni is a Gram-negative enteric bacterium with cell size range approximately between 0.2–0.8 µm wide and 0.5–5 µm in length. The cell has polar flagella at both ends and displays helical shape in exponential growth phase (22). *C. jejuni* is thermo-tolerant, it grows between 32 and 47°C with optimal growth temperature between 42 and 45°C (23). This characteristic contributes to its colonization of chickens (body temperature around 42°C), as well as mammals (body temperature around 37 °C). *C. jejuni* grows in pH values ranging from 5.5–8.0, and its optimal growth pH is at pH 6.5–7.5 (23). Unlike other common enteric pathogens such as *Escherichia coli* and *Salmonella Typhimurium* that are facultative anaerobes, *C. jejuni* is a microaerophile and is cultured under 5%–10% O₂ and 1–10% CO₂ (24) or growing in the enrichment medium supplemented with antimicrobial agents (e.g., vancomycin, polymyxin B, trimethoprim and amphotericin B) that suppress other bacteria in the culture at aerobic conditions (25).

1.1.3 *Campylobacter jejuni* adaptation to an enteric life style

The human intestinal track is covered by a layer of mucus. This mucus layer is mostly composed of mucin glycoproteins and serves as a physical barrier and immunological scaffold to protect deep tissue from bacteria invasion. The mucus layer can be subdivided into an outer loose layer and the inner firm layer (26). The outer loose layer hosts gut microbiota and antimicrobial components that clear pathogens through competition and innate immune defense mechanisms. The inner firm layer is normally devoid of bacteria, confirming a role of the mucus layer in separating bacteria from the gut tissue.

C. jejuni is found in different sites of the gastrointestinal tract in different hosts such as: cecum for chickens (27,28), cecum and large intestines for mice (29,30), and small intestines for cattle (31). *C. jejuni* human pathogens are usually isolated from feces. *C. jejuni* prefers to colonize close to the epithelium of the gut instead of the lumen (27,30). This localization may reflect the microaerophilic nature of *C. jejuni* as oxygen level drops in a radial gradient from the tissue to the lumen in the gut (32). *C. jejuni* has excellent motility to cross the mucus firm layer and reach the epithelium. Different to other flagellated enteric bacteria (*E. coli*, *Vibrio cholerae*, and *Salmonella enteritidis*), *C. jejuni* is motile when grown in viscous media (33). Interestingly, increased swimming velocity is observed in the media with increased viscosity (34,35).

C. jejuni is adapted to the nutritional environment of the mucus layer where amino acids and secondary metabolites are rich from the diet and the cell lysis of gut microbiota. The major carbon sources used by *C. jejuni* are amino acids and citric acid cycle intermediates. Incubation of *C. jejuni* in media supplemented with chicken/human mucus exhibited higher a reproduction rate than incubation in media alone (36,37). *C. jejuni* is considered as a low

carbohydrate consumer, a key enzyme 6-phosphofructokinase in the glycolytic pathway is missing in the genome, and *C. jejuni* is unable to use glucose as a carbon source (38). Despite *C. jejuni* not being able to metabolize carbohydrates such as glucose or galactose, a few *C. jejuni* strains carry a genomic island encoding transporters to uptake L-fucose (39), a common sugar derived from human mucin (40). The ability to uptake L-fucose by *C. jejuni* increased growth and competitive colonization in neonatal piglets as compared to the deficient strain (39). *C. jejuni* exhibits chemotactic responses to L-aspartate, L-glutamate, L-serine, pyruvate, fumarate and L-fucose (41) and readily uses aspartate, glutamate, asparagine, glutamine, serine, and proline (42,43). Genes involved in amino acid transport and the catabolic pathways are abundant in *C. jejuni*. Overall, the gut mucus layer serves as a suitable niche that meets the metabolic requirements of *C. jejuni*.

1.1.4 *Campylobacter jejuni* helical shape in pathogenesis

C. jejuni presents as a rod- and coccoid-shape under stressed conditions and helical-shape in log-phase growth culture. The cell's helical shape is proposed to provide selective advantages for facilitating bacterial motility. In *H. pylori*, also a flagellated helical-shaped bacterium, swimming speed predominantly depends on the propulsion force driven by flagellar rotation. The swimming speed increases ~19% when the number of flagella increases from 3 to 4 (44). Apart from the flagella propulsion, the helical shape may influence both thrust and drag to increase bacterial velocity (45). In a modeling experiment using *H. pylori* cell morphology parameters (cell axis length, helical pitch and helical radius), helical body rotation rate is estimated to contribute to propulsive thrust by up to 15%. When the cell axis length increased, the swimming speed of *H. pylori* decreased because of increased drag. When cell length is fixed, changing the length of helical pitch in cells resulted in a change in speed.

C. jejuni use several genetic elements to maintain helical cell morphology. Known shape-determining genes include *pgp1*, *pgp2*, *pgp3*, *CJJ81176_1228*, *CJJ81176_1105* and *ape1* (**Table 1-1**). Bacterial strains with deletion of the target gene are denoted as: $\Delta pgp1$, $\Delta pgp2$, $\Delta pgp3$, $\Delta 1228$, $\Delta 1105$, $\Delta ape1$. No discernable defects in cell growth, stress survival, membrane protein composition, nor swimming velocity in non-viscous liquid media were found in the shape-determining gene deletion strains. Conversely, important pathogenic attributes such as viscous motility, colonization, cell invasion, and host-immune responses are altered, implying the importance of the helical shape in *C. jejuni* pathogenesis.

Table 1-1. *C. jejuni* helical shape determining genes

Protein	Gene	Function	Shape of deletion strain	Reference
Pgp1	<i>CJJ81176_1344</i>	DL-carboxypeptidase	Straight	(46-48)
Pgp2	<i>CJJ81176_0915</i>	LD-carboxypeptidase	Straight	(47,49)
Pgp3	<i>A8118_01115</i>	DD-endopeptidase	Curved-Rod	(50)
		DD-carboxypeptidase		
1105	<i>CJJ81176_1105</i>	DD-endopeptidase ^a	Curved-Rod	(48,51,52)
1228	<i>CJJ81176_1228</i>	DD-endopeptidase ^b	Curved-Rod	(53)
Apel	<i>CJJ81176_0638</i>	O-acetyl esterase	Comma	(54)

^a1105 sequence is predicted with a M23 peptidase domain (51). Complementation of *CJJ81176_1105* gene restores the helical shape of $\Delta csd1$, a straight *H. pylori* strain with *csd1* gene (DD-endopeptidase) deletion (52).

^b1228 sequence is predicted with a M23 peptidase domain. 1228 is a homolog of *H. pylori* DD-endopeptidase Csd3 (sequence identity 46%).

The helical shape of *C. jejuni* is proposed to help passage through the mucus layer to reach the intestinal epithelium. Cell motility of shape mutants on gel-like soft agar plates was examined. Strains $\Delta pgp2$, $\Delta ape1$, $\Delta pgp1$, $\Delta 1128$, and $\Delta 1105$ displayed a reduction in motility as compared to wild-type motility by 30%, 30%, 20%, 15%, and 15%, respectively (46,49,51,53,54). The motility defects in soft agar were not due to deficiency in flagellar rotation. Video-recording of these mutant strains in liquid media indicated that $\Delta pgp2$, $\Delta pgp1$,

and $\Delta l128$ exhibited unaltered velocity compared to the wild-type strain (53). Therefore, the helical shape contributes to bacterial motility in viscous media.

Insight into the mechanism of how helical shape contributes to motility in viscous media was shown by investigation of flagellar motion. *C. jejuni* responds to increased viscosity by changing swimming modes (55). *C. jejuni* showed smooth and tumbling swimming in low viscosity media (< 1.5 cP). The bacterium demonstrates darting with long straight paths at medium viscosity (1.5–40 cP), and back and forth movement with short straight paths at high viscosity (40 cP). Imaging of fluorescent labeled flagella revealed that *C. jejuni* demonstrated two characteristic flagellar motions during swimming in viscous media: “unwrapped mode” and “wrapped mode” (34). In the unwrapped mode”, both polar flagella are projected outward into the media, whereas in the “wrapped mode”, the leading flagella wraps along helical cell body and the lagging flagella extends into the media. In low viscous media, most *C. jejuni* cells present “unwrapped mode” flagellar motion. The population of “wrapped mode” cells increases as the viscosity of media increases, and the average velocity of cells also increases, suggesting that the “wrapped mode” is associated with *C. jejuni* motility at high viscosity (34). Helical shape likely aids the flagella to stay in “wrapped mode”. The polarity of the wrapped flagella alternates when changing swimming directions. Notably, rod-shaped strain $\Delta pgp1$ displayed a 75% reduction of wild-type efficiency in exchanging the wrapped flagella (34).

Helical shape of *C. jejuni* seems to be a key factor for host colonization. Cell shape mutants were used to examine cecal colonization in 1-day-old or 3-week-old chicks (CFU/g) 5–7 days post infections. Rod-shaped $\Delta pgp1$ and $\Delta pgp2$, and comma-shaped $\Delta ape1$ showed 2–4.4 log decrease of wild-type colonization (46,49,54), suggesting that helical shape contributes to chicken colonization by *C. jejuni*. On the other hand, the curved rod-shaped

$\Delta 1105$ showed unaltered chicken colonization (47). The different degrees of colonization by these shape mutants may indicate that, other than cell shape, these mutants caused disruptions to unknown physiological attributes required for colonization. It is also possible that host susceptibility may account for colonization efficiency in above experiments. Three-week-old chicks carry reduced maternal antibodies and display relatively susceptible to *C. jejuni* infections as compared to one-day-old chicks (56).

Helical shape helps *C. jejuni* penetrate the mucus layer to reach the crypts of the epithelium of the small intestine (29). The single-IgG-IL-1-related receptor (SIGRR) is a negative regulator of MyD88-dependent inflammatory signalling. Vancomycin pretreated SIGRR ($-/-$) mice are susceptible to *C. jejuni* infections and show acute gastrointestinal inflammation to mimic human infections (29). SIGRR ($-/-$) mice were used to study *C. jejuni* helical shape mutants' colonization and crypt localization. The levels of colonization of $\Delta pgp1$ and $\Delta pgp2$ were similar to wild-type in SIGRR ($-/-$) mice. However, microscopic examination of the cecal tissue revealed that $\Delta pgp1$ and $\Delta pgp2$ were present in the mucus layer close to the lumen but were absent in crypts, different from the wild-type strain that was present across the lumen and crypts (53). Crypt colonization can be restored by complementation of *pgp1* and *pgp2* genes in trans. This study highlights that helical shape helps *C. jejuni* crypt colonization.

Helical shape contributes to bacteria-host interaction during *C. jejuni* infections. *C. jejuni* can adhere to, invade and survive within epithelial cells. These attributes were measured *in vitro* using intestinal epithelial cell lines (INT407 or Caco-2 cells) in gentamicin protection assays. Rod-shaped $\Delta pgp1$ and $\Delta pgp2$ displayed unaltered cell binding and invasion (46,49). The ability of other helical shape mutant strains to invade cells was affected: $\Delta 1228$ exhibited small defects in adherence, invasion, and intracellular survival (53); $\Delta pgp3$ showed reduced

cell invasion compared to the wild-type strain, and complementation partially restored the deficiency (50); $\Delta 1105$ showed ~50% adhesion and invasion of the wild-type strain, and the deficiency can be restored by complementation (51). Highly curved $\Delta ape1$ strain showed significant reduction in cell adherence, invasion and intracellular survival (54).

Helical shape is associated with structural changes in peptidoglycan (PG). These changes lead to altered induction of host immune responses through cytoplasmic Nod1 and Nod2 receptor activation (57,58). The Nod1 and Nod2 receptors recognize diaminopimelic acid (DAP) and muramyl dipeptide (MDP) moieties of PG, respectively, and induce signaling pathways for inflammatory gene expressions (59). DAP containing tripeptides are increased in $\Delta pgp1$ (46), but are decreased in $\Delta pgp2$ (49) and coccoid *C. jejuni* (60). As predicted, Nod1 activation in HEK293T cells was increased by $\Delta pgp1$ PG, and decreased by $\Delta pgp2$ and coccoid *C. jejuni* PG. Nod2 activation of HEK293T cells by the mutant PG were unexpected. The MDP level in $\Delta pgp1$ and $\Delta pgp2$ PG are decreased, but no changes in Nod2 activation are found (46,49). Coccid cells had increased MDP but resulted in decreased Nod2 activation (60).

Another immune response influenced by *C. jejuni* cell shape is interleukin-8 (IL-8) secretion. Epithelial cells can secrete the neutrophil chemoattractant IL-8 in response to *C. jejuni* infection. The level of IL-8 secretion is positively correlated with *C. jejuni* cell adhesion and invasion ability (61) and cytolethal distending toxin activity (62). IL-8 secretion was measured from incubation of epithelial INT407 cells with *C. jejuni* helical-shape mutant strains. Cells infected by $\Delta 1228$, $\Delta ape1$, and coccid strains showed reduced IL-8 secretion as compared to wild-type strain infected cells, consistent with the low cell invasion by these strains (53,54,60). In contrast, enhanced IL-8 was observed in $\Delta pgp1$ infected epithelial cells despite $\Delta pgp1$ showed unaltered cell adhesion ability (46).

1.2 Peptidoglycan

1.2.1 Peptidoglycan structure

PG is a net-like polymer encircling the cell and provides resistance to cell rupture resulting from osmotic stress. In Gram-negative bacteria, the PG is a thin layer between the cytoplasmic membrane and the outer membrane (**Figure 1-1**). It is tethered to the outer membrane through covalently bound Braun's lipoprotein (Lpp) (63,64). The length of the PG-Lpp complex is proposed to define the size of the periplasmic space for proper flagellar assembly (65). In Gram-positive bacteria, the PG is a much thicker layer which surrounds the cytoplasmic membrane and is directly exposed to the external environment because of the absence of an outer membrane. Gram-positive PG is covalently bound to wall teichoic acids and lipoteichoic acids. These anionic glycopolymers are important for cell envelope biology, such as cation homeostasis, cell growth and division, and antibiotic resistance (66).

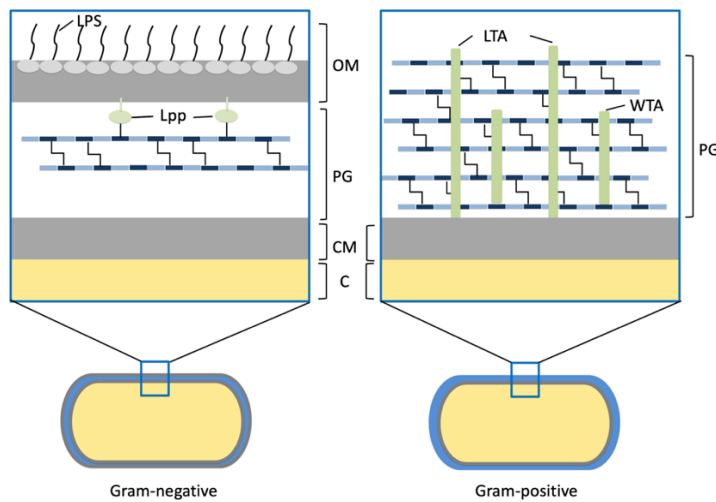


Figure 1-1. Schematic structure of cell wall in bacteria

Schematic presentation of cell surface compositions in Gram-negative and Gram-positive bacteria. C, cytoplasm; CM, cytoplasmic membrane; PG, peptidoglycan; OM, outer membrane; Lpp, Braun's lipoprotein; LPS, lipopolysaccharide; WTA, wall teichoic acid; LTA, lipoteichoic acid.

The core chemical structure of PG is well conserved across bacterial species. The glycan backbone of PG consists of repeated disaccharide units of β -(1-4)-*N*-acetyl glucosamine (GlcNAc) and *N*-acetyl muraminic acid (MurNAc). The C3 position of MurNAc is attached via a lactyl bond to a peptide stem, generally composed of L-Ala-D-Glu-*m*-Dap (or L-Lys)-D-Ala-D-Ala in nascent PG, and can be trimmed or cross-linked between adjacent glycan strands (**Figure 1-2**) (67). The 4-3 cross-linkage occurs at the D-Ala⁴ \rightarrow (D) *m*-Dap³ positions either through a direct peptide bond or via a pentaglycine peptide bridge (67). The 3-3 linkage is at the (L) *m*-Dap³ \rightarrow (D) *m*-Dap³ positions and is the major cross-link in pathogens like *Mycobacterium tuberculosis* and *Clostridium difficile* (68,69).

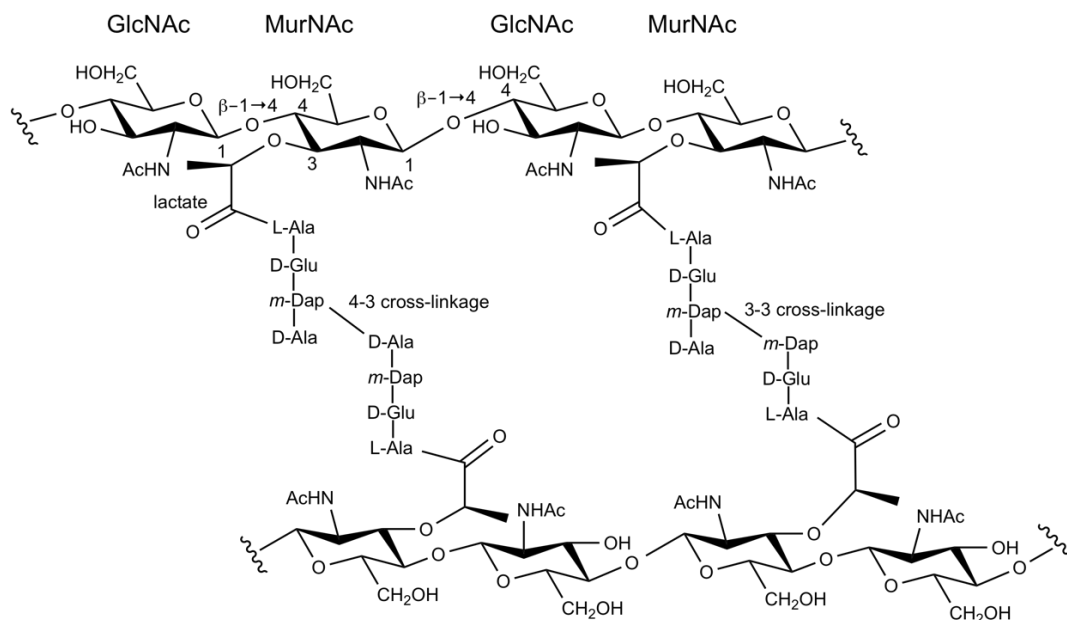


Figure 1-2. Core structure of PG in Gram-negative bacteria

PG consist of glycan chains cross-linked by the short peptides. The glycan chain consists of GlcNAc and MurNAc linked by β -(1-4)-glycosidic bond. A peptide is bonded through the a lactyl group to third carbon of MurNAc. Cross-links between neighboring peptides occur at the fourth D-Ala and (D) *m*-Dap (4-3 cross-linkage) or at the (L) *m*-Dap and (D) *m*-Dap (3-3 cross-linkage). The abbreviations indicate as follows: L-alanine (L-Ala), D-glutaminic acid (D-Glu), *meso*-diaminopimelic acid (*m*-Dap), and terminal D-alanine (D-Ala).

1.2.2 Peptidoglycan biosynthesis

The PG biosynthetic pathway consists of three main stages that occur across the cytoplasmic membrane (**Figure 1-3**). The synthesis of the cytosolic PG precursor uridine diphosphate (UDP)-MurNAc-pentapeptide starts in the cytoplasm. The initial substrate, UDP-GlcNAc, originates from D-fructose-6-phosphate by successive reactions catalyzed by the enzymes GlmS, GlmM and GlmU (70). UDP-GlcNAc is the substrate of the enzymes MurA and MurB to produce UDP-MurNAc. The peptidyl moiety is added onto UDP-MurNAc by ATP-dependent Mur ligases. Amino acids L-Ala, D-Glu, *m*-Dap or L-Lys, and dipeptide D-Ala-D-Ala are each added to UDP-MurNAc by the enzymes MurC, MurD, MurE, and MurF in a sequential order. Bacteria have unique enzymes to synthesize D amino acids (71). D-Glu is produced from L-Glu by glutamate racemase and from α -ketoglutarate by D-amino acid aminotransaminase. D-Ala is synthesized from L-Ala by D-Ala racemase. The dipeptide D-Ala-D-Ala is ligated by D-Ala-D-Ala ligase.

UDP-MurNAc-pentapeptide is later transferred onto a 55-carbon-long membrane acceptor undecaprenyl phosphate (C₅₅P) in the inner face of the cytoplasmic membrane by MraY, yielding a membrane associated undecaprenyl-pyrophosphoryl-MurNAc-pentapeptide (Lipid I) (72). A UDP-GlcNAc is added to Lipid I with UDP release by MurG, generating undecaprenyl-pyrophosphoryl-MurNAc-(pentapeptide)-GlcNAc (Lipid II). Lipid II is then flipped from the inner face to the outer face of the cytoplasmic membrane. The identity of flippase responsible for Lipid II translocation was controversial with candidates MurJ and FtsW (73). Recent studies have shown strong support for MurJ being the transporter. Inactivation of MurJ led to impaired Lipid II translocation in *E. coli* (74,75). Experiments using mass spectrometry suggested MurJ has a higher Lipid II binding affinity than FtsW since

at the same Lipid II concentration, MurJ but not FtsW, formed a protein-Lipid II complex (76). FtsW showed Lipid II flippase activity in a reconstructed liposome *in vitro*, and MurJ showed no activity in the same assay (77). However, Lipid II translocation was not inhibited in the absence of FtsW expression (74). The debate was cleared up when FtsW was revealed with a PG polymerase activity (78).

Lipid II is polymerized and crosslinked into the growing PG in the periplasm by the transglycosylase (GTase) and transpeptidase (TPase). The C4 position of the GlcNAc moiety of Lipid II is bonded to the C1 position of the MurNAc moiety of the growing glycan chain by the GTase (79-81). The by-product C₅₅-PP is converted to C₅₅-P and is recycled back to the inner face of the cytoplasm for the translocation of the next cytoplasmic PG precursor (82-84). For a long time, known GTases consisted of the bifunctional class A penicillin binding proteins (aPBP) containing both GTase and TPase activities and the monofunctional GTases (85). Recent studies suggest that the integral membrane SEDS (Shape, Elongation, Division, and Sporulation) family are a new class of GTases. The SEDS proteins RodA and FtsW were able to polymerize Lipid II substrate *in vitro* (78,86). Their mechanisms of action is not inhibited by the aPBP inhibitor moenomycin (78,86), and the FtsW activity required divalent cation and presence of the monofunctional class B PBP (bPBP) containing TPase activity (78).

The newly synthesized glycan chain is crosslinked to an adjacent glycan chain by transpeptidation reactions. The 4-3 cross-linkages are catalyzed by DD-TPases, including the bifunctional aPBP and monofunctional bPBP (85). Their TPase activities are inactivated by beta-lactam antibiotics because of the analogous structure of the beta-lactam ring and the CO-N bond in D-Ala-D-Ala substrate (87). The 3-3 cross-linkage are synthesized by LD-TPases.

The LD-TPases were suggested to provide some pathogens with beta-lactam antibiotic resistance as these enzymes were insensitive to penicillin drugs (88-90).

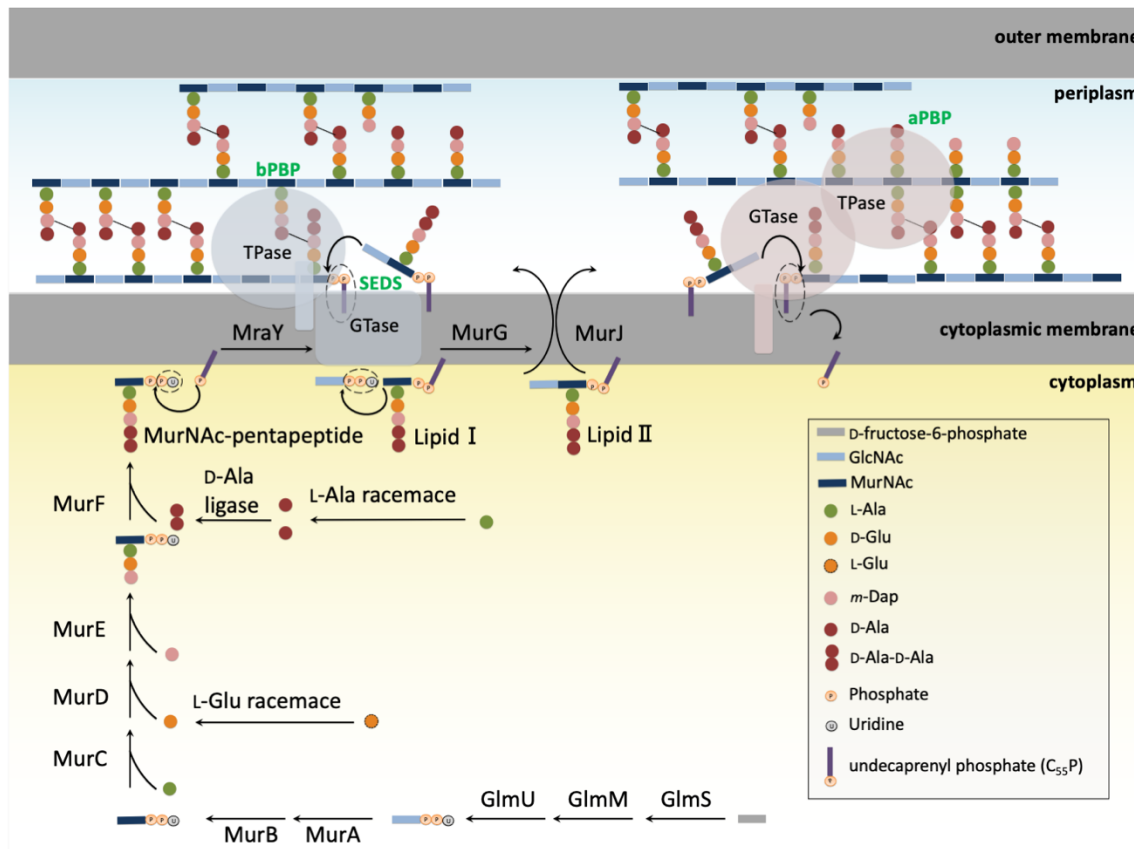


Figure 1-3. PG biosynthesis pathway

Schematic representation of reactions and enzymes involved in the synthesis of PG across the cytoplasmic membrane. The cytosolic PG precursor UDP-MurNAc-pentapeptide is synthesized by the enzymes GlmS, GlmM, and GlmU, followed by MurA-F. UDP-MurNAc-pentapeptide is transferred onto a membrane acceptor $C_{55}P$ to form a membrane associated PG precursor Lipid II by the enzymes MraY and MurG. Lipid II is flipped from the inner face to the outer face of the cytoplasmic membrane by MurJ, followed by polymerization to the existing PG by GTase and TPase. PG polymerization is achieved by bifunctional aPBP with both GTase and TPase activities or by the SEDS GTase family and bPBP TPase.

1.2.3 Peptidoglycan maturation

The newly synthesized PG is further remodeled by additional enzymes. Some peptide bonds and glycosidic bonds are hydrolyzed for different physiological purposes. For example, hydrolysis of the 4-3 cross-linkages of existing PG allows insertions of new PG strands (91), removal of peptide stem in PG contributes to cell separation (92), and cleavage of PG glycan strands generates space to accommodate large molecular machines such as flagella, pili and secretion systems that span across both membranes (93,94).

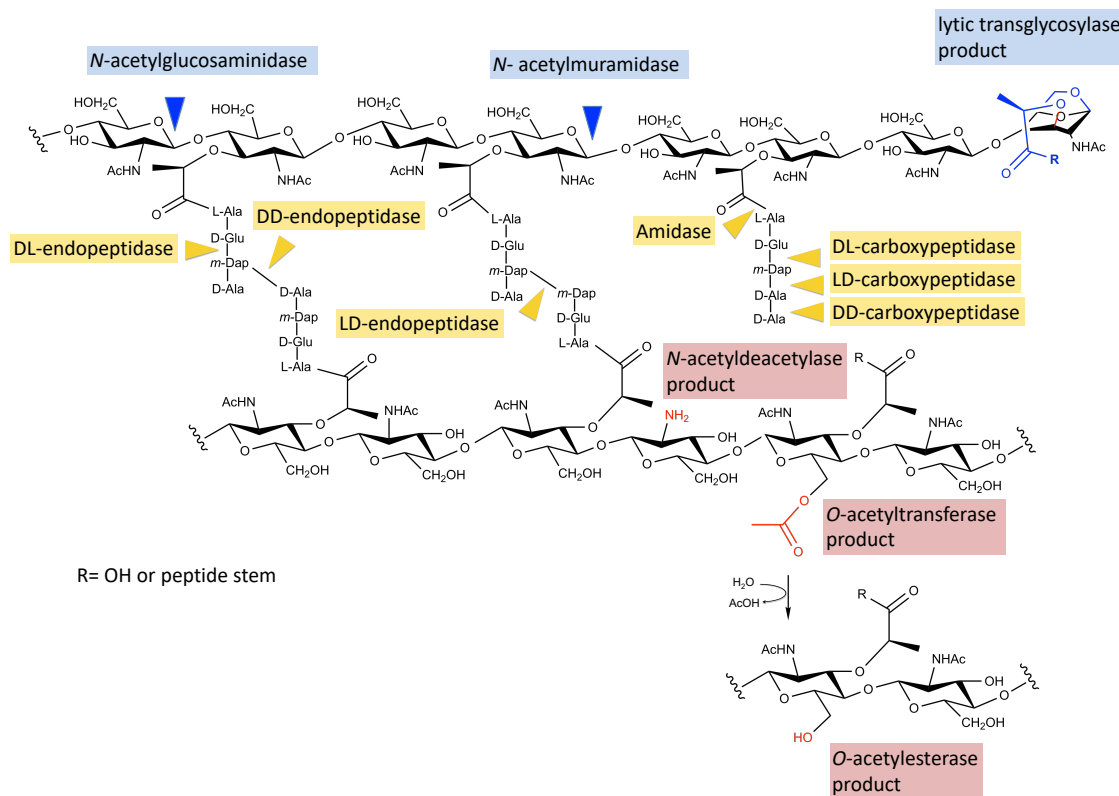


Figure 1-4. Sites of peptidoglycan structure remodeling

PG remodeling processes includes the cleavage of PG covalent bonds and modification of acetylation levels of the glycan strand. The solid triangle symbol represents sites of hydrolysis. Three glycosidases *N*-acetylglicosaminidase, *N*-acetylmuramidase and LT cleave glycosidic bonds within the glycan chain. Peptidases, *N*-acetylmuramoyl-L-alanine amidases, carboxypeptidases and endopeptidases cleave the covalent bonds in the peptide stems. D or L indicate the chiral center of carbons making the peptide bond. *O*-acetyltransferase adds the acetyl group to MurNAc. *N*-acetyldeacetylase and *O*-acetylesterase hydrolyzes the acetyl group from the glycan strand.

The PG hydrolases include both glycosidases or peptidases (**Figure 1-4**) as reviewed in (95-97). Three distinct glycosidases are identified that cleave the β -(1-4)-glycosidic bonds in PG. *N*-acetylglucosaminidase cleaves the bond between GlcNAc and MurNAc, and produces GlcNAc and MurNAc reducing ends. *N*-acetylmuramidase and lytic transglycosylase (LT) both cleave bonds between MurNAc and GlcNAc but using different mechanisms. *N*-acetylmuramidase adds water to hydrolyze the bond and releases MurNAc and GlcNAc containing reducing ends. LT catalyzes intramolecular reactions resulting in the concomitant formation of a1,6-anhydroMurNAc residue and GlcNAc with a non-reducing end. Peptidases are classified into amidases, carboxypeptidases, and endopeptidases based on the position of the cleavage amide bond. *N*-acetylmuramoyl-L-alanine amidases cleave the bond between L-Ala and the lactyl group of MurNAc, producing a denuded glycan backbone with a lactate moiety. Carboxypeptidases are exolytic peptidases that remove the C-terminal amino acid from the peptide stem. Endopeptidases refer to endolytic peptidases that cleave the amide bond within the peptide. Based on the chiral center (D or L) of the residues that compose the amide bond, these enzymes can be further grouped as DD-, LD-, and DL-carboxypeptidases or DD-, LD-, and DL-endopeptidases.

The GlcNAc and MurNAc residues may be chemically modified to prevent hydrolysis from environmental sources or to escape host immune systems (98). *N*-acetylglucosamine deacetylase and *N*-acetylmuramic acid deacetylase remove the acetyl group from GlcNAc and MurNAc residues, respectively. The acetyl group at the C2 position of these sugars is hydrolyzed, producing an amine group and releasing the acetate. Interestingly, the *N*-acetylmuramic acid deacetylase PdaA from *Bacillus subtilis* was proposed to catalyse both deacetylase and transpeptidase activity as it was required for muramic delta-lactam production

(99). *O*-acetyltransferases produce *O*-acetylated PG by adding acetyl groups to MurNAc or GlcNAc residues. *O*-acetylation on PG GlcNAc is less common. An example enzyme for this modification is the *Lactobacillus plantarum* *O*-acetyltransferase OatB, the *O*-acetylated PG from OatB catalysis is more resistant to an autolysin Acm2 activity (100).

1.3 Curved and helical shape maintenance mechanisms

1.3.1 MreB directs rod shape formation in bacteria

The generation of rod-shaped bacteria depends on PG synthesis complexes called the divisome and elongasome (**Figure 1-5**). Each complex contains a multitude of transmembrane and periplasmic proteins that conduct synthetic and hydrolytic activities for new PG insertion (101). Assembly of the divisome and elongasome complexes requires scaffold proteins. In *Escherichia coli*, the divisome is organized by a tubulin-like cytoskeleton protein named FtsZ, and this synthesis machinery facilitates formation of the division septum and cytokinesis. FtsZ is responsible for cell length control as the cells become filamentous when expressing FtsZ at a low level (102). The elongasome is organized by a eukaryotic actin-like filament called MreB, which helps to insert new PG along the lateral side-wall of the cell as it grows.

MreB presence has an interesting correlation with rod shape. MreB and homologs (e.g., Mbl and MreBH) are found in rod shaped bacteria (e.g., *E. coli* and *B. subtilis*) and curved rod bacteria (e.g., *C. crescentus* and *V. cholerae*), whereas MreB is absent in cocci and ovococci (e.g., *S. aureus* and *S. pyogenes*) (103). Two spherical strains of *E. coli* had mutations in the *mre* gene region, and the rod shape was restored by complementing *mre* gene fragments (104). Gradual reduction of MreB protein expression in *E. coli* demonstrated a morphology transition

from rod shape to coccoid shape (105). MreB isoforms in *B. subtilis* also showed its importance in the rod shape determination (106,107).

MreB is a membrane associated scaffolding protein. MreB displays a four-domain architecture, which is a structural homolog of the filament protein F-actin (108). Each MreB polymerizes in the presence of ATP or GTP to form protofilaments. Two protofilaments pack against each other in an anti-parallel fashion. The N-terminal amphipathic regions of MreB monomers are exposed at the same side of the MreB polymer, constituting a membrane binding plane that docks onto the cytoplasmic membrane (109,110). These filaments can assemble into sheets under various chemical conditions (111), and were first visualized as “helical cables” wrapped along the long axis of the *B. subtilis* by immunofluorescence microscopy (106). The “helical cable” of MreB was later suggested to be an artifact. Total internal reflection fluorescence microscopy (TIRFM) demonstrated that the MreB structure was made of protein patches that moved bi-directionally along linear tracks perpendicular to the long axis of the cell (112,113) (**Figure 1-5**). Together, MreB is a dynamic object that moves circumferentially along the long cell axis.

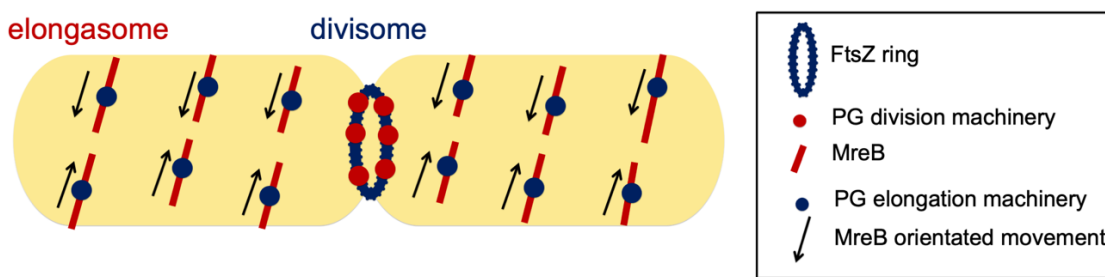


Figure 1-5. Cellular positions of divisome and elongasome complexes

Maintenance of a rod shape in *E. coli* requires both a divisome and elongasome. Both synthesis complexes recruit PG synthesis machinery which inserts new PG. The divisome is organized by a FtsZ cytoskeleton that forms a ring at the septum. The elongasome is guided by MreB which moves parallel to the short cell axis.

MreB promotes a higher PG synthesis rate along the long cell axis versus the short cell axis by recruiting elongasome complexes. These complexes are composed of proteins such as MreC, MreD, RodZ, RodA, PBP2, PBP1A (naming in *E. coli*) for PG elongation and cross-linking (101,114). Some of these proteins exhibit same orientated movement of MreB (112,113). Also, new PG insertion sites share a similar localization pattern of MreB in the rod cell (115,116). Adding fluorescent labelled vancomycin, an antibiotic that targets terminal D-Ala-D-Ala in nascent PG, to *B. subtilis* cells displayed transverse bands along the long axis of the cell. These studies support that MreB works with PG biosynthesis enzyme to insert new PG along long cell axis.

1.3.2 *Caulobacter crescentus* CreS

Caulobacter crescentus is Gram-negative bacteria with a curved rod shape. Its cell shape is maintained by MreB and CreS (117,118). CreS was first identified from a transposon insertion mutants library (118). Two mutants with straight shapes had insertions at 228 bp downstream and 15 bp upstream of the start codon of the *creS* open reading frame. Complementation with wild-type *creS* restored the curved shape in a straight mutant, confirming that CreS is a shape determining protein.

CreS is a filament forming protein that shares domain architecture with eukaryotic intermediate filament-like proteins (118). CreS consists of an N-terminal head domain, a central coiled-coil rod domain, and a C-terminal tail domain. The majority of the protein consists of the rod domain which is composed of coiled-coil segments interspersed by linkers. Each coiled-coil segment consists of predicted heptad repeats, in which the a and d position of the 7 residues (named a, b, c, d, e, f, and g) are hydrophobic, whereas b, c, e, g, f are hydrophilic residues. The heptad containing helices can polymerize through interactions between the

hydrophobic residues, which likely explains the filamentation formation of purified CreS protein *in vitro* (118).

CreS filament proteins were shown to be localized along the inner curvature of the asymmetric cell, and were excluded from the pole (119). The N-terminal basic residues of CreS anchored the protein to the cytoplasmic membrane (120). The CreS membrane association also involves cell wall structure. A strain which lacks β -lactamase encoding-gene (Δbla) is sensitive to the β -lactam antibiotic mecillinam (an antibiotic that targets cell wall synthesis). Expression of a CreS-GFP fusion protein in the Δbla strain upon mecillinam treatment showed CreS dislodged from the membrane. CreS binding to the membrane was hypothesized to exert a compressive force which bends the cell wall to form a curved shape. However, interruption of the CreS filament network by halting cell growth using chloramphenicol did not make the curved cell straight (120). Active cell growth is thus hypothesized to be required for CreS to induce a curved shape. Monitoring of the PG synthesis rate by pulse-chase PG labeling in wild-type and $\Delta creS$ strains showed an asymmetrical cell wall growth rate in the curved wild-type strain but not the $\Delta creS$ strain. To summarize, the inner curvature localization of CreS leads to inhibition of the local cell wall growth and generates the curved shape (120).

Proteins which are involved in CreS localization are important for generating the curved shape. *WbqL* is involved in the lipopolysaccharide (LPS) biosynthesis pathway. Deletion of *wbqL* resulted in dissociation of CreS from the membrane, resulting a straight cell shape (121). Cytidine triphosphate synthetase (CtpS) forms a filament structure that colocalizes with CreS in the cell. Overexpression of CtpS disrupted the inner curvature localization of CreS, also leading to straight cells (122).

1.3.3 *Vibrio cholerae* CrvA

Vibrio cholerae is a curved-rod Gram-negative bacterium. Similar to *C. crescentus*, the curved rod shape is maintained by a filament protein CrvA. CrvA was identified by a visual screening of straight cells from a Tn5 transposon insertion library (123). In-frame deletion of *crvA* produced straight cells and complementation restored curvature. Induction of cell curvature requires an appropriate protein level of CrvA and the presence of the accessory protein CrvB. CrvA level is regulated by quorum sensing and the concentration of cyclic di-GMP (123,124). Increased cyclic di-GMP in cells caused reduction of CrvA expression accompanied by straight morphology. Recombinant expression of CrvA and the downstream gene CrvB together in the straight-rod species *Escherichia coli* and *Pseudomonas aeruginosa* induce curved rod shapes (125).

Unlike CreS, which is a cytoplasmic filament, CrvA is a periplasmic filament containing an N-terminal signal peptide sequence, two coiled-coil domains, and a PEGA-like C-terminal domain (123). Each domain of CrvA is important for full protein function as suggested by a complementation study to a CrvA deletion strain using truncated proteins (123). CrvA is localized at the inner curvature of the cell surface. Asymmetrical CrvA localization seems to cause differential cell wall synthesis rates at the inner and outer curved faces in *V. cholerae*. The synthesis rate is determined by the rate of old PG removal and the rate of new PG insertion. A two-color pulse-chase experiment using fluorescent D-amino acids provides the rate of the decay of old PG (labeled by HCC-amino-D-alanine, $\lambda_{em} \approx 450$ nm) and the insertion of new PG (labeled by NBD-amino-D-alanine, $\lambda_{em} \approx 550$ nm). The rate of PG removal is similar between the inner curvature and outer curvature of a cell, but the rate of PG insertion at the inner curvature is slower than at outer curvature. Such asymmetrical cell wall insertion

rates were not observed in $\Delta crvA$. Thus, CrvA likely imposes a negative impact on PG insertion at the inner curvature of a cell leading to curved rod cells.

1.3.4 Multifactorial shape system in *Helicobacter pylori*

H. pylori is helical or spiral-shaped Gram-negative bacterium. Screening of strains with morphology defects identified eight nonessential and nonredundant genes that are required for helical shape (52,126-129). These genes encode both nonenzymatic scaffolding proteins (Csd2, Csd5, Csd7 and CcmA) and PG hydrolases (Csd1, Csd3/HdpA, Csd4, Csd6), suggesting that cell wall remodeling, apart from PG synthesis, helps to generate helical morphology of *H. pylori*.

Curvature analysis shows *H. pylori* has alternate positive and negative Gaussian curvatures along the sidewall (130). Gaussian curvature is defined as $K = \kappa_1 \times \kappa_2$, where κ_1 and κ_2 are the two principal curvatures (131) (**Figure 1-6**). The principal curvatures are derived from two planes which intersect at a point on the surface to produce a radius with a curvature of absolute maximum and absolute minimum. Zero Gaussian curvature ($K = 0$) occurs when one of the two principal curvatures is zero. For example, the surface along the long axis of a rod cell has zero Gaussian curvature. Positive Gaussian curvature ($K > 0$) is when the two principal curvatures have the same sign, meaning the two curvatures bend in same direction. Regions with positive Gaussian curvature include the whole cell surface of a spherical bacterium, the pole area of a rod cell, and the outer curved face of a vibrioid cell. Negative Gaussian curvature ($K < 0$) describes when the two principal curvatures have the opposite sign, meaning the two curvatures bend in opposite directions at the point. An example of negative Gaussian curvature is the inner curved face of a vibrioid cell.

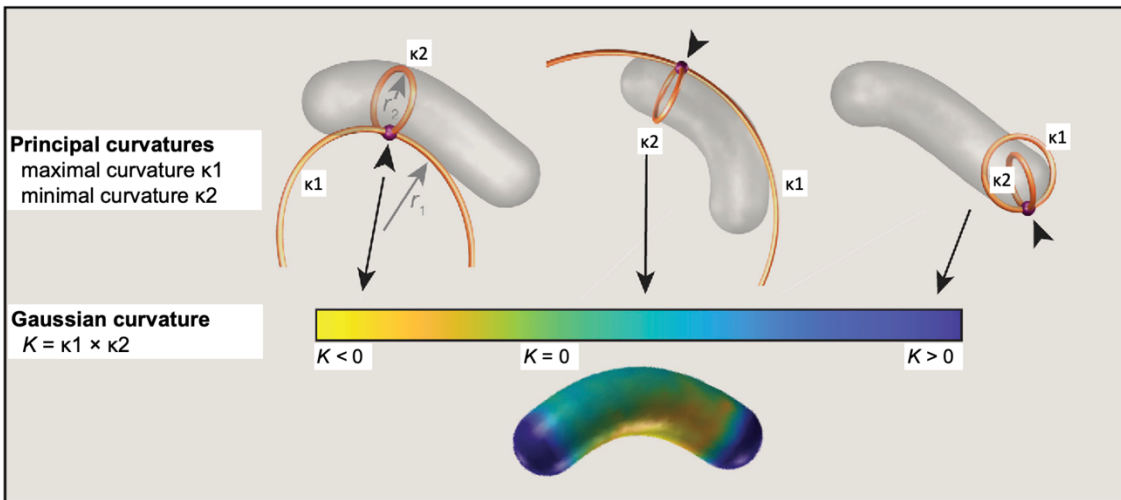


Figure 1-6. Regions of a cell with measured Gaussian curvatures

The curvature of each point on the cell surface can be measured by Gaussian curvature K , where K is determined by the two principal curvatures κ_1 and κ_2 . The maximal principal curvature κ_1 is derived from the largest radius of a circle that intersects at a surface point, whereas the minimal curvature κ_2 is derived from the smallest radius of a circle. Three selected regions of a cell surface displaying different Gaussian curvature values are shown (top). The surface of the cell pole (top right) represents strong positive Gaussian curvature. The outer curved face (top middle) and inner face (top left) of a vibrioid cell represent positive and negative Gaussian curvatures, respectively. The Gaussian curvature can be mapped onto the surface of a bent cell using a color scale (bottom). This figure is adapted and modified from the literature (131)

CcmA is a bactofilin homolog with no predicted enzyme activity (52). Purified CcmA formed filaments that assembled into helical bundles and lattice structures *in vitro*, confirming that CcmA is a cytoskeleton-like protein (130). An immunofluorescence localization study showed that CcmA exhibited as puncta along the cell, and was localized to positive Gaussian curvature in *H. pylori* (130). Moreover, CcmA showed co-localization with sites of new PG insertions. The use of alkyne (alk) functionalized PG precursors (MurNAc-alk or D-Ala-alk) during cell growth showed that the new PG was excluded from the poles but was relatively concentrated at regions of both negative and positive Gaussian curvatures (130). Particularly, signals of MurNAc-alk labeled PG aligned to Gaussian curvature at around $6 \mu\text{m}^{-2}$, similar to the localization of CcmA. The curvature enrichment pattern of MurNAc-alk labeled PG was

diminished in the absence of CcmA. It is hypothesized that CcmA localizes at positive Gaussian curvature and could promote local PG synthesis that maintains helical shape (130).

CcmA is proposed to form a “shapesome” complex with the shape determining proteins (Csd1, Csd2, Csd7, Csd5). The muropeptide profiles derived from bacterial strains with single gene deletions of *ccmA*, *csd7*, *csd1* and *csd2* shared similar changes of wild-type are similar and distinct from that of the wild-type *H. pylori* strain (52,128). This multiple protein complex is likely centered on Csd7. Csd7 is a predicted polytopic integral membrane protein and shown to interact with Csd1 and Csd2 by co-immunoprecipitation. Also, the protein levels of Csd1 and Csd2 in a Δ *csd7* strain were decreased, suggesting co-stability dependence of these proteins. The protein expression levels of Csd2 in Δ *csd1* and Csd1 in Δ *csd2* were largely reduced, suggesting Csd1 and Csd2 stability were mutually dependent (128). Csd1 is an M23 family peptidase with a LytM catalytic domain that cleaves 4-3 cross-linkages in PG (52). Csd2 is catalytically inactive due to a Glu residue replacement of a His residue that coordinates a catalytic metal (52,132). Csd1 and Csd2 form a heterodimer in solution and in the crystal structure (132). A direct interaction of Csd1 and Csd2 was validated using the bacterial two-hybrid assay (128).

Csd7 also precipitated CcmA from *H. pylori* cell lysate in an immunoprecipitation assay (128). A link between CcmA and Csd5 was found because CcmA was immunoprecipitated by Csd5 from the cell lysate (133). Csd5 is predicted to be a scaffolding protein; however, deletion of *csd5* did not cause a muropeptide profile change in *H. pylori* (126). Csd5 contains an N-terminal tail, a transmembrane (TM) domain, a coiled-coil motif, and a C-terminal PG binding SH3 domain (133). The TM domain of Csd5 is important for interaction with CcmA and a PG precursor synthase, MurF (133). Together, this work supports

the hypothesis that shape-determining proteins form a multiple protein complex. This “shapesome” might promote PG growth at regions with positive Gaussian curvatures to induce the helical-shape of *H. pylori*.

Three PG hydrolases (Csd3/HdpA, Csd4, and Csd6) are involved in helical cell shape and these proteins were not shown to have an interaction with the CcmA associated “shapesome”. Csd3/HdpA is an M23 family peptidase with a characteristic LytM domain (134). Csd3 was shown to cleave 4-3 cross-linkage of tetra-pentapeptides or to remove the terminal D-Ala from pentapeptides (52,129). Deletion of *csd3* resulted in pleomorphic morphologies (52,129). Csd4 is a DL-carboxypeptidase that removes *m*-Dap from tripeptides (126,135,136) and Csd6 is a LD-carboxypeptidase that removes D-Ala from tetrapeptides (127,137). Deletion of either *csd4* or *csd6* resulted in straight cells (126,127,135). The mechanism by which Csd3, Csd4 and Csd6 lead to helical shape is unclear. As DD-transpeptidase catalyzes 4-3 cross-linkage using pentapeptide and tetrapeptide substrates, it is hypothesized the peptide trimming by Csd4 and Csd6 would reduce the availability of these substrates for cross-linking. However, the percentage of cross-linked murotetrapeptide and monomeric muropeptide were not changed in $\Delta csd4$ and $\Delta csd6$ strains. Spatial reduction of cross-links by these proteins is proposed to introduce PG structure relaxation for helical shape generation (52). Alternatively, Csd3, Csd4 and Csd6 could be involved in local PG insertion and turnover rate, creating differential PG homeostasis along the cell surface. More studies on activity regulation and protein localization of these proteins are needed for a full understanding of the helical shape maintenance system.

1.4 *C. jejuni* helical shape generation

1.4.1 The *C. jejuni* helical cell shape determining proteins

As mentioned earlier in the introduction, the known shape-determining genes in *C. jejuni* identified by genetic screening include *pgp1*, *pgp2*, *pgp3*, *1228*, *1105* and *ape1*. These genes were identified by genetic deletion and identifying morphological deviation from the helical wild-type. Different from using spatial PG synthesis for maintaining the bent morphology in *C. crescents*, *V. cholerae*, and *H. pylori*, the identified *C. jejuni* shape determining genes so far function in PG modification (**Figure 1-7 and Figure 1-8**).

A *C. jejuni* strain with a deletion of *pgp1* (46) has a straight cell morphology. The $\Delta pgp1$ mutant displayed a rod shape similar to *B. subtilis* and *E. coli*. *C. jejuni* strain RM1285 is a rod-shaped cell with a nonsense point mutation in *pgp1* (138) and the loss of helical shape is likely due to deficient Pgp1 protein. Pgp1 is a DL-carboxypeptidase that cleaves *m*-Dap from murotripeptides to produce murodipeptides (46). The muropeptide profile from PG isolated from the $\Delta pgp1$ strain exhibited increased tripeptide, decreased dipeptide and decreased tetrapeptide when compared with the wild-type. Incubation of purified PG from strain $\Delta pgp1$ with recombinant Pgp1 resulted in decreased tripeptide and increased dipeptide, and the reaction was inhibited in the presence of EDTA, suggesting Pgp1 is a metal dependent hydrolase.

A *C. jejuni* ATCC 33560 strain with a deletion of *pgp3* exhibits curved-rod (50). Pgp3 is a bifunctional M23 metalloprotease with DD-carboxypeptidase and DD-endopeptidase activities (50). Recombinant Pgp3 cleaved the terminal D-Ala from a monomeric pentapeptide, cleaved the 4-3 cross-linkage in synthesized cross-linked tetratripeptide, and in isolated *Escherichia coli* sacculus. The Pgp3 structure contains an N-terminal immunoglobulin-like

domain, LytM domain, and a C-terminal helix (50). The catalytic LytM domain is found in two other PG hydrolases: lysostaphin and DD-endopeptidase (139,140). LytM structures show a large antiparallel beta-sheet and a conserved Zn²⁺-ion-binding motif (HxxxD and HxH) in the active site (50,132,134). The zinc ion is proposed to polarize the carbonyl oxygen of the scissile bond so that the carbonyl carbon is susceptible to nucleophilic attack by water (140). Replacement of Zn²⁺ coordinating residues abolishes Zn²⁺ binding in the active site and forms an inactive LytM domain. Examples are *E. coli* EnvC and *H. pylori* Csd2 (132,141). This inactive LytM domain can interact with PG hydrolases and function as a regulatory protein involved in peptidoglycan biogenesis (142).

Strains with a deletion of *CJJ81176_1228* (53) or *CJJ81176_1105* (51) exhibit curved-rod morphology. The proteins expressed from these genes, 1228 and 1105, are predicted LytM containing M23 metalloproteases. These enzymes are predicted to cleave the 4-3 cross-linkage between *m*-Dap and D-Ala. The biochemical activities of the 1128 and 1105 proteins are not yet reported. The homologous proteins in *H. pylori* are the endopeptidases Csd3 and Csd1, respectively (51,53). Based on homology, 1228 consists of a Csd3N-terminal domain and a LytM domain (53), and 1105 contains prefoldin (300 amino acids), coiled-coil, and C-terminal LytM domains (51).

Curved Shape Determining Proteins	<i>C. crescentus</i>	<i>V. cholerae</i>	<i>H. pylori</i>	<i>C. jejuni</i>
Filaments	CreS	CrVA CrVB	CcmA	
Remodeling enzymes			Csd1 (DD-EPase) Csd3 (DD-EPase) Csd4 (DL-CPase) Csd6 (LD-CPase)	Pgp1 (DL-CPase) Pgp2 (LD-CPase) Pgp3 (DD-EPase) 1105 (DD-EPase) 1228 (DD-EPase) Ape1 (OAc-esterase)
Scaffold proteins			Csd2 Csd5 Csd7	

Figure 1-7. Comparison of cell shape determining proteins in curved and helical bacteria.

The known curved and helical shape determining proteins are classified into filaments, remodelling enzymes and scaffold proteins. The curved shapes of *C. crescentus* and *V. cholerae* are maintained by filament proteins (CreS, CrvA and CrvB) localized at the inner-curvature side of the cell, leading to asymmetric PG growth rate. The helical shape of *H. pylori* is maintained by the filament protein CcmA localized at regions of positive Gaussian curvature. In addition to CcmA, *H. pylori* helical shape is maintained by PG hydrolases and scaffold proteins. The known proteins required for helical shape of *C. jejuni* are PG hydrolases and the *O*-acetyl esterase Ape1.

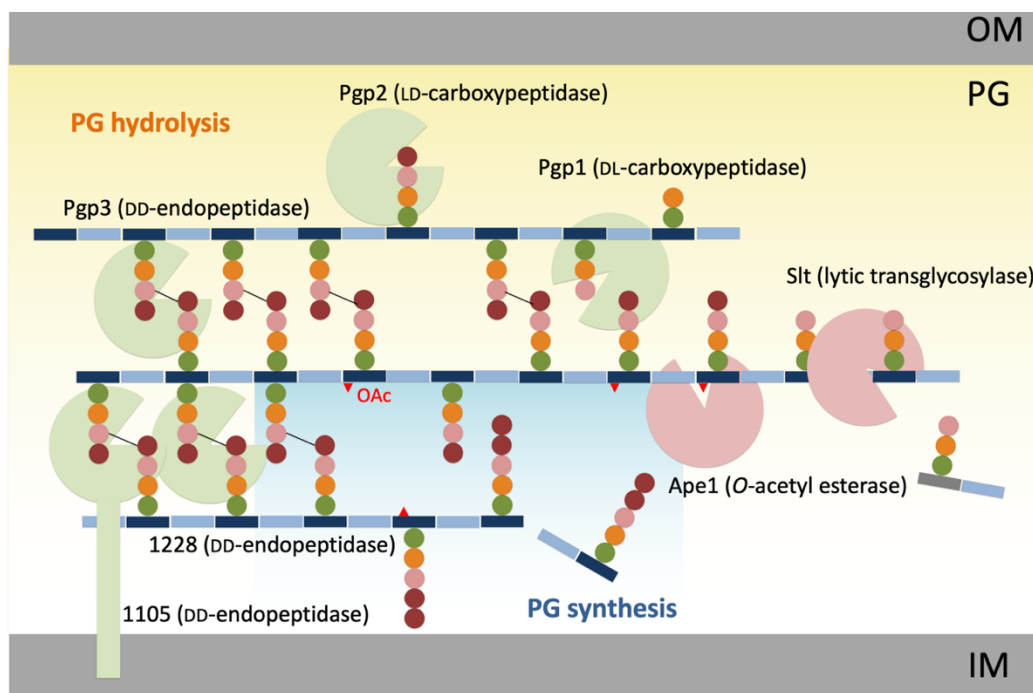


Figure 1-8. Schematic of cell shape maintenance proteins used by *C. jejuni*

Helical shape is maintained by hydrolysis by PG-modifying enzymes. In mature PG, the cross-linkages of the sacculus are digested by Pgp3, 1105 and 1228 (DD-endopeptidases). Additionally, the peptides are trimmed to tetra- and tri-peptides by Pgp2 (LD-carboxypeptidase) and Pgp1 (DL-carboxypeptidase). *O*-acetyl groups (OAc) are removed by Ape1 (*O*-acetyl esterase). The de-acetylated PG can be digested by Slt (lytic transglycosylase).

1.4.2 The LD-carboxypeptidase Pgp2

C. jejuni pgp2 is a major shape determining gene. Whole genome sequencing of rod-shaped strains from a transposon mutant library (~1933 mutants) and from laboratory passages found the rod-shaped strains all contained nucleotide perturbations in the *pgp2* or *pgp1* (47,48). The morphology of a strain with *pgp2* gene deletion looks like a football, mostly rod shape with narrow-ends at the poles.

Pgp2 is a LD-carboxypeptidase that cleaves D-Ala from tetrapeptides into tripeptides (49). The muropeptide of PG purified from strain $\Delta pgp2$ contains no tripeptides. Incubation of $\Delta pgp2$ PG with recombinant Pgp2 showed decreased levels of tetrapeptides and increased levels of tripeptides. The tripeptide product of Pgp2 cleavage is the substrate for Pgp1, and a $\Delta pgp1 pgp2$ strain shares a similar muropeptide profile to that of the $\Delta pgp2$ strain (49). Sequence analysis of Pgp2 indicates that it contains an LD-carboxypeptidase (LD-CPase) domain and an NTF2-like superfamily (NTF2) domain. NTF2 domains are broadly found in nature and function in both ligand binding and catalysis. Interestingly, NTF2 domains are found in PG hydrolases such as PBP2a and NlpC/p60 in addition to their catalytic domains (143,144). No biochemical study of the NTF2 domain in Pgp2 or in other PG hydrolases has been reported.

Orthologs of Pgp1 and Pgp2 are characterized in *Helicobacter pylori*, and both are required for maintaining helical cell shape (126,127). The *H. pylori* homolog of Pgp2 is named Csd6 and shares 36% amino acid sequence identity. Csd6 is suggested to be required for flagellin biosynthesis in *H. pylori* (145). Flagellin in *H. pylori* is modified by the addition of pseudaminic acid. Interestingly, purified flagellin A from a $\Delta csd6/HP0518$ strain contained higher levels of pseudaminic acid than in the wild-type strain. Subsequently, a crystal structure

of a Csd6 dimer was solved and pseudaminic acid was modeled bound to a pocket within the NTF2 domain (137). Nonetheless, direct evidence for pseudaminic acid binding by Csd6 is weak and this function is unconnected to a well-defined role of Csd6 in cleaving PG tetrapeptide stems as observed for Pgp2. A possible role of the NTF2 domain in either Pgp2 or Csd6 in binding PG has not yet been tested.

1.4.3 The *O*-acetyl-esterase Ape1

O-acetylation at the C6 hydroxyl group of MurNAc serves in a protective role to resist cell lysis by lysozymes produced by mammalian innate immune systems. Pathogens such as *Staphylococcus aureus*, *Enterococcus faecalis*, *Listeria monocytogenes* and *Neisseria gonorrhoeae* that contain *O*-acetylated PG are found to be more resistant to lysozymes (146-149). The level of PG *O*-acetylation is determined by enzymes encoded by the O-acetylation of peptidoglycan (OAP) regulon (150). In Gram-positive bacteria, the bi-functional protein OatA translocates cytoplasmic acetyl moieties to the periplasm and acetylates the C6 hydroxyl group of PG MurNAc (151,152). In Gram-negative bacteria, a two-component system, PatA and PatB, perform the activities of OatA (153-155). The OAP regulon encodes a third gene named *ape1*. Ape1 is a periplasmic *O*-acetyl esterase that hydrolyzes *O*-acetylated MurNAc within the PG polymer to produce de-*O*-acetylated MurNAc (156). De-*O*-acetylation by Ape1 is proposed to regulate PG turnover by LTs (157), which can only cleave the β -(1-4)-glycosidic bond between de-*O*-acetylated MurNAc and GlcNAc to generate glycan stands with an 1,6-anhydroMurNAc end (158).

C. jejuni ape1 contributes to the generation of a helical shape. Strains with *ape1* deleted exhibit highly curved cells. *O*-acetylated peptides increased from 2% to 10% from wild-type to Δ *ape1* cells. Ape1 belongs to the serine esterases and lipases of the GDSL family (150).

This enzyme family contains a catalytic Ser in one of three the conserved motifs: GxSxG, GDSL, and GDS (159). A subgroup of the GDSL family is further classified as the SGNH hydrolase superfamily due to presence of invariant residues Ser, Gly, Asn and His (160). Ape1 is predicted to contain the catalytic triad Ser, His, and Asp. Opposite the triad are Gly and Asn residues that form the oxyanion hole for transition state stabilization in the active site (161,162). Mutagenesis of the *N. gonorrhoeae* Ape1 homolog demonstrated that these conserved catalytic residues are required for enzyme activity (156,161,162). The *N. meningitidis* Ape1 crystal structure contains a catalytic domain with an α/β -hydrolase fold of the SGNH superfamily (163). The authors observed that the presence of an acetyl moiety rotates the Ser nucleophile by 90° to be positioned for optimal catalysis and proposed a substrate-induced mechanism as to prevent accidental de-*O*-acetylation. *N. gonorrhoeae* Ape1 was reported to have higher specific activity towards *O*-acetylated PG compared to *O*-acetylated xylan (156), suggesting that the enzyme may recognize additional substrate components beyond the acetate. *C. jejuni* Ape1 is predicted to contain a carbohydrate binding module of family 35 (CBM35) domain in addition to the SGNH domain. The CBM35 domain is typically found in plant cell wall degrading enzymes (164,165). The role of such domains was proposed to be involved in substrate specificity (163).

1.5 Objectives of this thesis

Helical shape increases the success of *C. jejuni* host colonization. Chicken, the natural reservoir of *C. jejuni* is considered to be the major transmission route of campylobacteriosis in humans. It has been proposed that cell shape disruption is a potential method for reducing the bacterial load in chicken (166,167). Despite the identification of six genetic elements responsible for helical shape in *C. jejuni*, few structural studies are known for these important

enzymes. Furthermore, it remains unclear whether the interaction of peptidoglycan with these shape enzymes contributes to the selection of sites on the PG for cleavage for helical shape generation. In this thesis, I performed structural, biochemical and genetic studies on the two helical shape determining enzyme: Pgp2 (Chapter 3) and Ape1 (Chapter 4). This work aims to define the functional regions of Pgp2 and Ape1 required for enzyme activity. These studies add to our knowledge of the mechanism of helical shape generation in *C. jejuni*. The protein structures and the identification of accessory PG binding sites could serve as a foundation to develop morphology-targeting inhibitors that reduce the prevalence of campylobacteriosis.

CHAPTER 2: Materials and methods

2.1 Bacterial strains and growth conditions

2.1.1 *E. coli*

E. coli was used for plasmid cloning and protein expression. *E. coli* cultures were grown at 37 °C or 25 °C in Luria Bertani (LB) broth or on LB agar under aerobic condition. Appropriate antibiotics ampicillin (125 µg/ml), kanamycin (25 µg/ml), chloramphenicol (20 µg/ml) were included in growth media for selectivity. Strains of *E. coli* used in this study are listed in **Table 2-1**.

2.1.2 *C. jejuni*

C. jejuni strains 81-176 wild-type, $\Delta pgp2$, $\Delta ape1$ and $\Delta pgp2$ complementation with point mutations were used for cell shape analysis and peptidoglycan preparation. *C. jejuni* were grown at 38 °C on Mueller-Hinton (MH; Oxoid) media agar under microaerophilic conditions (12% CO₂, 6% O₂, in N₂) in a Sanyo tri-gas incubator. For shaking MH broth culture, *C. jejuni* was cultured in airtight jars using the Oxoid CampyGen Atmosphere generation system with shaking at 200 rpm. Appropriate antibiotics chloramphenicol (20 µg/ml), vancomycin (10 µg/ml) and trimethoprim (5 µg/ml) were included in growth media. Strains of *C. jejuni* used in this study are listed in **Table 2-1**.

Table 2-1. Bacterial strains used in this study

Bacteria	Strain name	Description	Reference
<i>C. jejuni</i>	81-176	An isolate from a raw-milk diarrhea outbreak	(168)
<i>C. jejuni</i>	Δ ape1	<i>C. jejuni</i> strain 81-176 with an <i>ape1</i> deletion	(54)
<i>C. jejuni</i>	Δ pgp2	<i>C. jejuni</i> strain 81-176 with a <i>pgp2</i> deletion	(49)
<i>C. jejuni</i>	Δ pgp2 ^C	Strain Δ pgp2 complemented with a copy of <i>pgp2</i> integrated at one of three 16S ribosomal regions found in <i>C. jejuni</i>	(49)
<i>C. jejuni</i>	H157A	Δ pgp2 complemented with mutant of the catalytic triad	Chapter 3
<i>C. jejuni</i>	C174S	Δ pgp2 complemented with mutant of the catalytic triad	Chapter 3
<i>C. jejuni</i>	Y233A	Δ pgp2 complemented with mutant within the NTF2 pocket	Chapter 3
<i>C. jejuni</i>	F242A	Δ pgp2 complemented with mutant within the NTF2 pocket	Chapter 3
<i>C. jejuni</i>	K257A	Δ pgp2 complemented with mutant within the NTF2 pocket	Chapter 3
<i>C. jejuni</i>	K307A	Δ pgp2 complemented with mutant within the NTF2 pocket	Chapter 3
<i>C. jejuni</i>	E324Q	Δ pgp2 complemented with mutant within the NTF2 pocket	Chapter 3
<i>E. coli</i>	DH5 α	General strain for plasmid propagation. Contains the <i>recA1</i> mutation for insert stability and the <i>endA</i> mutation for high yield.	Life Technologies
<i>E. coli</i>	BL21(DE3)	A common strain for protein expression. Contains an integrated bacteriophage DE3 with T7 polymerase gene inducible by IPTG. Suitable for expression of target protein with a T7 promoter.	Novagen
<i>E. coli</i>	BL21-Pgp2	<i>E. coli</i> BL21(DE3) strain harboring plasmid pET15b-Pgp2 ⁴³⁻³²⁵	Chapter 3
<i>E. coli</i>	BL21-Pgp2 ^{K307A}	<i>E. coli</i> BL21(DE3) strain harboring plasmid pET15b-Pgp2 ^{K307A}	Chapter 3
<i>E. coli</i>	BL21-Ape1 ²²⁻³⁹²	<i>E. coli</i> BL21(DE3) strain harboring plasmid pET28a-Ape1 ²²⁻³⁹²	Chapter 4
<i>E. coli</i>	BL21-Ape1 ⁴¹⁻³⁹²	<i>E. coli</i> BL21(DE3) strain harboring plasmid pET28a-Ape1 ⁴¹⁻³⁹²	Chapter 4
<i>E. coli</i>	BL21-Ape1 ^{K103A}	<i>E. coli</i> BL21(DE3) strain harboring plasmid pET28a-K103AApe1 ²²⁻³⁹²	Chapter 4

<i>E. coli</i>	BL21-Ape1 ^{Y104G}	<i>E. coli</i> BL21(DE3) strain harboring plasmid pET28a-Ape1 ^{Y104G}	Chapter 4
<i>E. coli</i>	BL21-Ape1 ^{Q105A}	<i>E. coli</i> BL21(DE3) strain harboring plasmid pET28a-Ape1 ^{Q105A}	Chapter 4
<i>E. coli</i>	BL21-Ape1 ^{Q106A}	<i>E. coli</i> BL21(DE3) strain harboring plasmid pET28a-Ape1 ^{Q106A}	Chapter 4
<i>E. coli</i>	BL21-Ape1 ^{N121A}	<i>E. coli</i> BL21(DE3) strain harboring plasmid pET28a-Ape1 ^{N121A}	Chapter 4
<i>E. coli</i>	BL21-Ape1 ^{S122A}	<i>E. coli</i> BL21(DE3) strain harboring plasmid pET28a-Ape1 ^{S122A}	Chapter 4
<i>E. coli</i>	BL21-Ape1 ^{R123A}	<i>E. coli</i> BL21(DE3) strain harboring plasmid pET28a-Ape1 ^{R123A}	Chapter 4
<i>E. coli</i>	BL21-Ape1 ^{F132A}	<i>E. coli</i> BL21(DE3) strain harboring plasmid pET28a-Ape1 ^{F132A}	Chapter 4

2.2 Strain construction

2.2.1 Complementation of $\Delta pgp2$

Complementation of $\Delta pgp2$ was achieved using a *pgp2* complementation plasmid (49).

The *pgp2* gene and promoter were amplified from *C. jejuni* 81-176 genomic DNA and cloned into the pRRC vector (169). The inserted *pgp2* gene included 196 bp of the native promoter region and 190 bp of the downstream sequence. The complementation plasmid was integrated into an available strain 81-176 $\Delta pgp2$ mutant (49) by natural transformation. The transformed *C. jejuni* cells were grown at 38 °C under microaerophilic conditions in a tri-gas incubator. Colonies were selected on MH-TV (Mueller-Hinton containing trimethoprim and vancomycin) plates with chloramphenicol. Recombination into the chromosome was verified by PCR analysis using primers Spe1, 198R, 554F, and cat-2. Construction of variant Pgp2 mutant strains was achieved by site-directed mutagenesis of the wild-type complementation plasmid. The primers used in this study are listed in **Table 2-2**. Constructed plasmids are listed in **Table 2-3**.

Table 2-2. List of primers used in this study

Name of Primer	Primer sequence (5' to 3') ^a
pRRC_C174S (F)	TAAAACAAGAGGA <u>A</u> GTATTGCTTATT
pRRC_C174S (R)	AATAAAGCAATA <u>C</u> TCCTCTGTTTA
pRRC_H157A (F)	GTGGTATTGGATC <u>G</u> CTGGCTATCCTTAG
pRRC_H157A (R)	CTAAAGGATAGCC <u>A</u> CGATCAAATACCAC
pRRC_Y233A (F)	GTGACACTAATACC <u>G</u> CTTAAGTTTATG
pRRC_Y233A (R)	CATAAAA <u>A</u> CTTAA <u>G</u> CGGTATTAGTGTAC
pRRC_F242A (F)	GATGAGCAAGAAG <u>C</u> TAACGTTTGAT
pRRC_F242A (R)	ATCAAAACGTT <u>A</u> G <u>C</u> TTGCTCATC
pRRC_K257A (F)	TTGCTTCCAT <u>G</u> CAA <u>A</u> ATCTATT
pRRC_K257A (R)	AAAATAGATT <u>T</u> <u>G</u> CATGGAAGCAAA
pRRC_K307A (F)	CAGTTAGAGGCGAT <u>G</u> CAATTATACGTTAAG
pRRC_K307A (R)	CTTAACGTATAAA <u>A</u> TT <u>G</u> CATGCCTCTAAACTG
pRRC_E324A (F)	GAAAATT <u>T</u> AGCAC <u>A</u> GAATAATGTC
pRRC_E324A (R)	GACATTATTGCT <u>G</u> TGCTAAAATTTC
Spe1	GCGACTAGTTGCC <u>T</u> AAAAAAGACATTCTATAAA
198R	TTAATAAAGCAAGTCGTTTAACAA
554F	AGGCCGTAA <u>G</u> TTAATCCAGGTGA
cat-2	TTTTTTGGATGAATTACAAGA
Pgp2 ⁴³⁻³²⁵ (F)	GGGAATT <u>C</u> <u>C</u> <u>A</u> <u>T</u> <u>G</u> CAAAAGGATT <u>T</u> GGTTAAGT
Pgp2 ⁴³⁻³²⁵ (R)	CCCG <u>C</u> <u>T</u> <u>C</u> <u>G</u> <u>A</u> TT <u>G</u> C <u>T</u> <u>C</u> <u>G</u> CTAA <u>A</u> TT
Pgp2 ^{K307A} (F)	CAGTTAGAGGCGAT <u>G</u> CAATTATACGTTAAG
Pgp2 ^{K307A} (R)	CTTAACGTATAAA <u>A</u> TT <u>G</u> CATGCCTCTAAACTG
Ape1 ⁴¹⁻³⁹² (F)	GC <u>G</u> <u>C</u> <u>G</u> <u>G</u> <u>C</u> <u>T</u> CTGCTTAA <u>C</u> AAAGTTATGTATCAA AAAAGATC
Ape1 ⁴¹⁻³⁹² (R)	CAATGAGCTCCTAA <u>A</u> TTTTATAGTA <u>A</u> CTAATAATT <u>C</u> <u>T</u> <u>A</u> <u>G</u> <u>G</u> <u>C</u> <u>G</u> <u>C</u> <u>G</u>
Ape1 K103A	CTATCCTTACAGCCT <u>G</u> CATATCAACAA <u>A</u> TC ^b
Ape1 Y104G	CCTTACAGCCTAA <u>G</u> GTCAACAA <u>A</u> ATCTTAATC ^b
Ape1 Q105A	CTTACAGCCTAA <u>A</u> AT <u>G</u> CACAA <u>A</u> ATCTTAATCTG ^b
Ape1 Q106A	CAGCCTAA <u>A</u> AT <u>T</u> CA <u>G</u> CA <u>A</u> ATCTTAATCTGTT ^b
Ape1 N121A	CTTTGAA <u>A</u> TTTA <u>G</u> CCTCAAGAA <u>A</u> TCCTGC ^b
Ape1 S122A	CTTTGAA <u>A</u> TTTA <u>A</u> <u>G</u> CA <u>A</u> AGAA <u>A</u> TCCTGCTAATGC ^b
Ape1 R123A	GAAATT <u>T</u> AA <u>C</u> TA <u>G</u> CA <u>A</u> ATCCTGCTAATG ^b
Ape1 F132A	GCTGGACATA <u>A</u> TC <u>G</u> CC <u>A</u> CTAGGTGGG ^b

^aRestriction enzyme digestion sites are in underlined italics. The three nucleotides of the variant residue are in bold. The nucleotide that is different to the native sequence is underlined.

^bPrimers contain 5' phosphate.

Table 2-3. List of plasmids used in this study

Plasmid name	Description	Reference
pRRC-Pgp2	A complementation plasmid for chromosomal insertion of <i>pgp2</i> into one of three conserved <i>C. jejuni</i> rRNA sites; delivers a chloramphenicol resistance cassette for insertion selection	(49)
pRRC-H157A	A complementation plasmid carries H157A variant of Pgp2	Chapter 3
pRRC-C174S	A complementation plasmid carries C174S variant of Pgp2	Chapter 3
pRRC-Y233A	A complementation plasmid carries Y233A variant of Pgp2	Chapter 3
pRRC-F242A	A complementation plasmid carries F242A variant of Pgp2	Chapter 3
pRRC-K257A	A complementation plasmid carries K257A variant of Pgp2	Chapter 3
pRRC-K307A	A complementation plasmid carries K307A variant of Pgp2	Chapter 3
pRRC-E324Q	A complementation plasmid carries E324Q variant of Pgp2	Chapter 3
pET15b	<i>E. coli</i> protein expression vector containing a T7 promoter and an N-terminal His ₆ -tag coding sequence; contains an ampicillin resistance gene	Novagen
pET15b-Pgp2 ⁴³⁻³²⁵	pET15b construct for the expression of recombinant Pgp2	Chapter 3
pET15b-Pgp2 ^{K307A}	pET15b construct for the expression of recombinant Pgp2 K307A variant	Chapter 3
pET15b-Csd6	pET15b construct for the expression of recombinant Csd6	(127)
pET28a	<i>E. coli</i> protein expression vector containing a T7 promoter and an N-terminal His ₆ -tag coding sequence; contains a kanamycin resistance gene	Novagen
pET28a-Ape1 ²²⁻³⁹²	pET28a construct for the expression of recombinant Ape1 containing residues 22–392 in the native sequence	(54)
pET28a-Ape1 ⁴¹⁻³⁹²	pET28a construct for the expression of recombinant Ape1 containing residues 41–392 in the native sequence	Chapter 4
pET28a-Ape1 ^{K103A}	pET28a construct for the expression of recombinant Ape1 K103A variant	Chapter 4
pET28a-Ape1 ^{Y104G}	pET28a construct for the expression of recombinant Ape1 Y104G variant	Chapter 4

pET28a-Ape1 ^{Q105A}	pET28a construct for the expression of recombinant Ape1 Q105A variant	Chapter 4
pET28a-Ape1 ^{Q106A}	pET28a construct for the expression of recombinant Ape1 Q106A variant	Chapter 4
pET28a-Ape1 ^{N121A}	pET28a construct for the expression of recombinant Ape1 N121A variant	Chapter 4
pET28a-Ape1 ^{S122A}	pET28a construct for the expression of recombinant Ape1 S122A variant	Chapter 4
pET28a-Ape1 ^{R123A}	pET28a construct for the expression of recombinant Ape1 R123A variant	Chapter 4
pET28a-Ape1 ^{F132A}	pET28a construct for the expression of recombinant Ape1 F132A variant	Chapter 4

2.3 Protein expression vectors construction

2.3.1 Pgp2 and Pgp2 site-directed mutagenesis

A region of the *pgp2* (*CJJ81176_0915*) coding sequence corresponding to the product without the N-terminal signal peptide (residue 1-18) and the following 24 residues was cloned into a pET15b vector using *NdeI* and *XhoI* restriction sites, producing pET15b-Pgp2⁴³⁻³²⁵. The resulting recombinant Pgp2 protein includes an N-terminal His₆-tag followed by a thrombin cleavage site and residues 43-325. The Pgp2^{K307A} expression plasmid was made by site-directed mutagenesis using pET15b-Pgp2⁴³⁻³²⁵ as the template.

2.3.2 Ape1 and Ape1 site-directed mutagenesis

The expression vector pET28a-Ape1²²⁻³⁹² was donated by Dr. Erin Gaynor (54). The encoded product includes an N-terminal poly-His tag followed by a thrombin cleavage site and the full-length Ape1 protein without the N-terminal signal peptide (residue 1-21). The expression vector pET28a-Ape1⁴¹⁻³⁹² encoding Ape1 protein with an N-terminal His₆-tag followed by a thrombin cleavage site and residues 41–392 was constructed using the restriction enzyme double-digestion method. The portion of *ape1* (*CJJ81176_0638*) corresponding to the

product without the N-terminal signal peptide and the subsequent 19 residues was amplified from *C. jejuni* 81-176 genomic DNA using primers Ape1⁴¹⁻³⁹² (F) and Ape1⁴¹⁻³⁹² (R). The PCR product and pET28a vector were digested with restriction enzymes *NheI/BamHI*, and ligated together by T4 DNA ligase (NEB). The recombinant plasmid was then transformed into *E. coli* DH5α, selected using kanamycin, and validated by PCR analysis and sequencing.

Site-directed mutagenesis was used to generate the CBM35 loop variants K103A, Y104G, Q105A, Q106A, N121A, S122A, R123A, F132A using pET28a-Ape1²²⁻³⁹² as a template. Each primer was 5' phosphorylated and designed to contain a complementary mutation of the target sequence. Whole-plasmid amplification reactions were performed using Phusion polymerase (NEB) and Ampligase (Epicentre). Reactions were digested with DpnI for 3 hours at 37 °C to remove methylated template vectors.

2.4 Recombinant protein expression and purification

2.4.1 Pgp2

Recombinant Pgp2 was produced in *E. coli*. *E. coli* BL21(DE3) cells carrying the recombinant Pgp2 expression plasmid (pET15b-Pgp2⁴³⁻³²⁵) were cultured at 37 °C in 1 L LB supplemented with ampicillin (100 µg/mL) with shaking to an optical density of 0.6–0.8 before addition of 0.25 mM isopropyl β-D-thiogalactopyranoside (IPTG) to induce expression for an additional 16 hours at 25 °C. Cultures were pelleted by centrifugation and stored at –80 °C. Cells were thawed in binding buffer 50 mM Tris-HCl pH 7.0, 150 mM NaCl, 1 mM dithiothreitol (DTT) supplemented with 1 mM phenylmethylsulfonyl fluoride (PMSF) and DNase, and then lysed at 4 °C with a homogenizer. The lysate was centrifuged, loaded onto a 5 mL HisTrap HP column (GE Healthcare), and washed with 15 column volumes of 20 mM

imidazole in binding buffer. Pgp2 was then eluted with increasing imidazole in binding buffer. The protein was digested with thrombin (250:1 w/w Pgp2: thrombin ratio) overnight at 4 °C to remove the His₆-tag. Thrombin was removed with *p*-aminobenzamidine agarose beads (5 mg thrombin: 1 mL beads). Pgp2 protein was reloaded onto a 5 mL HisTrap HP column to remove uncleaved protein. The protein without the His₆-tag was further purified by gel filtration chromatography on a Superdex 200 16/60 column (GE Healthcare) in binding buffer. Protein fractions were pooled and concentrated to 150–200 μM and flash-frozen in liquid nitrogen. Protein purity was assessed by SDS-PAGE. Pgp2^{K307A} protein was purified as described for recombinant Pgp2.

2.4.2 Pgp2 labeled with ¹⁵N, ¹³C, ²H

¹⁵N-labeled Pgp2 was produced in modified M9 minimal media (6 g/L Na₂HPO₄, 3 g/L KH₂PO₄, 0.5 g/L NaCl, 1 g/L ¹⁵NH₄Cl, 10 g/L D-glucose, 1 mM MgSO₄, 10 mg/L vitamin B1, 10 μM FeCl₃, 0.1 mM CaCl₂, 100 μg/mL ampicillin). Briefly, overnight LB broth cultures were collected by centrifugation and resuspended in M9 media. Cell suspensions were standardized to OD₆₀₀ 0.05 in M9 media and grown at 37 °C to achieve log phase (OD₆₀₀ ~0.7–1.0). Protein expression was induced for 16 hours at 22 °C with 0.3 mM IPTG. The purification protocol was adapted from that for unlabeled Pgp2. The final buffer contained 50 mM Tris-HCl pH 6.5, 150 mM NaCl and 1 mM DTT. This was the buffer for all NMR experiments in this study.

Pgp2 labeled with ²H, ¹³C, and ¹⁵N was expressed in M9 minimal media with deuterium oxide (D₂O) and D-glucose-¹³C₆-d₇ (3 g/L). Protonated reagents were dissolved in D₂O and lyophilized prior to use. To optimize expression, cells were first adapted to deuterium M9 media (170), inoculated in M9/D₂O media at OD₆₀₀ 0.05, and cultured at 37 °C to OD₆₀₀ 1.0.

Protein expression was induced with 1 mM IPTG for 16 hours at 25 °C. Cells were lysed in denaturing buffer (4 M guanidinium HCl, 20 mM Na₂HPO₄, pH 7.0, 0.5 M NaCl, 2 mM Tris(2-carboxyethyl)phosphine (TCEP), and 5% glycerol) supplemented with 1 mM PMSF and DNase using a homogenizer. The denatured protein underwent uniform amide deuterium to protium exchange, as required for ¹H-detected NMR measurements. The cleared supernatant was loaded onto a HisTrap HP column (GE Healthcare). After binding, the column was washed with denaturing buffer followed by on-column refolding with gradually decreasing concentrations of guanidinium HCl to 0 M. Folded protein was eluted with elution buffer (20 mM Na₂HPO₄, pH 7.0, 0.5 M NaCl, 0.5 M imidazole, 2 mM TCEP, and 5% glycerol). The His₆-tag was cleaved by thrombin (100:1 w/w Pgp2: thrombin ratio) during dialysis (50 mM Tris pH 7.0, 150 mM NaCl and 1 mM DTT). Thrombin was removed with p-aminobenzamidine agarose beads (5 mg thrombin: 1 mL beads). Uncleaved proteins and cleaved His₆-tag were removed using a HisTrap HP column. His₆-tag free Pgp2 was polished using a Superdex 200 16/60 column (GE Healthcare) in NMR experiment buffer. The sample was immediately concentrated to ~350 μM and was used for NMR data collection.

2.4.3 Csd6

A Csd6 expression plasmid, pET15b-Csd6, was a gift from Dr. Nina R. Salama (127). The *csd6* gene coding for amino acids 18–330 (without the predicted signal peptide) was cloned from *H. pylori* strain G27 into pET15b. Csd6 purification was as for Pgp2 except that the binding buffer was adjusted to pH 7.5.

2.4.4 Ape1

Ape1²²⁻³⁹², Ape1⁴¹⁻³⁹² and variants were prepared in *E. coli* BL21(DE3) grown overnight at 37 °C in LB media containing 25 µg/ml kanamycin. Overnight cultures were inoculated into 1 L LB media at a 1:100 dilution and grown at 37 °C to OD₆₀₀ of 0.8-1.0 before induction with 0.5 mM IPTG at 20 °C for 16 hours. The cells were pelleted by centrifugation at 5,000 rpm at 4 °C for 15 min. The cell pellet was resuspended at 4 °C in 50 mM Tris-HCl pH 7.0, 500 mM NaCl, 20 mM Imidazole, 1 mM PMSF, and DNase and lysed using an Emulsi Flex-C5 homogenizer (Avestin). The cell lysate was centrifuged at 16,000 rpm at 4 °C for 50 min, then the soluble fraction was filtered through 0.22 µm PVDF membrane filter before loading onto a 5 mL HisTrap HP column (GE Healthcare). The column was washed with 20 column volumes of 50 mM Tris-HCl pH 7.0, 500 mM NaCl, and Ape1 was eluted with imidazole. Ape1 was dialyzed against 20 mM Tris-HCl pH 7.0, 150 mM NaCl and simultaneously digested with thrombin (200:1 w/w Ape1: thrombin ratio) at 4 °C overnight to remove the His₆-tag. The Ape1-thrombin mixture was incubated with p-aminobenzamidine-agarose beads (5 mg thrombin:1 mL beads ratio; Sigma) at 4 °C for 15 min to remove thrombin and was then filtered through a 0.22 µm PVDF membrane filter. The cleaved protein was separated using a second HisTrap HP column (GE Healthcare). His₆-tag free Ape1 protein was then loaded onto a Superdex 200 16/60 column (GE Healthcare) in 20 mM Tris-HCl pH 7.0, 150 mM NaCl. Finally, monodisperse tag-free Ape1 was concentrated using 10 kDa MWCO Amicon (Millipore) to 15–20 mg/ml, flash frozen in liquid nitrogen, and stored in –80 °C. Protein purity was assessed by SDS-PAGE and electrospray ionization mass spectroscopy (MSL/LMB Proteomics Core Facility, UBC).

Seleno-methionine (SeMet) labeled Ape1⁴¹⁻³⁹² was prepared in *E. coli* BL21(DE3) grown overnight at 37 °C in LB media containing 25 µg/ml kanamycin. Pelleted cultures were then inoculated in 1 L M9 minimal media (6 g Na₂HPO₄, 3 g KH₂PO₄, 1 g NH₄Cl, 0.5 g NaCl, 1 mM MgSO₄, 40% (w/v) glucose, 0.5% (w/v) thiamine, 4.2 g Fe₂SO₄, 25 µg/mL kanamycin per liter) and grown at 37°C to an OD₆₀₀ of 0.3. 100 mg of L-lysine, L-threonine, L-phenylalanine and 50 mg of L-isoleucine, L-leucine, L-valine, and L-seleno-methionine were then supplemented into the 1 L culture media, followed by induction with 0.5 mM IPTG at 20 °C for 16 hours. SeMet-labeled Ape1 was purified using the same protocol as for unlabeled proteins.

2.5 Crystallization and Structure determination

2.5.1 Pgp2 and K307A variant

Unlabeled recombinant Pgp2 (10 mg/mL) was prepared in a buffer of 50 mM Tris pH 7.0, 150 mM NaCl and 1 mM DTT. Pgp2 crystals grew at room temperature using the hanging drop vapor diffusion method. The reservoir contained 200 mM tris-methylamine N-oxide dihydrate, 100 mM Tris pH 8.5 and 20% (w/v) PEG monomethyl ether 2000. Rectangular shaped crystals grew to size of 0.2–0.4 µm within a week. Reservoir solution supplemented with 25% glycerol was used as a cryoprotectant. X-ray diffraction data was collected on beamline 9-2 at the Stanford Synchrotron Radiation Lightsource (SSRL; Palo Alto, CA). Each data set was collected from a single crystal at 100 K using a wavelength of 0.98 Å. Diffraction images were processed using HKL2000 (171). The Pgp2 structure was phased by molecular replacement method using Csd6 (PDB ID: 4XZZ) as the search model with Phenix.phaser (172). The structure was refined with Phenix.refine and manual model building was done with

Coot (173). The final model includes residues Ser-His-Met from the expression vector and the residues of the Pgp2 construct (residues 43 to 325). Due to weak electron density, the side chains of residues R121, K268, Y296, Y297, Q302 and F303 were not included in the model.

Pgp2^{K307A} (14 mg/mL) was prepared in 50 mM Tris pH 7.0, 500 mM NaCl and 10% glycerol. The reservoir contained 0.17 M ammonium acetate, 0.085 M sodium acetate pH 4.6, 25.5% (w/v) PEG 4000 and 15% (v/v) glycerol. Pgp2^{K307A} crystals grew at 4 °C by hanging drop vapor diffusion and were cryoprotected with 20% glycerol. X-ray diffraction data were collected from a single crystal at 100 K using a wavelength of 0.98 Å at the Canadian Light Source on beamline 08B1-1. Diffraction images were processed using XDS (174) and CCP4 packages (175), phased using the Pgp2 structure and refined as above. Data collection and refinement statistics for Pgp2 and Pgp2^{K307A} are summarized in **Table 3-1**. The coordinates are deposited as entries 6XJ6 and 6XJ7 in the Protein Data Bank.

2.5.2 Ape1

Ape1⁴¹⁻³⁹² was crystallized by hanging drop vapor diffusion. The crystallization well contained a 900 µl solution of 100 mM CAPS pH 10.5, 200 mM NaCl, 16% (w/v) PEG8000, 2.5% (w/v) PEG3350. 1 µL of this solution was mixed with 1 µL Ape1⁴¹⁻³⁹² (12 mg/ml). A rod-shaped crystal with a size of 0.2 µm appeared after one day of incubation at room temperature. The crystal was submerged in 35% (w/v) PEG8000 prepared in the crystallization solution as a cryoprotectant, then immediately stored in liquid nitrogen before data collection. A native dataset was collected at 1 Å at 100 K on beamline 9-2 at SSRL. SeMet Ape1⁴¹⁻³⁹² was crystallized as described for unlabeled Ape1⁴¹⁻³⁹² with modification. The crystallization well contained 100 mM CAPS pH 10.5, 200 mM NaCl, 16% (w/v) PEG 8000, 12 mM phenol. A 0.4 mm rod-shaped crystal was submersed in cryoprotectant consisting of 35% (w/v) PEG

8000 and 10% (v/v) glycerol prior to freezing. A single-wavelength anomalous dispersion (SAD) dataset was collected at 0.979 Å.

The collected datasets were indexed, integrated, and scaled with HKL2000 (176). Structural determination was conducted using software packages in Phenix (172). SeMet Ape1⁴¹⁻³⁹² SAD dataset was processed in Phenix.AutoSol to obtain initial phases and a preliminary model through automated fitting. Manual model construction of SeMet Ape1 was done with Coot (173) and Phenix.refine. The Ape1⁴¹⁻³⁹² native dataset was phased by molecular replacement using SeMetApe1, and the model was built as described above. The side chains of K49, Q63, K224, K316 of chain A to C; K177, K313, Q314 and K319 of chain A; K147 and K313 of chain B; K50, K53, E56, K168, K275, K298, Q361 and D391 of chain C were not included due to disorder.

Ape1²²⁻³⁹² was crystallized using hanging drop vapor diffusion. The crystallization well contained 900 µl of 166 mM sodium acetate, 28% (w/v) PEG4000, and 80 mM Tris-HCl pH 8.5. 1 µl precipitant solution and 1 µl Ape1²²⁻³⁹² (28 mg/mL) were mixed with 0.2 µl of 10 mM GSH (L-Glutathione reduced) and 10 mM GSSG (L-Glutathione oxidized) in the hanging drop. Crystals grew at room temperature within a week. The crystal was briefly soaked in crystallization solution containing 15% (v/v) glycerol before stored in liquid nitrogen. A native dataset was collected at 0.98 Å at 100 K at the Canadian Light Source on beamline 08ID-1. Data process, phasing and model building are same the Ape1⁴¹⁻³⁹² model determination methods. Side chains of K329 of chain B and D28 of chain A to C were not included in the final model due to disorder.

2.6 Microscopy and Celltool shape analysis

Overnight broth cultures of *C. jejuni* were standardized to OD₆₀₀ 0.05 in fresh MH-TV media and grown for 4 hours at 38 °C under microaerophilic conditions (Oxoid CampyGen) to log phase (OD₆₀₀ 0.1–0.3). Cells were mounted on a 1% agarose gel pad on a glass slide and imaged with a Nikon Eclipse TE2000-U microscope equipped with 100X oil-immersion objective and a Hamamatsu C4742-95 digital camera. Cell images were transformed into binary mode with GIMP software and analyzed with the Celltool software package (177). Principal component analysis on wild-type cell contours of ~400 cells from each strain generated a shape mode that described cell curvature from straight to highly curved morphology. To compare the curvature distributions of each strain to the distribution of wild-type cells, all cells were aligned with the averaged morphology of wild-type cell by iterative translation and rotation.

2.7 Immunoblotting

C. jejuni whole cell lysates of each strain were prepared from log phase cultures (OD₆₀₀ 0.1–0.3) that were centrifuged and frozen. The cell pellet was lysed in 100 µl of 0.1% Triton X-100, 50 mM Tris pH 8.0, 10% glycerol and 150 mM NaCl at room temperature for 30 min. Total protein from each lysate was by normalized to OD₅₉₅ 0.44/µl using Bradford reagent (Bio-Rad). Sample were separated on a 12% SDS-PAGE and transferred onto a nitrocellulose membrane. Membranes were blocked by TBS-T buffer plus 5% skim milk (TBS-T; 20 mM Tris pH 7.5, 150 mM NaCl and 0.5% Tween 20) at 4 °C for overnight. The membrane was incubated with 1:3500 dilution of an anti-Pgp2 antibody, produced from a rabbit immunized with recombinant Pgp2, at 4 °C overnight followed by three washes with TBS-T buffer. Secondary antibody Alexa Fluor 680 (Invitrogen) was added at 1:2000 dilution and incubated

for 1 hour at room temperature. The membrane was washed three times with TBS-T buffer before imaged at 700 nm by Odyssey Classic Imaging System (LI-COR).

2.8 Peptidoglycan isolation

C. jejuni was cultured on 100 MH-T plates for 18 hours at 38 °C and at late log phase cells were collected in cold MH-TV broth (1 mL/plate) by scraping. Culture media was removed by centrifugation at 5,000 rpm at 4 °C for 10 min and the cell pellet was re-suspended in 80 mL cold PBS buffer. Cells were lysed by mixing with an equal volume of boiling 6% SDS for 4 hours and centrifuged at room temperature to remove intact cells. The PG was pelleted from the cell lysate by ultracentrifugation at 45,000 rpm at 22 °C for 3 hours and washed with water. To remove glycogen and lipoproteins, the PG was resuspended in buffer (10 mM Tris pH 7.0 and 10 mM NaCl) and digested sequentially with alpha-amylase (200 µg/mL) and Pronases (200 µg/mL) at 37 °C overnight. The PG sample was boiled in 6% SDS for 10 min followed by centrifugation (10,000 rpm, room temperature, 10 min). SDS was removed by 3 washes with water and ultracentrifugation (45,000 rpm at 22 °C for 3 hours). PG samples were lyophilized in water and stored at -20 °C.

2.9 Muropeptide preparation and HPLC analysis

To prepare muropeptides, 0.2 mg PG was digested with 50 U mutanolysin (Sigma) in 50 mM Tris pH 7.0 and 150 mM NaCl at 37 °C for 24 hours. Mutanolysin was removed by boiling for 10 min and centrifugation. Muropeptides prepared for HPLC analysis were reduced with 100 mM sodium borohydride pH 9.0 at room temperature for 30 min, titrated to pH ~4 with phosphoric acid, and passed through a 0.22 µm filter. Muropeptide separation by HPLC was performed with an Xterra MS C18 column (Waters) and UV detection at 210 nm. Elution

relied on a gradient from 100% buffer A (50 mM sodium phosphate pH 4.3) to 100% buffer B (50 mM sodium phosphate pH 4.9 and 15% (v/v) methanol) over 100 minutes.

2.10 NMR

2.10.1 NMR spectra assignment

NMR spectra for resonance assignments of Pgp2 were recorded at 25 °C using an ~ 350 μM uniformly labeled ²H-¹³C-¹⁵N Pgp2 sample with 5% D₂O included for locking. Spectra were acquired on Bruker Avance III 500, 600, and 850 MHz spectrometers equipped with xyz-gradient TCI cryoprobes. Collected spectra include a ¹⁵N-BEST-TROSY-HSQC, a BEST-TROSY-HNCACB/BEST-TROSY-HNCOCACB pair, and a BEST-TROSY-HNCACO/BEST-TROSY-HNCO pair (178). Data were processed with NMRpipe (179) and analyzed in NMRFAM-SPARKY (180) and Topspin. Spectra were automatically interpreted using PINE (181) and verified manually to assign main chain ¹H, ¹³C, and ¹⁵N signals.

2.10.2 NMR titration experiment

NMR titration experiments were performed with ¹⁵N-labeled Pgp2. PG ligand titration studies with ¹⁵N-labeled Pgp2 were monitored by ¹⁵N-BEST-TROSY-HSQC at 25 °C for different ligand-to-protein ratios. PG ligand was dialyzed against water using a float dialysis membrane device with a 100–500 Da cut-off (Spectrum Laboratories, Inc) and lyophilized before preparation of a concentrated stock solution in NMR buffer (182). A 160 μM sample of ¹⁵N-labeled Pgp2 was titrated with 3.4 and 6.8 μL of D-Glu-*m*-oxa-Dap-D-Ala (4 μg/μL; MW 434.2 g/mol), giving a final peptide:protein molar ratio of 2:1. A 160 μM sample of ¹⁵N-labeled Pgp2 was titrated with 5, 10 and 20 μL of purified murotetrapeptide (50 μg/μL; MW

941.1 g/mol) to a final peptide:protein molar ratio of 33:1. A 160 μ M sample of ^{15}N -labeled Pgp2 was titrated with 5, 10 and 20 μ L of purified cross-linked murotetrapeptides (50 μ g/ μ L; MW 1864.8 g/mol) to a final peptide:protein molar ratio of 16:1. A 160 μ M sample of ^{15}N -labeled Pgp2 was titrated with 5, 10, and 20 μ L of muramidase-digested $\Delta\text{pgp}2$ PG solution (60 μ g/ μ L) to a final concentration of 5.5 μ g/ μ L. A 110 μ M sample of ^{15}N -labeled Pgp2 was titrated with 60 μ L of Tse1-digested *E. coli* PG (~30 μ g/ μ L) to a final concentration of ~4 μ g/ μ L. Spectra were overlaid in NMRFAM-SPARKY, and CSP ($\Delta\delta$) values were calculated as $\Delta\delta = \sqrt{(\Delta\delta_{\text{H}})^2 + (0.14 * \Delta\delta_{\text{N}})^2}$, where $\Delta\delta_{\text{H}}$ and $\Delta\delta_{\text{N}}$ denote the observed changes of the amide $^1\text{H}^{\text{N}}$ and ^{15}N chemical shifts in the absence versus presence of PG ligand at the final highest concentration used for a titration series.

2.11 Peptidoglycan pull-down

Pgp2 and variant proteins pulled-down by PG isolated from *C. jejuni* $\Delta\text{pgp}2$. Pgp2 proteins at the indicated amounts were incubated with purified PG (50 μ g) in a 250 μ L reaction at 4 °C for 30 min, followed by centrifugation at 13,000 rpm for 10 min. Insoluble PG and pulled-down proteins were washed 3 times with 1 mL of buffer (50 mM Tris pH 7.0 and 150 mM NaCl) to remove unbound proteins. Insoluble PG and pulled-down proteins were analyzed by SDS-PAGE stained with Coomassie Blue.

Ape1 and variant proteins (40 μ g) were incubated with purified *C. jejuni* $\Delta\text{ape}1$ PG (50 μ g) in 250 μ L of reaction buffer (50 mM sodium phosphate pH 6.5, 50 mM NaCl) at 4 °C for 20 min, followed by centrifugation at 13,000 rpm for 10 min. To remove unbound proteins, insoluble PG and pulled-down proteins were washed three times with 1 mL of buffer. Pulled-down proteins were analyzed by SDS-PAGE. Band intensities were quantified in ImageJ.

2.12 O-acetylesterase activity on 4-Nitrophenyl acetate

O-acetylesterase activity was quantified using a colorimetric assay. 20 nM Apel protein and 2 mM *p*NPAc (prepared in methanol and diluted with reaction buffer to a final concentration of < 1%) were incubated in a 300 μ l volume of 50 mM sodium phosphate pH 6.5 and 50 mM NaCl at 25 °C for 5 min. 1 unit of specific activity was defined as the amounts of released *p*-nitrophenol (μ mole) per min per mg of protein. A molar extinction coefficient of 18,000 M⁻¹cm⁻¹ for *p*-nitrophenol at 405 nm was used to calculate product formation (183).

2.13 HADDOCK docking

2.13.1 Pgp2-PG

Models of Pgp2 in complex with murotetrapeptides were produced in HADDOCK 2.2 (184). Two starting conformers for Pgp2, based on the wild-type and Pgp2^{K307A} crystal structures, were generated as they differed in the NTF2 loop region that overhangs the pocket entrance. Unmodeled side-chains were manually rebuilt and residue 307 was restored to Lys in Pgp2^{K307A} using Coot (173) prior to docking. The sugar moiety coordinates and topology files of GlcNAc-GlcNAc with a β -(1-4)-glycosidic bond of a phi/psi angles of 69°/12° (185) was produced with the GlyC_aNS server (186). Tetrapeptide coordinates and topology files were generated with the PRODRG server (187) using a tetrapeptide model extracted from PDB entry 2MTZ. An ensemble of 20 murotetrapeptide conformers were generated by simulated annealing and energy minimization (188).

AIRs are defined as either active residues involved in binding or passive residues potentially involved (**Table 3-2**). The active residues of Pgp2 were defined as solvent accessible residues with a CSP above a cut-off in the murotetrapeptide titration experiment

and from the list of functional residues identified by mutagenesis. The passive residues of Pgp2 were defined as the proximal residues within 5 Å of the active residues. The active residues of the murotetrapeptide were the peptide moiety and the passive residues were the sugars.

For the docking experiment using data from a titration with purified murotetrapeptide, an unambiguous distance restraint (2.0 Å) was defined between the sulfur of the nucleophile Cys174 and the carbonyl carbon of *m*-DAP. A sample of 10,000 docking solutions were generated at the rigid body stage. The top 400 complexes based on HADDOCK score were used subjected to simulated annealing and the resulting top 200 complexes were further refined with waters. The docking solutions formed 5 clusters using an FCC cut-off of 0.45. In a second docking experiment, the active residues of Pgp2 were defined from residues with CSP above the cut-off in the muramidase digested $\Delta pgp2$ PG titration experiment. Both the peptide and sugar moieties of the murotetrapeptide were defined as passive residues. The final 200 solutions were grouped into 5 clusters using the FCC cut-off of 0.4.

2.13.2 Ape1-PG

A model of the CjApe1-PG complex was produced using HADDOCK 2.2 (184,189). The Ape1 docking conformer was extracted from the crystal structure of the acetate-bound CjApe1⁴¹⁻³⁹², with missing side-chains rebuilt using Coot (173). The binding interface of Ape1 was predicated using the CPoRT server (190). CPoRT predicts the consensus binding interface from the results of 6 prediction servers. An output of active (i.e., involved in binding) and passive residues (~5 Å proximal to the binding site) were produced from CPoRT.

An ensemble of 10 *O*-acetyl hexasaccharide conformers were used to represent the PG glycan. The phi/psi angles of the β -(1-4)-glycosidic bond in the hexasaccharide was modelled at 69°/12°, as was previously determined by NMR (186). An *O*-acetyl group was manually

built onto the third sugar residue of the hexasaccharide using CNS (188). The ensemble of *O*-acetyl hexasaccharide conformers were generated by simulated annealing and energy minimization in CNS. All residues in *O*-acetyl hexasaccharide were defined as passive and are fully flexible in HADDOCK.

The list of AIR is summarized in **Table 4-4**. A total of 6 unambiguous distance restraints were used in docking. Two involved the triad hydrogen bond distance: 2.5–3.5 Å between O δ 2 of the acid D367 and N δ 1 of the base H369, and 3.5 Å between N ε 2 of the base H369 and O γ of the nucleophile S73. The remaining four involved the bond distance between the catalytic cleft and the *O*-acetyl group of the substrate, including 2.5–3.5 Å between the O γ of S73 and carbonyl carbon of *O*-acetate, 2.5 Å between the *O*-acetate oxygen atom to the amide nitrogen of G237 and N δ 2 of N270 from the oxyanion hole, and 4.0 Å of hydrophobic contact between the methyl group carbon of *O*-acetate and C γ of V368. In the docking procedure, a sample of 10,000 docking solutions were generated at the rigid body stage. The top 400 complexes based on HADDOCK scoring were subjected to simulated annealing and the resulting top 200 complexes were further refined with waters.

CHAPTER 3: PG recognition of Pgp2 determines *C. jejuni* helical shape

3.1 Introduction

Helical cell shape is maintained by PG trimmed by the LD-carboxypeptidase Pgp2, an enzyme that cleaves D-Ala from both monomeric and cross-linked tetrapeptides (49). Deletion of *pgp2* displayed a straight-rod morphology and no PG tripeptides were detected (49). Sequence analysis predicts Pgp2 contains an LD-carboxypeptidase (LD-CPase) and a conserved NTF2-like superfamily fold (NTF2), but little is known about the function of NTF2 domain in Pgp2. Here, we report the crystal structure of Pgp2 and identified a conserved binding pocket in the NTF2 domain. We investigated the role of the NTF2 domain in maintaining *C. jejuni* helical shape. Site-directed mutagenesis combined with interaction studies using PG fragments were used to show that the NTF2 domain binds PG and is required for *C. jejuni* helical shape. On the basis of these results, we propose a model for Pgp2-PG interaction involving both the LD-CPase and the NTF2 domains to guide catalytic activity.

3.2 Results

3.2.1 Two clusters of conserved residues are identified in the Pgp2 structure

A recombinant Pgp2 construct (Pgp2⁴³⁻³²⁵) containing residues 43–325 of the native sequence (*CJJ81176_0915*) is enzymatically active (191) and was suitable for structural characterization. Pgp2 crystallized in space group *P*2₁2₁2₁ and the structure was solved to 1.6 Å resolution by molecular replacement using Csd6 as a search model (PDB ID: 4XZZ). X-ray data collection and refinement statistics are summarized in **Table 3-1**. The Pgp2 structure contains one Pgp2 molecule in the asymmetric unit (**Figure 3-1**). Analysis in solution by

dynamic light scattering indicated an average molecular weight of 44 kDa, consistent with the predicted weight of the recombinant Pgp2 monomer (36 kDa; not shown).

Table 3-1. Data collection and refinement statistics for Pgp2 and Pgp2^{K307A}

	Pgp2 ⁴³⁻³²⁵	Pgp2 ^{K307A}
Data collection ^a		
Space group	P2 ₁ 2 ₁ 2 ₁	P22 ₁ 2 ₁
Cell dimensions		
<i>a, b, c</i> (Å)	47.5, 71.9, 91.7	64.9, 89.8, 106.6
α, β, γ (°)	90, 90, 90	90, 90, 90
Total reflections	320747	396576
No. of unique reflections	51069	53923
Resolution (Å)	50.00-1.50 (1.53-1.50)	50.00-1.85 (1.89-1.85)
R _{merge}	0.037 (0.581)	0.102 (0.868)
<i>I</i> / σ <i>I</i>	33.5 (2.0)	13.1 (2.3)
CC (1/2)	0.978 (0.885)	0.998 (0.829)
Completeness (%)	99.5 (99.5)	100 (100)
Redundancy	6.3 (6.1)	7.4 (7.4)
Refinement		
Resolution (Å)	32.97-1.50	47.18-1.85
R _{work} /R _{free}	0.158/0.192	0.164/0.203
Ramachandran		
Favored (%)	98.2	99.1
Allowed (%)	1.8	0.9
Outliers (%)	0	0
Average B factors (Å ²)		
Protein	30.8	31.0
Water	38.5	35.6
RMSDs from ideal values		
Bond lengths (Å)	0.004	0.010
Bond angles (°)	0.709	0.964
PDB ID	6XJ6	6XJ7

^aValue for the highest resolution shell is shown in parenthesis.

The structure of Pgp2 contains an N-terminal helix (residues Q43-I51), the catalytic LD-CPase domain (residues V65-K201), and the C-terminal NTF2 domain (residues K208-Q325), each connected to the next domain by a single loop (**Figure 3-1A**). An extensive interface with a buried surface area of 1130 Å² is found between the LD-CPase and NTF2 domains, as calculated by the PISA server (192). The LD-CPase domain consists of parallel

strands β 5- β 6 sandwiched by a beta sheet (β 1- β 4 and β 7), four helices (α 2- α 5) and connecting loops. The likely catalytic triad (C174-H157-G158) is located on the central stands β 5- β 6 (**Figure 3-1A and Figure 3-1D**). The NTF2 domain contains three helices (α 6- α 8) wrapped around a curved antiparallel β -sheet (β 8- β 11), which together forms a cone shape domain with a broad pocket.

Using a Dali search (193) for similar structures in the PDB, only Csd6 can be superimposed with Pgp2 over both the LD-CPase and NTF2 domains (PDB ID: 4XZZ, RMSD of 1.8 Å for 281 C α atoms). The structure of Csd6 includes two additional α -helices at the N-terminus that forms a homodimerization domain between two Csd6 monomers. The equivalent 27 residues are absent in the truncated Pgp2 construct. The structure of Csd6 deviates from strands β 9- β 10 of the Pgp2 NTF2 domain (**Figure 3-1B**). The LD-CPase domain of Pgp2 is distantly related to LD-transpeptidases with sequence identity <20%. An example is LdtMt5 from *Mycobacterium tuberculosis* (PDB ID: 4Z7A, RMSD of 2.4 Å over 106 C α atoms). The NTF2 domain is structurally similar to proteins with diverse functions, such as calmodulin-dependent protein kinase II from *Rattus norvegicus* (PDB ID: 5U6Y, RMSD of 2.4 Å over 109 C α atoms) and penicillin binding protein 2A, a DD-transpeptidase from methicillin-resistant *Staphylococcus aureus* (PDB ID: 3ZFZ, RMSD of 2.7 Å over 95 C α atoms).

To predict functionally important residues in Pgp2, 150 homologous sequences with 35%-95% sequence identity to Pgp2 were identified and aligned in ConSurf (194). The level of sequence conservation was mapped onto the surface of Pgp2 (**Figure 3-1C**). Regions of high sequence conservation are observed on one side of the molecule, focused in two clusters. The first cluster is in proximity to the catalytic triad in the LD-CPase domain (**Figure 3-1D**).

The second cluster is formed by 17 primarily aromatic (41%) and charged (30%) residues that are clustered in the pocket of the NTF2 domain.

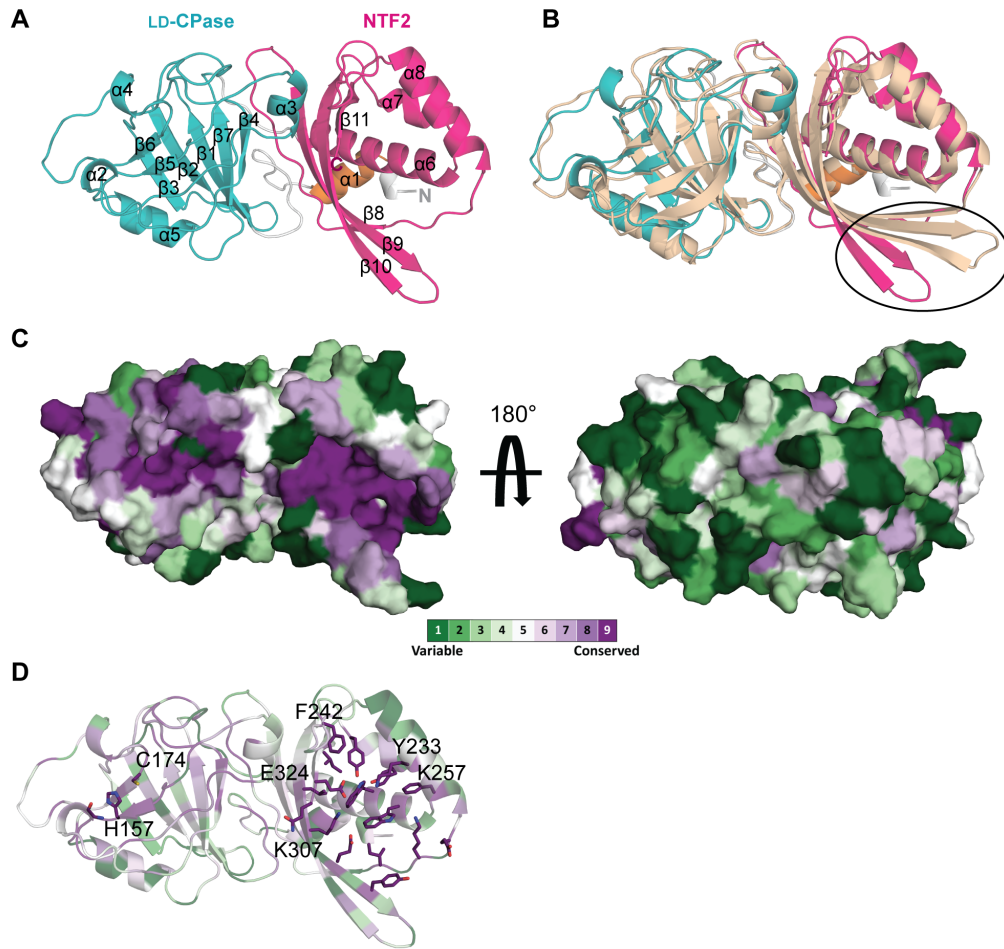


Figure 3-1. The conserved residues of Pgp2 are focused in two clusters: the active site of the LD-CPase domain and the pocket of NTF2 domain

(A) The overall monomeric structure of Pgp2. The N-terminal helix, LD-CPase and NTF2 domains, and loops between domains are colored orange, cyan, magenta and gray, respectively. (B) Superimposition of Pgp2 and *H. pylori* Csd6 (orange, PDB ID: 4XZZ). The strands $\beta 9-\beta 10$ of Pgp2 (circled) showed the largest deviation from the Csd6 model. (C) Surface representation of Pgp2 colored by amino acid conservation. The most conserved residues are shown in purple and the least conserved in green. (D) The clustered conserved residues are shown in stick form (nitrogen, blue; oxygen, red; sulfur, yellow). Residues targeted for subsequent site-directed mutagenesis studies are labeled.

3.2.2 The LD-CPase and NTF2 domains are required for helical shape

Previously, integration of wild-type *pgp2* with its native promotor at a remote site of the $\Delta pgp2$ chromosome restored helical cell shape in the straight-rod deletion strain (49). Using this complementation system, we evaluated the importance of the two conserved clusters by constructing single residue Pgp2 variants. Mutants of *pgp2* encoding substitutions of catalytic residues (H157 and C174) or residues in the NTF2 pocket (Y233, F242, K257, K307, and E324) were generated, and the morphologies of these strains were examined by differential interference contrast microscopy. The $\Delta pgp2$ strains complemented by mutants of the catalytic triad (H157A, C174S) displayed rod morphologies, confirming that Pgp2 catalytic activity is required for helical shape (**Figure 3-2A**). Point mutations within the NTF2 pocket resulted in bacteria with partially curved to straight morphologies. Quantitative analysis of each strain by Celltool (177) indicated that strains complementation with native *pgp2* displayed a cell curvature distribution similar to wild-type cells, whereas the strains expressing Pgp2 mutants had similar lengths but varied in cell curvature (**Figure 3-2B**). The catalytic triad mutants (C174S, H157A) and three mutants within the NTF2 pocket (Y233A, K257A and K307A) resulted in bacteria with cell curvature distributions that were similar to the $\Delta pgp2$ strain. Two mutants were of an intermediate phenotype (F242A and E324Q). These curvature defects were not due to Pgp2 expression deficiency as confirmed by Western blot using an anti-Pgp2 antibody (**Figure 3-2C**). Together, we concluded that the LD-CPase and NTF2 domains are both required for helical shape in *C. jejuni*.

Pgp2 was reported to be post-translationally modified (195). In this earlier study, Pgp2 purified from cell lysate using a carbohydrate binding column displayed three spots by 2-dimensional electrophoresis. Two *C. jejuni* N-linked glycosylation sequons (D/E-X1-N-X2-

S/T, where X1, X2≠Proline) were found in the sequence of Pgp2, suggesting post-translational glycosylation likely gave rise to the two bands observed on the Western blot (**Figure 3-2C**). No positive correlation was found from a quantification of the intensities of the two bands and a comparison against cell shape.

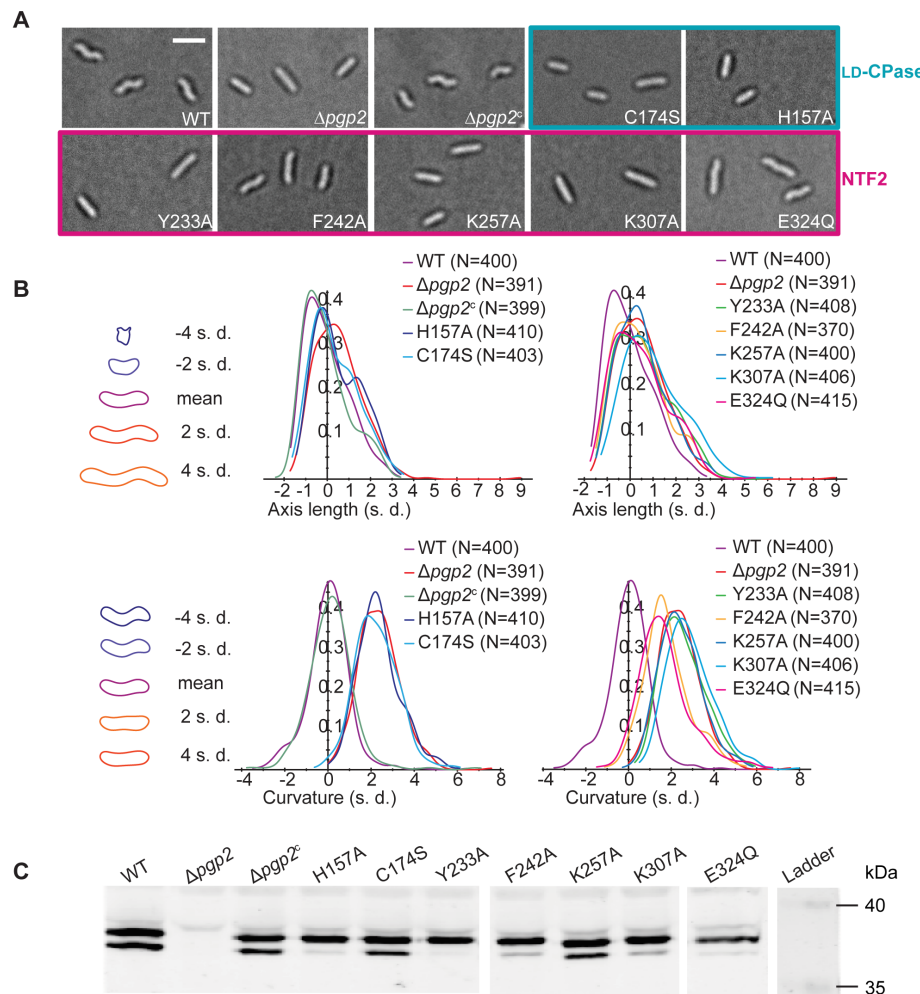


Figure 3-2. Helical shape restoration of $\Delta pgp2$ by complementation with wild-type $pgp2$ and point mutants of the catalytic triad and within the NTF2 pocket

(A) Light microscope images of *C. jejuni* strains. Scale bar = 2 μ m. (B) Quantitative analysis of the shape of individual cells extracted from images using Celltool software. The shape mode that best describes the shape variance in each analysis (axis length or curvature) is plotted on the left side. Smooth histograms display the population of cells by axis length or curvature (x-axis). (C) Composite western blot of *C. jejuni* whole cell extracts for Pgp2. Samples were normalized to total protein using a Bradford assay. Spliced lanes are separated by white lines.

3.2.3 The NTF2 domain is required for Pgp2 catalytic activity in *C. jejuni*

Pgp2 activity was quantified by assaying for the products (tripeptide or cross-linked tetra-tripeptides) in the hydrolysed PG of *C. jejuni*. Purified PG from *C. jejuni* strains complemented with *pgp2* harboring point mutations was digested by muramidase and analyzed by HPLC. The identities of peaks from the HPLC elution profile were confirmed by MALDI-TOF mass spectrometry. Complementation with a catalytically inactive variant (C174S) produced undetectable levels of monomeric and crosslinked tripeptides (**Figure 3-3, left panel**), and this variant served as a negative control. Lower levels of products were observed in the NTF2 domain mutant strains (K257A, K307A, and E324Q) relative to the strain expressing wild-type Pgp2 (**Figure 3-3, left panel**). The proportion of monomeric tripeptides ranged from 14% to 25% whereas the proportion of cross-linked tetra-tripeptides ranged from 41% to 95% (**Figure 3-3, right panel**), demonstrating that the NTF2 domain is required for full Pgp2 activity in *C. jejuni*. Furthermore, for NTF2 mutants, the activity on monomeric tetrapeptides was diminished more than for cross-linked tetrapeptides.

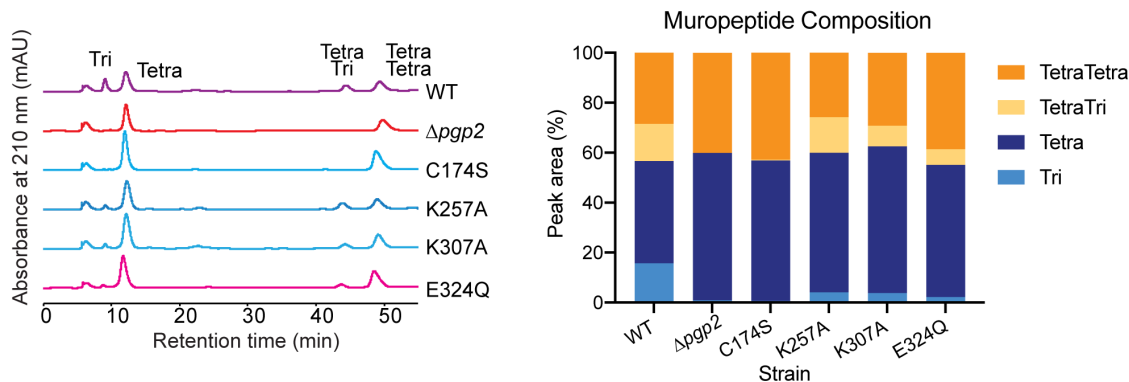


Figure 3-3. HPLC muropeptide profile of *C. jejuni* wild-type, $\Delta pgp2$ and $\Delta pgp2$ complemented with point mutations of the catalytic triad and within the NTF2 pocket

Purified PG digested with muramidase were reduced with sodium borohydride and separated by HPLC. Muropeptides were monitored by absorbance at 210 nm. Each peak is labeled with the corresponding muropeptide. The proportion of each muropeptide (Tri, Tetra, TetraTri or TetraTetra), relative to the combined total of these four muropeptides, are shown on the right.

3.2.4 The NTF2 domain binds PG

In some multi-domain PG hydrolases, the presence of a PG-binding domain enhances the activity of the catalytic domain (196,197). We examined whether the NTF2 domain functions as a PG binding domain that is synergistic with the LD-CPase domain for Pgp2 catalytic activity. A pull-down experiment was performed with Pgp2⁴³⁻³²⁵ and variants using $\Delta pgp2$ PG, which is rich in tetrapeptides. Wild-type Pgp2 was pulled down, demonstrating PG binding (**Figure 3-4**). Two catalytically inactive variants, C174S (Pgp2^{C174S}) and H157A (Pgp2^{H157A}), showed minimal association. The K307A variant (Pgp2^{K307A}), a conserved residue within the pocket of the NTF2 domain, was also weakly associated, supporting a role for this binding pocket for appreciable PG interaction. Mutation of conserved Y233 in the NTF2 domain (Pgp2^{Y233F}) was insufficient to disrupt the pull down of Pgp2 by PG. The removal of one hydroxyl group by replacement of tyrosine by phenylalanine was insufficient to substantively decrease PG binding.

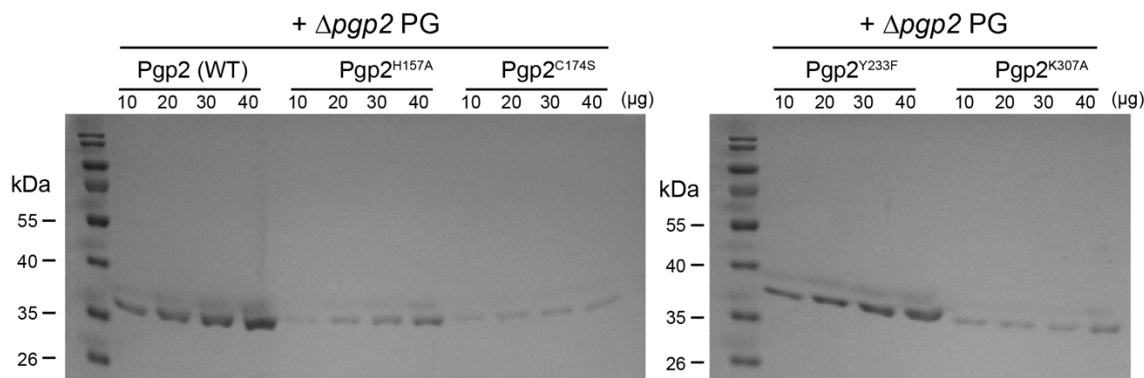


Figure 3-4. Binding of Pgp2 mutants to $\Delta pgp2$ PG

Pgp2 and variant proteins pulled-down by PG isolated from *C. jejuni* $\Delta pgp2$. Pgp2 proteins at the indicated amounts were incubated with purified PG (50 μ g) in a 250 μ L reaction at 4 °C for 30 min, followed by centrifugation at 13,000 rpm for 10 min. Insoluble PG and pulled-down proteins were washed 3 times with 1 mL of buffer (50 mM Tris pH 7.0 and 150 mM NaCl) to remove unbound proteins. Insoluble PG and pulled-down proteins were analyzed by SDS-PAGE stained with Coomassie Blue.

3.2.5 Strands β 9- β 10 form a flexible lip of the NTF2 domain binding pocket

To investigate if the loss of PG binding by the Pgp2^{K307A} was due to conformational change, the crystal structure of this variant was solved at 1.85 Å resolution (**Table 3-1**). The Pgp2^{K307A} crystal structure contains two Pgp2^{K307A} molecules in one asymmetric unit that superimposed with an RMSD of 0.7 Å over 281 C α atoms. The fold of the Pgp2^{K307A} is similar to that of wild-type Pgp2 (RMSD of 1.5 Å over 277 aligned C α atoms). The largest deviation is located at residues 296-306 of strands β 9- β 10 (**Figure 3-5A to Figure 3-5C**), which form a protruding lower lip of the NTF2 domain binding pocket. An overlay of the structures of Pgp2, Pgp2^{K307A}, and *H. pylori* Csd6 (PDB ID: 4XZZ) showed the conformation of lower lip is more similar between the latter two (**Figure 3-5**). In the wild-type Pgp2 crystal structure, the average B-factor of β 9- β 10 (residues 292-310) was 53.4 Å², 1.8-fold higher than the average B-factor over all residues. We conclude that β 9- β 10 is conformationally flexible and may allow variation in ligand specificity.

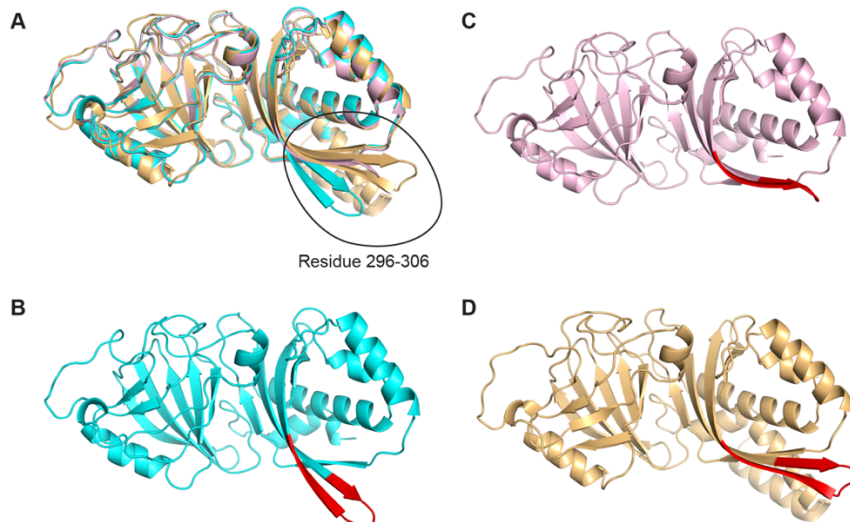


Figure 3-5. Superimpositions of the Pgp2, Pgp2^{K307A} and Csd6 structures

(A) Cartoon representation of an overlay of Pgp2 (cyan), Pgp2^{K307A} monomer B (pink) and Csd6 monomer A (orange, PDB ID: 4XZZ). Cartoon representation of Pgp2 (B), Pgp2^{K307A} (C), and Csd6 (D) structures. Residues 296-306 of strands β 9- β 10 form a flexible lip (circled or highlighted in red).

3.2.6 Identifying PG-binding interfaces of Pgp2 by NMR-monitored titrations

To identify PG interaction sites by NMR spectroscopy, triple labeled (^2H - ^{13}C - ^{15}N) Pgp2⁴³⁻³²⁵ was produced and used to obtain the assignments of 236 out of 287 expected main chain amide $^1\text{H}^{\text{N}}$ - ^{15}N signals (**Figure 3-6**). The unassigned residues include those in two loops (residues 167-173 and 238-253) for which conformational exchange may have led to resonance broadening. Although deuteration was required for resonance assignments of this 36 kDa protein, the ^{15}N -BEST-TROSY-HSQC spectrum of ^{15}N -labeled Pgp2⁴³⁻³²⁵ was of high quality (**Figure 3-7**), enabling titration experiments with panel of PG derived ligands.

Four PG ligand preparations for titration experiments were derived from digesting whole PG: a muramidase digestion of *C. jejuni* Δ p $gp2$ PG, a DL-endopeptidase (*Pseudomonas aeruginosa* Tse1) digestion of *E. coli* PG, HPLC purified murotetrapeptide, and HPLC purified cross-linked murotetrapeptides. The latter two ligands were treated with sodium borohydride before purification, which reduced the MurNAc residue. A fifth ligand was a synthesized peptide analogue (D-Glu-*m*-oxa-Dap-D-Ala) of the Pgp2 substrate (191).

In general, the $^1\text{H}^{\text{N}}$ and ^{15}N chemical shifts of many amides in Pgp2 changed progressively with added ligand (**Figure 3-8**). This corresponds to the fast exchange regime on the chemical shift timescale ($k_{\text{ex}} \gg \Delta\omega$, where k_{ex} is the interconversion rate constant and $\Delta\omega$ is the chemical shift difference between free and bound states) and is indicative of relatively weak binding (198). Such a response enabled their signals to be followed over the course of the titration, and their chemical shift perturbations (CSPs) to be calculated as the square root of the sum of the squared $^1\text{H}^{\text{N}}$ and ^{15}N chemical shift differences between the apo-versus ligand-bound protein at the titration endpoint (199). To define residues most perturbed by ligand binding, a CSP cut-off was determined for each given titration based on the average

CSP value for all residues, combined with patterns of clustering when mapped to the structure. In some cases, increasing linewidths and decreasing intensities of amide signals also occurred upon ligand binding (**Figure 3-9**). This typically corresponds to the intermediate exchange regime ($k_{\text{ex}} \sim \Delta\omega$) and could arise from larger amide chemical shift changes upon binding, or perhaps sensitivity to exchange between multiple bound conformations. Although precluding the measurement of CSP values, the patterns of such spectral perturbations aided in the identification of ligand binding sites.

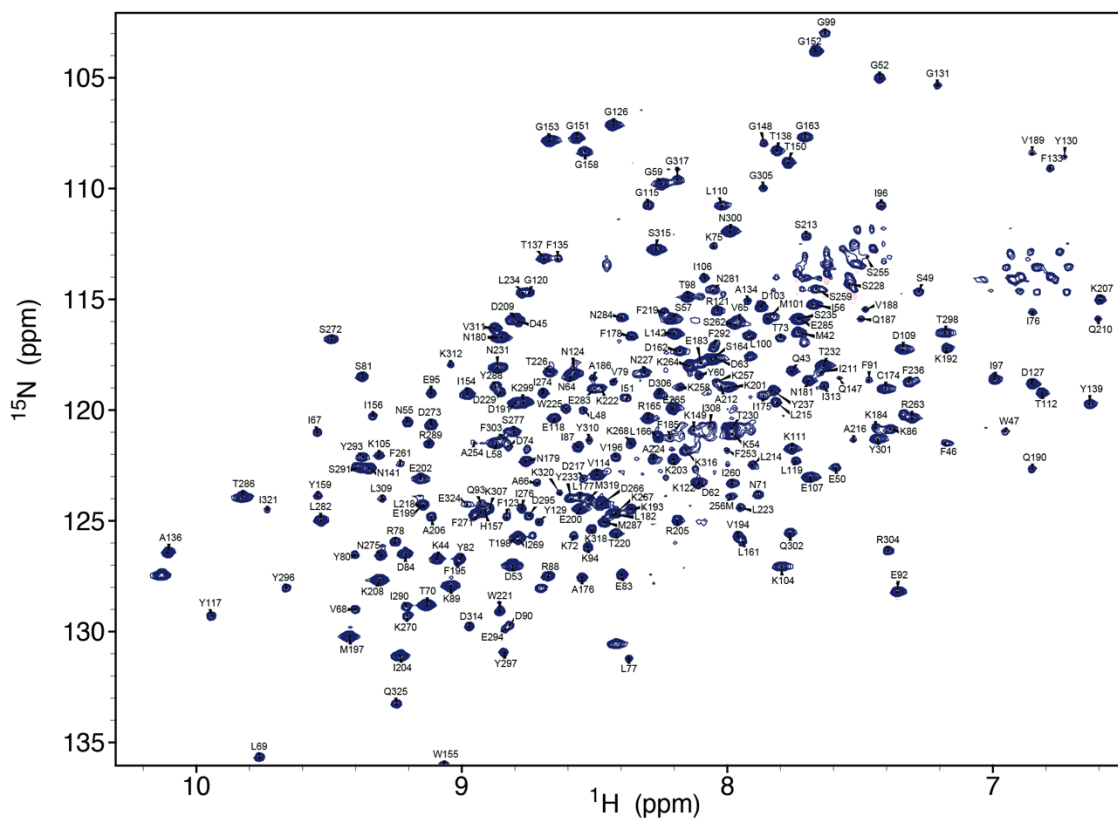


Figure 3-6. HSQC spectra of Pgp2 assignment of backbone amide ^{15}N and $^1\text{H}^{\text{N}}$ cross resonances

Assigned ^{15}N -BEST-TROSY-HSQC spectrum of a ^2H - ^{13}C - ^{15}N labeled Pgp2 sample, recorded at 25 °C with an 850 MHz NMR spectrometer. Based on 3D ^1H - ^{13}C - ^{15}N scalar correlation experiments, backbone amide ^1H - ^{15}N signals were automatically assigned using PINE, followed by manual verification with NMRFAM-SPARKY.

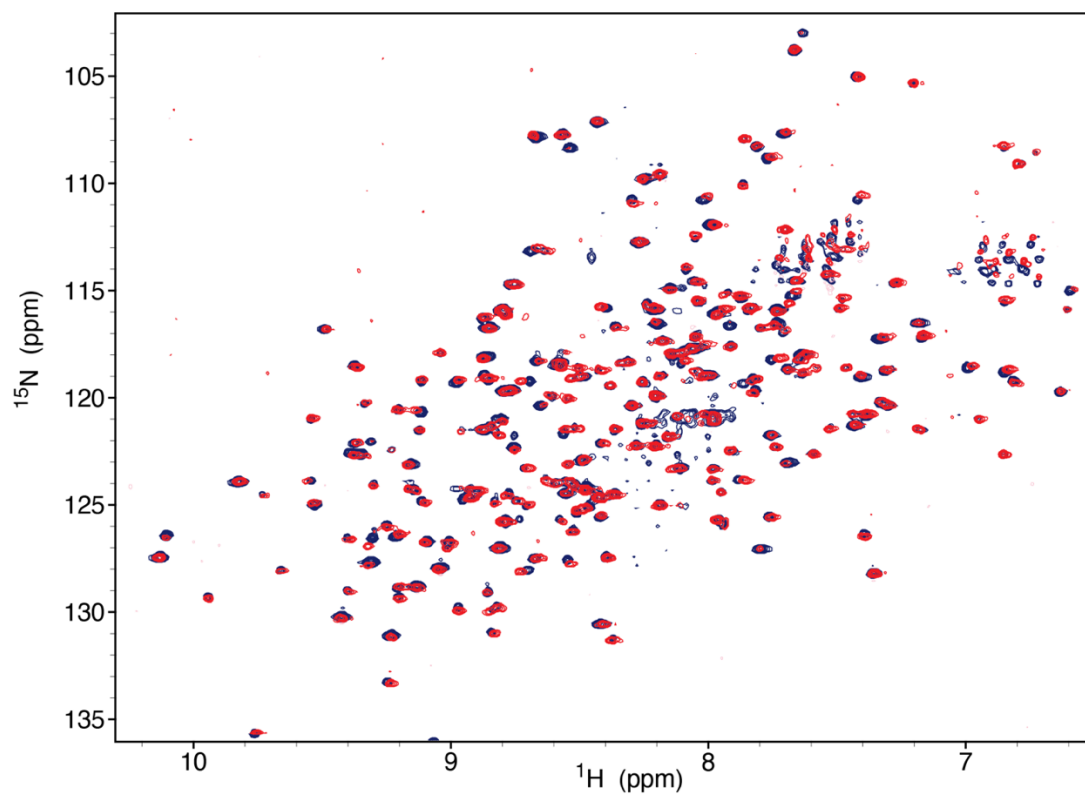


Figure 3-7. Overlaid HSQC spectra of ²H-¹³C-¹⁵N labeled and ²H-¹⁵N labeled Pgp2

Overlaid ¹⁵N-BEST-TROSY-HSQC spectra of Pgp2 uniformly labeled with only ¹⁵N (red) and with ²H, ¹³C and ¹⁵N (blue). Although deuteration was required to obtain assignments, ¹⁵N-labeling was sufficient for NMR-monitored titrations.

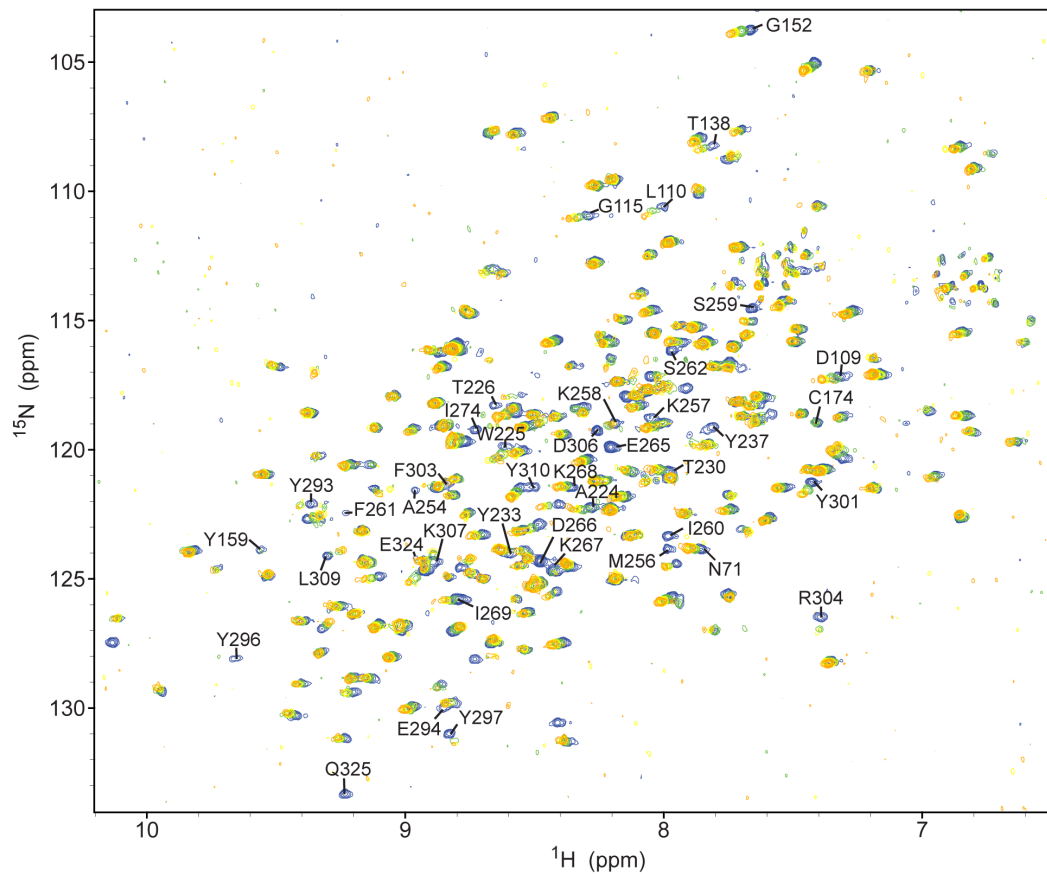


Figure 3-8. Overlaid ^{15}N -BEST-TROSY spectra of ^{15}N -labeled Pgp2 titrated with muramidase-digested PG from *C. jejuni* Δpgp2

Spectra colored blue, green, yellow and orange represent Pgp2 titrated with 0, 5, 10 and 20 μL of digested PG (60 $\mu\text{g}/\mu\text{L}$), respectively. Selected peaks from residues showing chemical shift perturbations or line broadening and signal loss over the course of the titration are labeled.

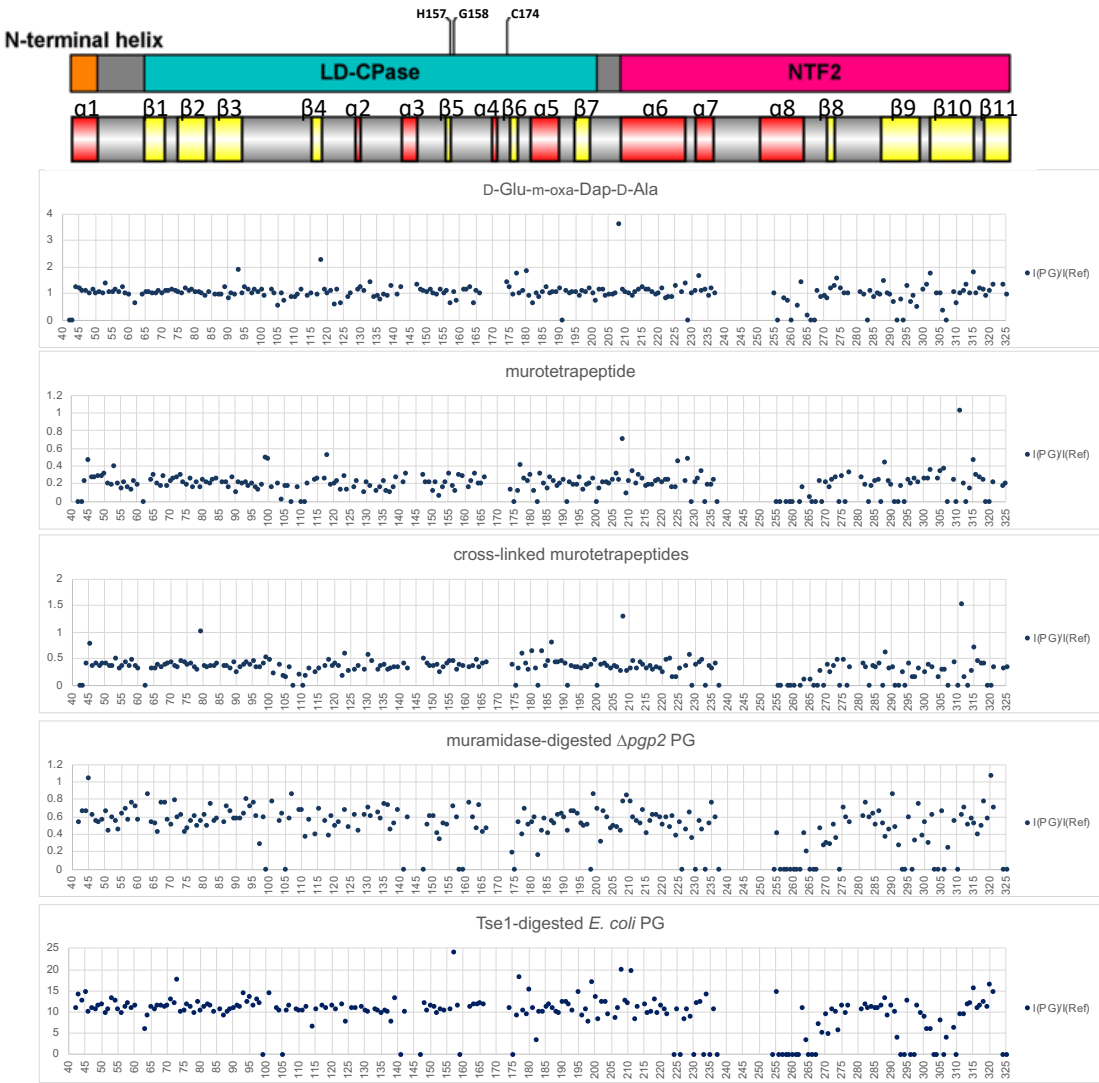


Figure 3-9. Relative intensity analysis of ^{15}N -labeled Pgp2 interacting with a panel of PG derived ligands

Relative intensity is calculated as $I(\text{PG})/I(\text{Ref})$, where $I(\text{Ref})$ and $I(\text{PG})$ denote the height of an amide $^1\text{H}^{N-15}\text{N}$ peak in ^{15}N -BEST-TROSY spectra recorded in the absence versus the presence of a PG ligand at the endpoint (highest) ligand:protein ratio for each given titration experiment. Signal intensities were not corrected for dilution (~0.99 with D-Glu-*m*-oxa-Dap-D-Ala, ~0.9 with the murotetrapeptide, cross-linked murotetrapeptides and muramidase-digested PG, and ~0.5 for the Tse1-digested *E. coli* PG) or in the case of Tse1-digested *E. coli* PG, increased acquisition time to better detect weaker signals.

Titration with D-Glu-*m*-oxa-Dap-D-Ala identified three patches of amides in the protein with CSP values above the cut-off (**Figure 3-10 & Figure 3-11A**). These include a patch next to helix α 2 and strand β 5 of the active site in the LD-CPase domain (Y130, W155, H157 and Y159), consistent with slow hydrolysis of the synthetic substrate by Pgp2 (191). The second patch is located on the pocket of the NTF2 domain at helix α 8 and strands β 8- β 10 (S262, E265, K268, F271, D273, N275, I276, Y296-T298, Q302, R304, and D306). A cluster of residues along helix α 8 and strand β 9 also showed signal broadening during the titrations (M256, I260, D266, K267, F292). This confirms the role of the NTF2 domain in PG binding. The third small patch is primarily from a loop with low sequence conservation at the inter-domain interface (N281, L282 and N284-M287) along the surface on the opposite side of both the LD-CPase domain active site and the NTF2 domain pocket.

Titrations using purified murotetrapeptide resulted in amides with line broadening or CSPs above the cut-off localized to three main patches (**Figure 3-10 & Figure 3-11B**). One patch, which includes helix α 2, strand β 5 and nearby loops (F123, Y130, F133-F135, T137, G152, G153, W155, H157, Y159, L166, C174 and L177), corresponds to a more extended interface near the Pgp2 active site than seen with the synthetic peptide. The second patch lies on the NTF2 pocket with residues within helices α 7- α 8 and strands β 9- β 11 showing extensive line broadening. The third backside patch is located at loops between the two domains (N281-L282 and N284-T286, E202-I204, D314-K316, K318), and is more extended than seen with the peptide titration. Titration of purified cross-linked murotetrapeptides identified the same three patches (**Figure 3-10 & Figure 3-11C**). No significant differences in the patterns of amide spectral perturbations were observed between monomeric murotetrapeptide and cross-

linked murotetrapeptides. This suggests that, even when cross-linked, the murotetrapeptides (and the synthetic peptide) bind to distinct interaction surfaces on Pgp2.

A titration with muramidase-digested $\Delta pgp2$ PG identified a predominant patch within the NTF2 pocket that includes residues A224, W225, K268, I269, Y297 and K307, which are located along helix α 6 and strands β 8- β 10 within the NTF2 pocket (**Figure 3-8, Figure 3-10 and Figure 3-11D**). Considerable resonance broadening was also observed for the nearby residues, including Y233 and Y237 of helix α 7, A254 and M256-S262 of helix α 8, E265-K267, and residues of strands β 9- β 11. An analysis of peak intensity changes over the course of the titration revealed the largest reductions for amides on strands β 8- β 10 of the NTF2 domain (I269-F271, D273, F292, Y297, K299, Y301 and K307) (**Figure 3-9**). Thus, under the conditions of this titration experiment, the digested PG mixture primarily bound to the NTF2 pocket.

Titration with Tse1-digested *E. coli* PG showed patterns of small CSPs for amides located at helices α 6 and α 8 (T220, W225, R263 and K264), and strands β 8- β 10 (F271, D273, I276, L282-N284, S291-F292, Y301, G305, K307 and L309) along the NTF2 domain pocket (**Figure 3-10 & Figure 3-11E**). In addition, resonance broadening was associated with residues on helices α 6- α 8 and strands β 9- β 11. Thus, Tse1-digested *E. coli* PG also bound to the pocket of the NTF2 domain, with little measurable association near the active site of the LD-CPase domain. This may reflect a relatively low endpoint concentration of the PG used for the titration and a decrease in tetrapeptides due to the cleavage mechanism of Tse1 (200). As perturbations of resonances of residues in the NTF2 pocket were observed by NMR when titrating with PG fragments, including residues that when mutated gave rise to a straight

phenotype (Y233, K257, K307), binding of PG by the NTF2 domain may be a necessary for *C. jejuni* helical shape generation.



Figure 3-10. Chemical shift perturbation (CSP) analysis of ¹⁵N-labeled Pgp2 interacting with a panel of PG-derived ligands

CSP values ($\Delta\delta$) were calculated for each residue by $\Delta\delta = \sqrt{(\Delta\delta_H)^2 + (0.14 * \Delta\delta_N)^2}$, where $\Delta\delta_H$ and $\Delta\delta_N$ denote the observed changes of the amide ¹H^N and ¹⁵N chemical shifts in the absence versus presence of a PG ligand at the endpoint (highest) ligand:protein ratio for each given titration experiment (see methods). Residues above and below the indicated CSP cut-off values are colored in red and gray, respectively. Residues that showed shift perturbations that could not be quantitated due to line broadening or severe intensity loss are colored in light orange (Figure 3-9). Blank values correspond to prolines and residues with overlapping or unassigned signals. Residues that when mutated exhibited straight cell shape phenotype (H157, C174, Y233, K257, K307) are marked with arrow in the bar graph.

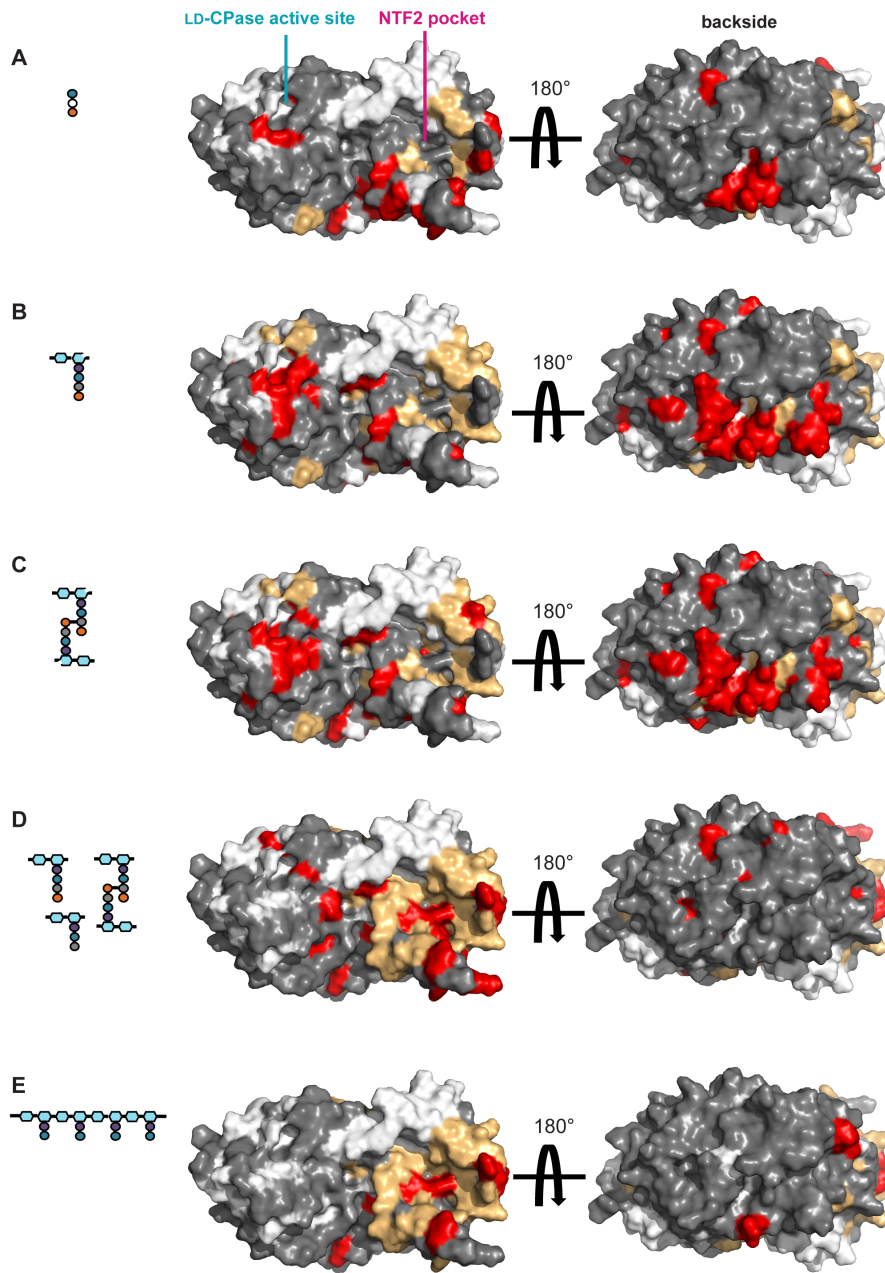


Figure 3-11. Interaction surfaces of Pgp2 with PG ligands identified from NMR-monitored titrations

(A) D-Glu-*m*-oxa-Dap-D-Ala. (B) HPLC purified murotetrapeptide. (C) HPLC purified cross-linked murotetrapeptides. (D) Muramidase-digested Δ pgp2 PG. (E) DL-endopeptidase (*P. aeruginosa* Tse1) digested *E. coli* PG. A representation of the ligand used in each experiment is shown as a diagram (hexagons: glycan backbone; circles: peptide residues; open hexagons: reduced MurNAc). Amide CSP values of ^{15}N -labeled Pgp2 upon titration with the indicated PG ligand (**Figure 3-10**) are mapped onto the protein surface (residues above the CSP cut-off in red; residues below the cut-off in gray; prolines and residues with unassigned signals in white). Also identified in orange are amides for which CSP values could not be determined due to severe signal line broadening (**Figure 3-9**).

3.2.7 NMR data-driven docking to identify binding modes between Pgp2 and PG

NMR-monitored titrations identified three major PG binding sites: the catalytic cleft, the NTF2 pocket and a backside patch. The titration with purified murotetrapeptide exhibited the largest continuous patch of perturbed residues in the catalytic cleft and the backside patch, and the muramidase-digested PG mixture displayed extensive perturbations in the NTF2 pocket. These two NMR titration datasets were therefore chosen for computational docking experiments using HADDOCK (184,189) to construct a model of the Pgp2-PG complex. To overcome the inherent challenges of identifying bound conformations of a flexible ligand in molecular docking, an ensemble of murotetrapeptide conformers was derived by sampling molecular dynamic simulations using CNS. In addition, we used two Pgp2 crystal structures (WT and Pgp2^{K307A}) as initial docking conformers.

For the docking using CSP data from the murotetrapeptide titration experiment, an unambiguous distance restraint of 2.0 Å between the nucleophile (Cys174) and the carbonyl carbon of *m*-DAP was added. The top 200 docking solutions were grouped into 5 clusters with a coverage rate of 92.5% (185/200) (**Table 3-2**). The largest cluster (88 solutions) had the best HADDOCK score with reasonable distances between nucleophilic C174 and the carbonyl carbon of *m*-DAP (**Figure 3-12A**). Contacts within the complex were primarily between the active cleft and peptide moiety, with minor interactions between the protein and sugar moiety. Within this cluster, all disaccharides point away from the active cleft. The second major cluster (68 solutions) features contacts primarily between the murotetrapeptide and loops of the domain interface on the backside of Pgp2 (**Figure 3-12A**). The solutions in this cluster are catalytically unfavorable because the nucleophilic attack distance for C174 is over 18 Å.

For docking using the CSP data from the titration with muramidase-digested PG, no unambiguous distance restraints were included. The top 200 solutions grouped into 5 clusters with a coverage rate of 95.5% (191/200) (**Table 3-2**). The largest cluster (126 solutions) had the best HADDOCK score, featuring strands β 8- β 12 and helix α 8 of the NTF2 domain pocket interacting with the peptide moiety (**Figure 3-12B**). The contact regions within the second cluster (31 solutions) are similar to cluster 1 but positions the backbone sugar in the reverse direction. The remaining clusters had poor scores with small buried surface areas.

Selecting the best solutions from the docking of a murotetrapeptide to the catalytic and NTF2 domains (**Figure 3-12C**), we generated a model of Pgp2 bound to PG by manually building a bridging peptidoglycan polymer between the two docked muropeptides, which are ~40 Å apart (**Figure 3-13A**). This PG strand runs the length of the Pgp2 molecule. Csd6 is a dimer formed by a small dimerization domain at the N-terminus. Much of this domain is absent in the recombinant Pgp2 construct used in these biochemical studies. Based on homology to Csd6, full length Pgp2 is expected to also form a dimer. To model PG binding to the Pgp2 dimer, two Pgp2-PG complexes were superimposed onto crystal structure of the Csd6 dimer (PDB ID: 4XZZ) (**Figure 3-13B**). Remarkably, the two PG strands are on one face of the dimer and run antiparallel 32 Å apart, close to the inter-stand distance of model crosslinked PG (201).

Table 3-2. HADDOCK calculation statistics of Pgp2-murotetrapeptide complexes

Docking experiment	Murotetrapeptide	Muramidase-digested PG				
AIR ^a						
Pgp2 active residues ^b	74,87,111,266,273,282 ,284,286	64,87,110,138,152,225,262,264,268,293,297,2 99,301,304,306,324				
Pgp2 passive residues ^b	55,62,63,73,83,86,88,8 9,95,105,106,107,108, 121,122,124,127,128,1 29,132,138,145,147,15 0,153,161,164,165,168 ,170,172,178,183,201, 202,203,205,245,264,2 65,268,272,283,285,29 3,296,304,325	44,45,48,49,50,53,54,55,57,62,63,73,74,75,83, 84,86,88,89,105,106,107,108,111,118,120,136 ,145,147,150,153,168,169,170,172,190,192,19 3,201,202,203,204,205,207,208,209,210,223,2 27,229,231,232,235,239,240,241,243,244,245, 248,250,252,255,256,258,259,260,263,265,26 6,270,272,273,281,282,295,296,298,300,302,3 03,325				
murotetrapeptide active residues ^b	3	1,2,3				
murotetrapeptide passive residues ^b	1,2					
Cluster^c						
Number	1	2	1	2	3	4
HADDOCK score	-52 ± 11	-35 ± 8	-81 ± 8	-54 ± 12	-59 ± 13	-30 ± 16
Average RMSD (Å) between structures	1.0 ± 0.5	0.8 ± 0.3	1.3 ± 0.5	0.8 ± 0.4	0.9 ± 0.4	0.99 ± 0.5
No. of structures	88	68	126	31	16	11
Buried surface area (Å ²)	810 ± 153	835 ± 118	1131 ± 116	1034 ± 138	833 ± 64	859 ± 143
E _{intermolecular} (kcal/mol)	-19 ± 59	24 ± 26	-234 ± 79	-91 ± 55	-179 ± 64	-48 ± 57
E _{non-bonded} (kcal/mol)	-252 ± 49	-181 ± 46	-319 ± 51	-225 ± 53	-32 ± 83	-134 ± 66
Evan der Waals (kcal/mol)	-31 ± 7	-34 ± 7	-41 ± 7	-37 ± 7	-23 ± 5	-28 ± 4
Electrostatic (kcal/mol)	-221 ± 52	-147 ± 48	-278 ± 49	-187 ± 49	-298 ± 84	-106 ± 65
E _{ambiguous intermolecular restraints} (kcal/mol)	233 ± 34	205 ± 31	85 ± 56	134 ± 40	142 ± 52	-87 ± 45
No. of AIR violations	3.6 ± 0.5	2.9 ± 0.7	2.4 ± 1.2	3.3 ± 1.0	3 ± 1.2	2.2 ± 1.1

^aThe AIR residues were defined based on NMR CSP data and mutagenesis studies.

^bThe number for Pgp2 corresponds to the amino acid number in the native sequence. The number 1, 2, and 3 for the murotetrapeptide corresponds to the residues GlcNAc, MurNAc and tetrapeptide.

^cIn each cluster, the energetic statistics were calculated over the 10 structures with the best HADDOCK scores.

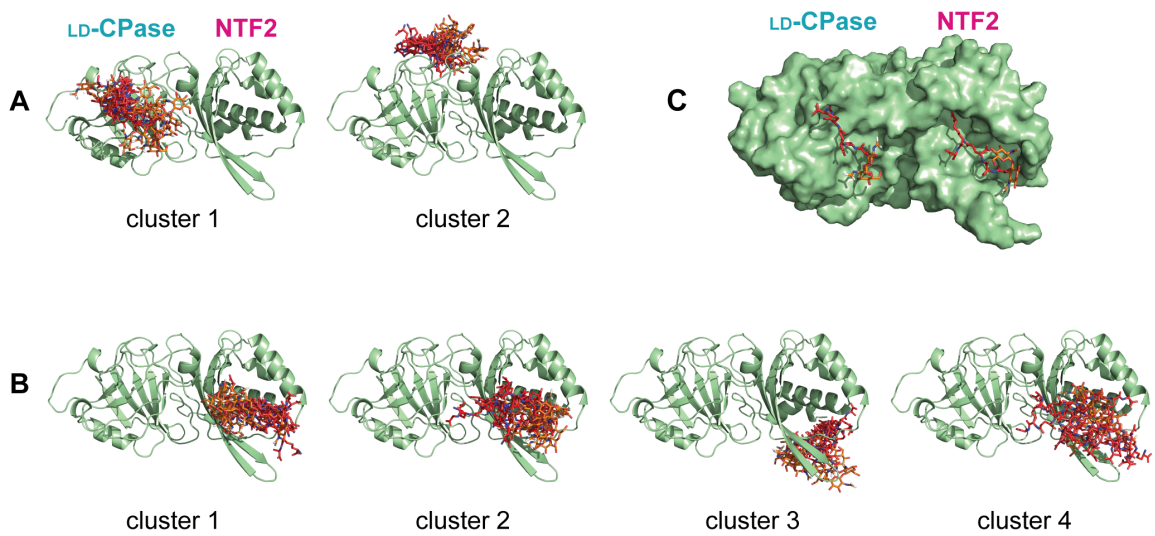


Figure 3-12. HADDOCK models of the Pgp2-murotetrapeptide complexes driven by NMR spectral perturbations

The top 10 scoring docking solutions from each of the dominant clusters (with >10 solutions) in each docking experiment are displayed. Pgp2 is shown in green. The bound murotetrapeptide is shown in stick form, where the sugar and peptide moieties are colored orange and red, respectively. (A) Clusters identified from docking using CSP data from the murotetrapeptide titration experiment. (B) Clusters identified from docking using CSP data from the muramidase-digested PG titration experiment. (C) Superimposition of the best HADDOCK scoring models for the murotetrapeptides (stick form) bound to the LD-CPase and NTF2 domains.

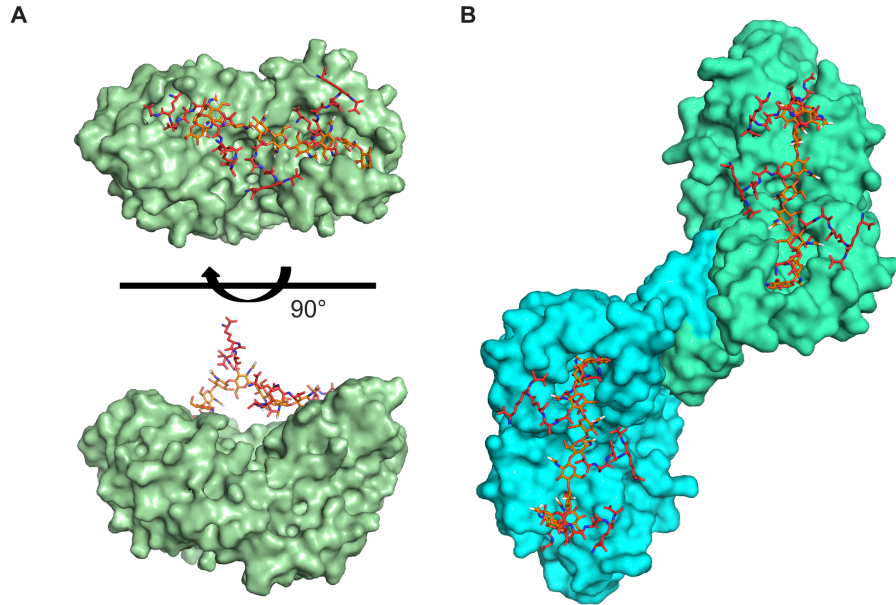


Figure 3-13. The Pgp2-PG binding model

(A) A Pgp2-PG binding model manually built by bridging the murotetrapeptides bound to the LD-CPase and NTF2 binding sites through a penta-disaccharide peptidoglycan polymer. Each MurNAc residue is attached to one tetrapeptide. PG is shown in stick form. The sugar is colored orange and tetrapeptide is colored red, respectively. Pgp2 is shown as a surface representation. (B) A dimer Pgp2-PG binding model made by superimposition of two copies of the Pgp2-PG model onto the dimeric Csd6 crystal structure (PDB ID: 4XZZ). The monomers are colored cyan and green, respectively.

3.3 Discussion

Pgp2 is annotated to be within the YkuD protein family (Pfam entry ID: PF03734) (202), which are LD-transpeptidases (LD-TPase) with a conserved catalytic triad of Cys, His and the main-chain carbonyl of a third residue (Gly in Pgp2) (203). LD-TPases bind two muropeptide stems in the active cleft to catalyze the formation of (L) *m*-Dap³→(D) *m*-Dap³ (3-3) cross-links (204). However, the catalytic cleft of Pgp2 can only accommodate a single muropeptide and a water molecule for peptide bond hydrolysis. Superimposition of the LD-CPase domain of Pgp2 and the LD-TPase domain of LdtMt5 from *Mycobacterium tuberculosis* (PDB ID: 4Z7A) revealed that the Pgp2 loops composed of residues 102-115 and 138-151

block the entry of an acyl receptor, consistent with the absence of 3-3 cross-links in *C. jejuni* PG (46).

The catalytic domain of Pgp2 shares conserved features with Csd6, the LD-CPase from *H. pylori* (**Figure 3-14**). The arrangement of the catalytic triad (C174, H157 and G158) is conserved. Also conserved are residues (E107, Y130, and W155, Pgp2 numbering) interacting with two bound D-Ala molecules observed in the Csd6 active site (137). One D-Ala is proposed to mimic the binding of the D-Ala residue of the peptide stem substrate whereas the second D-Ala is thought to bind in the *m*-DAP subsite. Despite these similarities, Pgp2 cleaved both monomeric and cross-linked tetrapeptides in a biochemical assay with recombinant enzyme containing the predicted dimerization domain (residues 19-325) and purified *C. jejuni* PG (49), whereas the equivalent Csd6 construct (residues 18-303) fully cleaved monomeric tetrapeptides with only trace digestion of cross-linked tetrapeptides in purified *H. pylori* PG (127). We assayed the same purified *H. pylori* Csd6 construct with *C. jejuni* PG and observed digestion of both monomeric and cross-linked tetrapeptides (**Figure 3-15**). Taken together, the difference in activity may thus be due to the differing PG architectures as opposed to enzyme substrate specificity differences.

Our pull-down data demonstrate that both the LD-CPase and NTF2 domains of Pgp2 are required for high affinity binding to PG (**Figure 3-4**), a feature not previously observed for the LD-CPase enzyme family. Many cell wall enzymes contain a non-catalytic NTF2 domain in addition to their catalytic module. For example, an NTF2 domain is found in a subset of class B penicillin binding proteins (143,205), the DD-endopeptidase NlpD and β -lactamase (144). These NTF2 domains may also be required for high-affinity PG binding, playing a role in the recognition of specific local PG structural features and guiding catalysis. Characterizing

the structures and substrate preferences of the NTF2 domain from these enzymes will determine how this domain is adapted to diverse roles in PG metabolism.

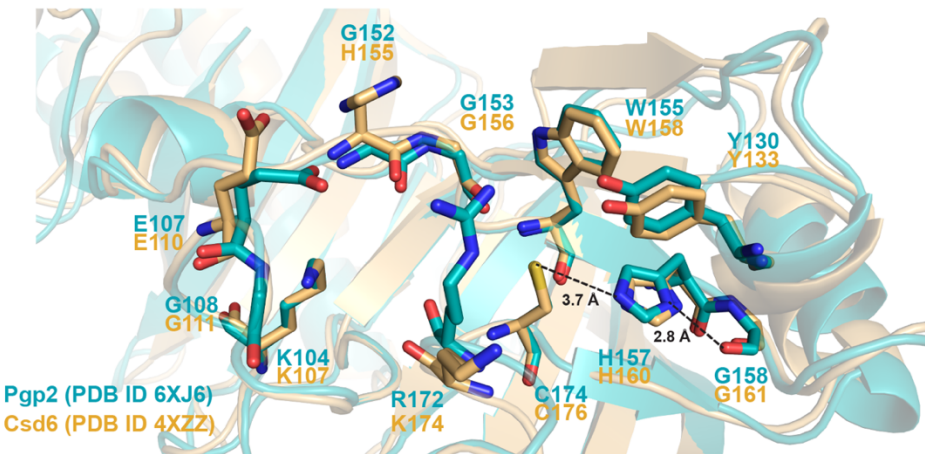


Figure 3-14. Superimpositions of active sites of Pgp2 and Csd6 structures

Superimposition of the active sites of Pgp2 (PDB ID: 6XJ6) and Csd6 (PDB ID: 4XZZ). Residues of the catalytic triad and substrate binding site are shown in stick form (nitrogen, blue; oxygen, red; sulfur, yellow). A hydrogen bond network between residues of the triad is drawn as dashed lines.

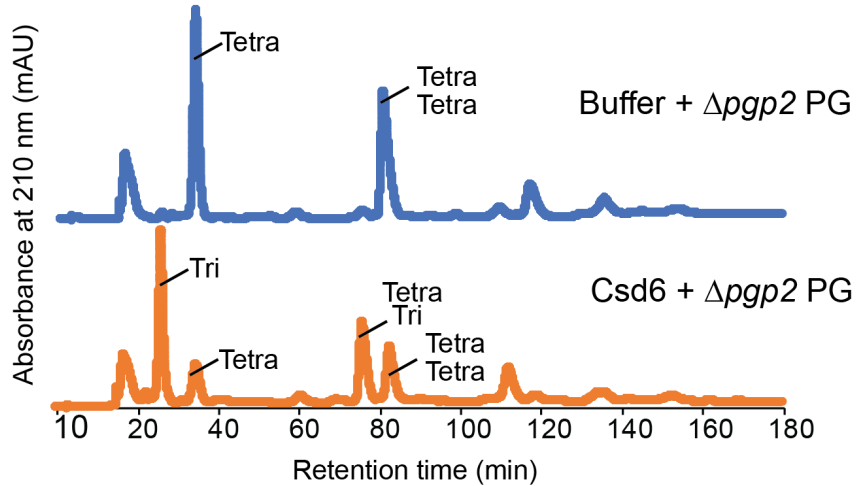


Figure 3-15. $\Delta pgp2$ PG digestion by Csd6

HPLC muropeptide profile of purified *C. jejuni* $\Delta pgp2$ PG after digestion with Csd6. Samples were separated on a C₁₈ column using a gradient from 100% buffer A (50 mM sodium phosphate pH 4.3) to 100% buffer B (50 mM sodium phosphate pH 4.9 and methanol 15% (v/v)) over 200 minutes. Muropeptides were monitored by absorbance at 210 nm. HPLC results are plotted as the intensity of absorbance (in units of mAU, y-axis) as a function of column retention time (in units of min, x-axis).

We observed extensive NMR spectral perturbations clustered into three regions on the surface of Pgp2 upon titration with model PG ligands (i.e., the CPase active site, the NTF2 pocket and a third backside patch; **Figure 3-11A to Figure 3-11C**). The conserved CPase active site and NTF2 domain pocket are ~40 Å apart along the same side of the protein surface. The glycan backbone of PG was proposed to preferentially form a right-handed helix with a periodicity of 30-40 Å, or approximately three to four GlcNAc-MurNAc repeats with successive peptide stems projecting outward from the glycan strand screw axis (185,206). As the top solutions from NMR-data driven docking at both domains position two bound murotetrapeptides oriented such that they can originate from a single right-handed PG strand (**Figure 3-12C**), we propose this as the most parsimonious Pgp2-PG binding model, an interaction that simultaneously involves both the catalytic and NTF2 cavities (**Figure 3-13A**).

The backside patch features low sequence conservation and was prominent during titrations with the synthetic peptide analog and purified monomeric and crosslinked murotetrapeptides (**Figure 3-11A to Figure 3-11C**). Situated between the two domains, the region may be involved in allosteric coupling of the two frontside binding sites. Neither the third patch nor the active site exhibited strong relative perturbations when titrated with enzymatically digested PG (**Figure 3-11D & Figure 3-11E**). This may reflect low relative concentrations of each muropeptide in the PG mixture and complex binding dynamics arising from multiple binding sites.

Pgp2 likely forms a higher oligomerization state within the bacterial cell. The Pgp2 homolog Csd6 dimerizes through three N-terminal helices from each monomer, building a six-helix bundle (137). The hydrophobic dimer interface of Csd6 is composed of the sequence **IMRLYX₃GLEMV**. The N-terminal residues, including the hydrophobic dimer interface

(LVRIYX₃GLDAV), are conserved in Pgp2 but missing in the truncated recombinant construct. We used the crystal structure of the Csd6 dimer (PDB ID: 4XZZ) and our PG docking data to predict the interaction of a Pgp2 dimer with PG (**Figure 3-13B**). In this model, the PG interaction interface of both Pgp2 monomers is on the same face of the dimer. The Pgp2 dimer can interact with two PG strands ~32 Å apart, allowing for recognition of an ordered PG tertiary structure that may direct patterned digestion of the PG to form helical shape.

Some Pgp2 and PG structural features were not included in the generation of the proposed model. Firstly, the docked murotetrapeptides did not include acetylation at O6 of MurNAc. Secondly, strands β9-β10 which form the lip of the NTF2 pocket are flexible (**Figure 3-5**) and this flexibility may alter binding specificity. Lastly, a more complex PG binding model is possible in which the two muropeptides bound to the active site and NTF2 domains originate from separate glycan strands ~40 Å apart. In this alternate model the Pgp2 dimer could interact with up to four distinct PG strands. Solid-state NMR can be used to calculate the ¹³C-¹⁵N inter-nuclear distance of D-[1-¹³C]Ala and L-[¹⁵N]Ala labeled PG peptide stems (207), and may be able to resolve these possibilities. Attempts to co-crystallize Pgp2 with synthesized peptide D-Glu-*m*-oxa-Dap-D-Ala and purified murotetrapeptide were ultimately unsuccessful.

Bacterial cell shape requires the spatial coordination of PG insertion (103). A localized ‘shapesome’ complex, coordinated across the cytoplasm, inner membrane, and periplasm, is proposed to contribute to helical shape generation in *H. pylori* via asymmetrical cell wall synthesis (128,130,133). However, no interactions were identified between Pgp2 and PG synthesis machinery. Biophysical modeling suggests that spatially-targeted PG growth

(120,123,208) or changes to the degree of cross-linking along a helical axis can lead to a helical cell shape (52,209). Neither overall growth rates (49) nor cell length (**Figure 3-2B**) were affected upon the deletion of Pgp2. However, Pgp2 may modulate spatial PG insertion or cross-linking. The percentage of cross-links are similar between the wild-type (47.9%) and $\Delta pgp2$ (47.6%) strains (49), suggesting the overall proportion of cross-links is not sufficient to determine helical shape. Instead, the deletion of Pgp2 increases the ratio of tetra-tetra to tetra-tri crosslinks due to the absence of tripeptides (49). In *H. pylori*, the overall proportion of cross-links is also unaffected upon the deletion or overexpression of Csd6, but the ratio of tetra-tetra to tetra-tri cross-linked peptide stems varies (127). Both deletion and overexpression of Csd6 gives a straight cell shape, suggesting that helical shape requires a proper balance between these two types of cross-links.

We show that Pgp2 has higher enzymatic activity on monomeric as compared to cross-linked peptides (**Figure 3-3**), consistent with previous experiments using synthetic model peptides and purified PG (49,191). By mutating conserved NTF2 domain pocket residues, we demonstrate that this domain impacts enzyme activity and is required for the preference for monomeric substrates in *C. jejuni*. Point mutations in the NTF2 domain resulted in a 75-86% reduction in the proportion of monomeric tripeptide products in *C. jejuni* PG as compared to wild-type. The same mutations reduced cross-linked tetratripeptides by 5-59% in the same samples. Clearly, muropeptide distribution is insufficient to determine shape phenotype. The NTF2 domain mutants (K257A, K307A, E324Q) have a similar loss in monomeric and cross-linked tripeptides but differ in shape phenotype ranging from curved to straight rods (**Figure 3-2A & Figure 3-2B**). Nonetheless, these mutants may differ in function, such as modified localization or targeting of PG substructures, that would lead to the shape phenotypes.

Based on the evidence that NTF2 domain binds to PG and regulates Pgp2 activity, we propose that preferential trimming of monomeric tetrapeptides by Pgp2 is localized to one of the helical axes. Since tripeptides produced by Pgp2 can be further digested to release *m*-DAP by the DL-carboxypeptidase Pgp1 (49), they are no longer able to form crosslinks. Thus, Pgp2 activity along a helical axis may allow for local relaxation of the PG, leading to cell twist. Future examination of Pgp2 localization and involvement of the NTF2 domain will test this model.

The requirement of Pgp2 for helical shape may serve as a basis for antimicrobial development as *C. jejuni* colonization within the host could be reduced. This strategy was successfully employed to target Pgp1 and the *H. pylori* homolog Csd4 (166). Incubation of bacteria with a small molecule inhibitor of the carboxypeptidase domain results in a morphological shift from helical to straight rod cells. Unlike the LD-CPase domain, which is found in both helical and non-helical shaped cells, the NTF2 domain appears to be restricted to helical shaped cells, suggesting that the NTF2 domain may be a more selective target.

In summary, we show that helical shape in *C. jejuni* depends on both the LD-CPase and NTF2 domains of Pgp2. Our proposed Pgp2-PG model highlights the importance of PG-binding by the NTF2 domain that may guide Pgp2 activity through recognition of PG architecture.

CHAPTER 4: Role of the CBM35 domain in the *O*-acetyl esterase Ape1

4.1 Introduction

C. jejuni helical cell shape is maintained by de-*O*-acetylation of PG by *O*-acetylesterase Ape1 (CjApe1), an enzyme that hydrolyzes acetyl group from *O*-acetylated MurNAc residues (54). Deletion of *ape1* resulted in bacteria with a highly curved morphology, a significant increase of *O*-acetylation level, and longer of PG glycan strands (54). Sequence analysis predicts CjApe1 contains a SGNH hydrolase domain and an uncharacterized CBM35 family domain. The role of CBM35 domain in CjApe1 function remains unclear. In this chapter, I present a 1.8 Å resolution crystal structure of a complex between acetate and CjApe1. An active site cleft is formed at the interface of the two domains and two large loops from the CBM35 domain are proposed to form part of the active site. Site-directed mutagenesis of residues in these loops coupled with activity assays using *p*-nitrophenol acetate indicate that the CBM35 loops are required for full catalytic efficiency. Molecular docking of a model *O*-acetylated hexasaccharide model substrate to CjApe1 gives insight into the PG binding mode. Together, we propose that the active cleft of CjApe1 diverges from other SGNH hydrolase members by using the CBM35 loops to assist catalysis. The concave CjApe1 active cleft may accommodate the long glycan strands for selecting PG substrates to regulate subsequent biological events.

4.2 Results

4.2.1 Structure determination of *C. jejuni* Ape1

C. jejuni Ape1 is a 392 amino acid protein containing a predicted signal peptide at residues 1-21 of the native sequence (*CJJ81176_0638*) (**Figure 4-1A**). The full-length mature protein (Ape1²²⁻³⁹²) was crystallized, and despite diffracting to high resolution (better than 1.6 Å), structure determination was impeded by crystal twinning. A truncated construct with residues 41-392 (Ape1⁴¹⁻³⁹²) was crystallized and its structure was solved to 1.8 Å resolution by single anomalous dispersion (SAD) with selenomethionine-labeled protein (SeMetApe1⁴¹⁻³⁹²). An initial model was automatically built with Phenix AutoBuild (210), resulting in three partial Ape1 monomers in the asymmetric unit. A continuous model was built for two monomers, with the third monomer incomplete due to disorder.

The native Ape1⁴¹⁻³⁹² protein structure was solved to 1.8 Å resolution by molecular replacement with one of the complete monomers from the SeMetApe1⁴¹⁻³⁹² structure. Three monomers were built and refined to R_{work} and R_{free} values of 0.17 and 0.19, respectively. The final model includes three complete Ape1 monomers (residues 41-392), with each monomer bound to one acetate molecule in the active site. The electron density for the acetate was clearly defined in electron density maps and was refined to an average B-factor of 20.7 Å². To explore the oligomeric state, Ape1⁴¹⁻³⁹² was analysed by SEC-MALS. In solution, the molecular weight was determined to be 37.3 ± 2.5% kDa, consistent with the predicted molecular weight of the recombinant Ape1 monomer (41.1 kDa).

The Ape1²²⁻³⁹² structure was solved by molecular replacement with Ape1⁴¹⁻³⁹² as the search model and refined assuming merohedral twinned to R_{work} and R_{free} values of 0.14 and 0.18. The Ape1²²⁻³⁹² and Ape1⁴¹⁻³⁹² structures are similar, with a RMSD of 0.16 Å over 352

aligned C α atoms. The Ape1²²⁻³⁹² structure also contains three monomers in the asymmetric unit and reveals an additional N-terminal helix (**Figure 4-1B**). The N-terminal helix of Ape1²²⁻³⁹² shows limited contacts to the rest of the protein and its sequence is not conserved amongst homologs from different species. As the Ape1⁴¹⁻³⁹² structure is of higher quality, it was used for all subsequent analyses and will be denoted as CjApe1. All data collection, phasing and refinement statistics are summarized in **Table 4-1**.

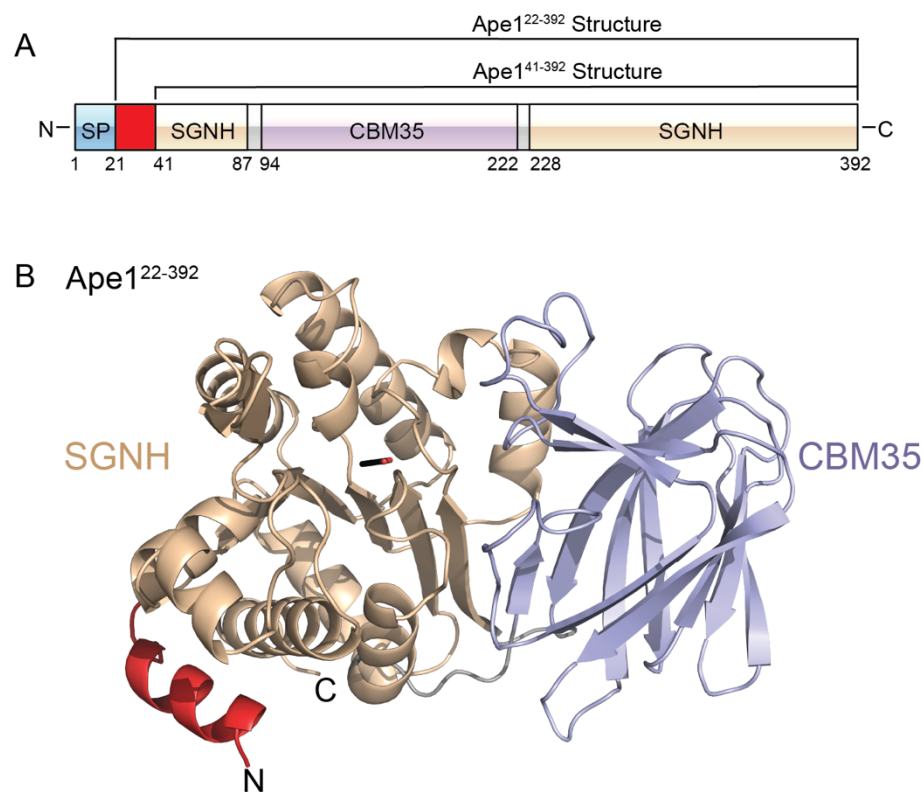


Figure 4-1. The crystal structure of *C. jejuni* Ape1

(A) Schematic representation of full-length Ape1 (SP = signal peptide). The regions corresponding to recombinant Ape1⁴¹⁻³⁹² and Ape1²²⁻³⁹² proteins are labeled. (B) The overall structure of acetate-bound Ape1²²⁻³⁹² with the N-terminal helix, SGNH and CBM35 domains colored in red, brown and light purple, respectively. The acetate is shown in stick form.

Table 4-1. Data collection and model refinement statistics of *C. jejuni* Ape1

	Ape1 ⁴¹⁻³⁹²	Selenomethionine- substituted Ape1	Ape1 ²²⁻³⁹²
Data collection^a			
Space group	P3 ₂	P3 ₂	P3 ₂
Cell dimensions			
<i>a</i> , <i>b</i> , <i>c</i> (Å)	94.9, 94.9, 102.7	95.3, 95.3, 103.1	95.3, 95.3, 103.0
α , β , γ (°)	90, 90, 120	90, 90, 120	90, 90, 120
Total reflections	546678	696966	271029
No. of unique reflections	95429	111763	46459
Wavelength (Å)	0.97946	0.97915	0.98011
Resolution (Å)	50.0–1.80 (1.83–1.80)	50.0–1.70 (1.73–1.70)	50.0–2.30 (2.34–2.30)
R _{merge}	0.100 (0.798)	0.087 (0.614)	0.148 (0.782)
I/σI	18.3 (1.7)	23.0 (2.6)	13.2 (2.3)
CC (1/2)	(0.810)	(0.859)	(0.653)
Completeness (%)	99.7 (99.7)	97.1 (98.6)	100 (100)
Redundancy	5.7 (5.1)	6.2 (6.4)	5.8 (5.8)
Refinement			
Resolution (Å)	34.9–1.80		43.70–2.30
R _{work} /R _{free}	16.7/18.8		14.3/18.1
Ramachandran			
Favored (%)	96.7%		96.2%
Allowed (%)	3.3%		3.8%
Outliers (%)	0%		0%
Average B factors (Å ²)			
Protein	27.2		30.71
Water	31.4		37.43
RMSDs			
Bond lengths (Å)	0.003		0.002
Bond angles (°)	0.562		0.510

^aValues for the highest resolution shells are shown in parentheses.

4.2.2 The overall structure of acetate-bound CjApe1

CjApe1 has a rigid two-domain structure with an SGNH hydrolase domain (residues S41-Y87 and Y228-Y392) and a CBM35 domain (residues I94-T222) interconnected by two short loops (residues L88-S93 and N223-N227) (**Figure 4-1**). An extensive interface, with a buried surface area of 1370 Å² as measured using PISA (192), is found between the SGNH and CBM35 domains. The domain-domain interaction is mediated by a hydrophobic core of 19 hydrophobic amino acids (Ala, Ile, Leu, Met, Val, Trp, Phe, Tyr) from the SGNH domain and 15 hydrophobic amino acids from the CBM35 domain.

The CjApe1 SGNH domain adopts a three-layer α/β/α fold, with a central five-stranded parallel β-sheet (β2, β14, β15, β16, β17) flanked by 10 α-helices (α1-α10) (**Figure 4-2A, top**). The invariant catalytic residues (S73, G237, N270 and H369) are situated within a concave surface above the parallel β-sheet of CjApe1 (**Figure 4-2A, bottom**). The catalytic triad (S73-D367-H369) form a hydrogen bonding network adjacent to a bound acetate molecule. Clear electron density for the acetate showed that one of the oxygen atoms as 2.7 Å from the amide of G237 and 2.9 Å from Nδ2 of N270, two residues that comprise the oxyanion hole. The methyl group of the acetate packs against a conserved hydrophobic cavity formed by L273 and V368. The orientation of the bound acetate thus likely represents a model for the tetrahedral oxyanion intermediate of the acetyl moiety of the substrate-enzyme complex.

The electrostatic surface potential of CjApe1 was investigated. The side of CjApe with the shallow active site had a largely positively charged surface. Rotating the molecule along the long axis by 90° showed a relatively neutral to negatively charged surface (**Figure 4-2B**). The positive charged surface of the CjApe1 may help to orient molecule such that the catalytic cleft is directed towards the negatively charged PG substrate for catalysis.

The CBM35 domain of CjApe1 is formed by two sandwiched antiparallel β -sheets (β 3, β 5, β 6, β 8, β 11, β 13 in the first sheet and β 4, β 7, β 9, β 10, β 12 in the second). A structural homolog search using Dali (193) identified CBM35 domains in various glycoside hydrolases (**Figure 4-3**). In these hydrolases, the inter- β -strand loops of the CBM35 domain often coordinate calcium ions and saccharides (165). Saccharide binding by this domain has been proposed to guide substrate specificity of the associated glycoside hydrolase domain (164,211). However, these CBM35 domains and CjApe1 shares sequence identities less than 11% suggesting the CBM35 domain of CjApe1 may have functions other than saccharide binding. Notably, two large loops of the CjApe1 CBM35 domain (CBML1 and CBML2) are situated close to the active cleft of the SGNH domain (**Figure 4-3E**). Inspection of the sequences of CBML1 (13 amino acids, A97-N109) and CBML2 (16 amino acids, N121-F136) identified conserved polar (Q105, Q106, N121, S122) and aromatic (Y104 and F132) residues. Inspection of the CjApe1 structure revealed that the side chains of Q105, N121 and R123 form hydrogen bonds with the main chain of the loop in the SGNH domain forming the oxyanion hole (residues A234-D240) (**Figure 4-3E**). A similar hydrogen bond network is found in NmApe1 (**Table 4-2**). We hypothesize that these residues of the CBM35 domain contributes to enzyme catalysis by stabilizing the oxyanion hole.

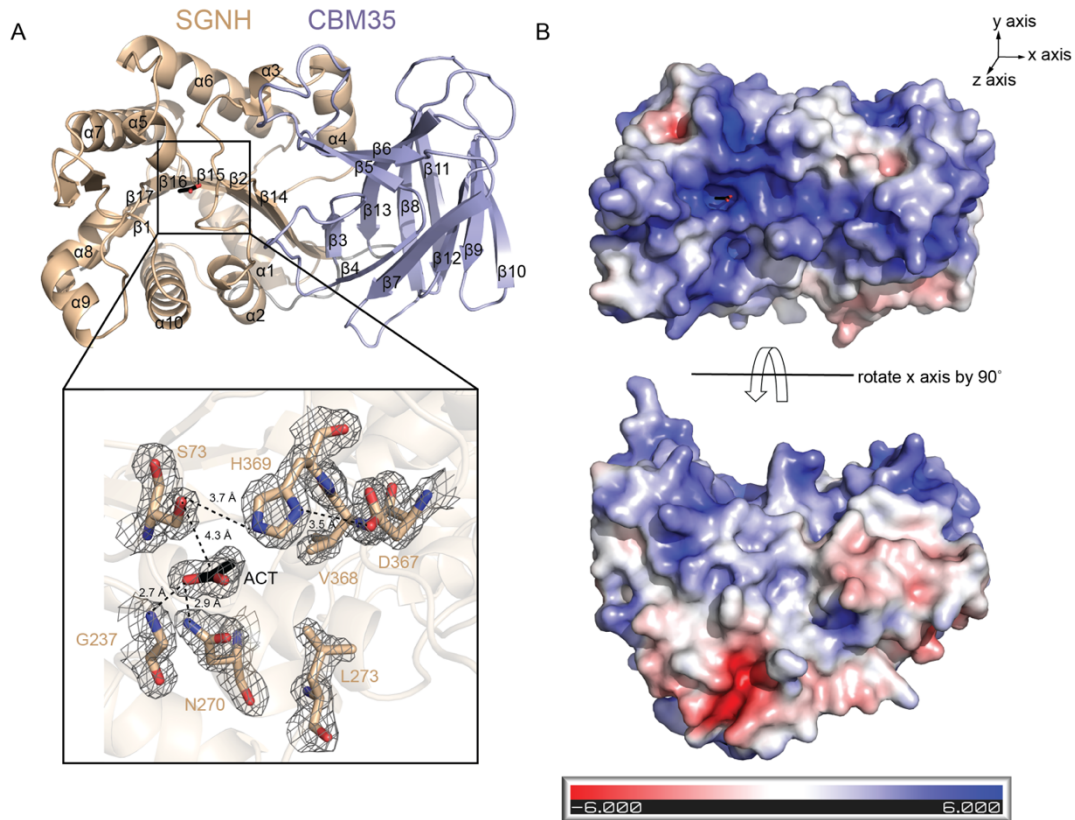


Figure 4-2. Active site arrangement and electrostatic potential properties of Ape1⁴¹⁻³⁹²

(A) Magnified view of the active site. The catalytic triad (S73-H369-D367), oxyanion hole (G237 and N270) and conserved hydrophobic residues (V368 and L273) are shown in stick form (nitrogen, blue; oxygen, red; carbon, brown). The electron density is shown as a weighted 2Fobs-Fcal map contoured at 1 σ . Hydrogen bond networks between residues of the triad are drawn as dashed lines. (B) The electrostatic potential ($\pm 6 \text{ kT/e}$) plotted onto the solvent accessible surface of CjApe1. The surface charge was calculated using the APBS plugin in PyMOL, and the input Ape1 structure containing charge and radius information for each atom was prepared using the PDB2PQR web server.

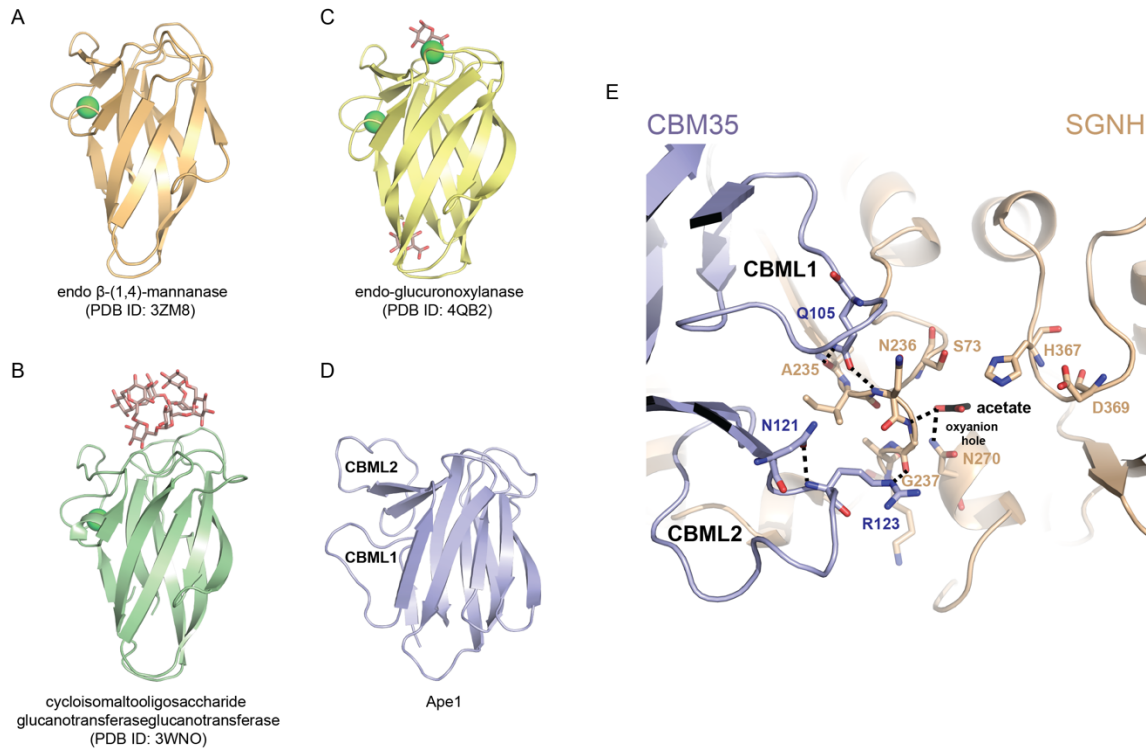


Figure 4-3. Structural comparison of CBM35 structural homologs

Comparison of CBM35 domain structural homologs: (A) *Campylobacter jejuni*, Ape1; (B) *Podospora anserina*, β-(1,4)-mannanase, PDB 3ZM8; (C) *Paenibacillus barcinonensis*, Xyn30D, PDB 4QB2; (D) *Bacillus circulans*, cycloisomaltooligosaccharide glucanotransferaseglucanotransferase, PDB: 3WNO. Bound calcium ions and bound saccharides are displayed in green sphere and stick form, respectively. (E) Residue Q105 of CBML1 and residue R123 of CBML2 make H-bonds to residue A235, N236, G237 of the oxyanion hole loop. H-bonds are shown as black dash lines between atoms.

Table 4-2. H-bond network between the CBM35 loop and the oxyanion hole

CjApe1		NmApe1 ^a			
CBM35	Oxyanion hole	CBM35	Oxyanion hole		
Q105, Ne2	A234, O	3.0	Q115, Ne2	G233, O	2.8
Q105, Oe2	N236, N	2.9	Q115, Oe2	N235, N	3.0
N121, Oδ1	R123, N	3.0	T130, Oγ1	R132, N	3.2
R123, Ne	G237, O	2.7	R132, Ne	N235, O	3.5

^aThe NmApe1 model is derived from PDB 4K7J.

4.2.3 Two CBM35 loops promote Ape1 *O*-acetyl esterase activity

To examine if these loops are required for CjApe1 deacetylase activity, site-directed variants of residues of CBML1 (K103A, Y104G, Q105A, Q106A) and CBML2 (N121A, S122A, R123A, F132A) were generated in the context of the full-length Ape1²²⁻³⁹² construct (**Figure 4-4A**). All purified CjApe1 variants were concentrated to higher than 9.5 mg/mL, suggesting the proteins are stable in solution. The *O*-acetyl esterase activity of the wild-type and variant proteins were assayed using *p*-nitrophenol acetate (*p*NPAc) as a substrate. Controls with *p*NPAc alone and *p*NPAc incubated with an inactive CjApe1 variant with a substitution of the catalytic nucleophile (S73A) showed minimal absorbance change at 405 nm (**Figure 4-4B & Table 4-3**). Wild-type CjApe1 cleaved *p*NPAc at a specific activity of 32 $\mu\text{mole}\cdot\text{min}^{-1}\cdot\text{mg}^{-1}$, which is consistent with previously measured CjApe1 activity (26.1–38.9 $\mu\text{mole}\cdot\text{min}^{-1}\cdot\text{mg}^{-1}$) (54). Wild-type activity levels were observed for the K103A (110%), Y104G (113%), Q106A (102%), S122A (101%) and F132A (95%) variants, indicating that replacement of these residues did not substantially reduce *O*-acetyl esterase activity (**Table 4-3**). On the contrary, reduced deacetylase activity was observed for variants Q105A (59%), N121A (60%), and R123 (34%), suggesting these residues are required for optimal CjApe1 catalysis.

To examine whether the reduced activity of the variants Q105A, N121A, and R123A was due to a deficiency in PG-binding, a PG pulled-down assay was performed. CjApe1 and variant proteins were incubated with insoluble *Aape1* PG, followed by centrifugation and wash steps. Proteins pulled down by PG isolated from *C. jejuni* *Aape1* were recovered from the pellet and quantified using SDS-PAGE. Protein pulled down in the absence of PG was minimal (**Figure 4-5**). Conversely, CjApe1 and variants were pulled down by *Aape1* PG. Relative PG binding was estimated by band densitometry analysis by comparing the amount of variant

protein pulled down to that of wild-type CjApe1. Slight reductions were observed for all variants tested: K103A (94%), Y104G (88%), Q105A (90%), Q106A (82%), N121A (85%), S122A (91%), R123A (88%) and F132A (78%) (**Figure 4-4C**); however, the discernable differences in the amount of protein pulled down did not explain the larger differences in *p*NPAc activity. The site-directed variants support a role for the CBML1 and CBML2 loops in deacetylase catalysis.

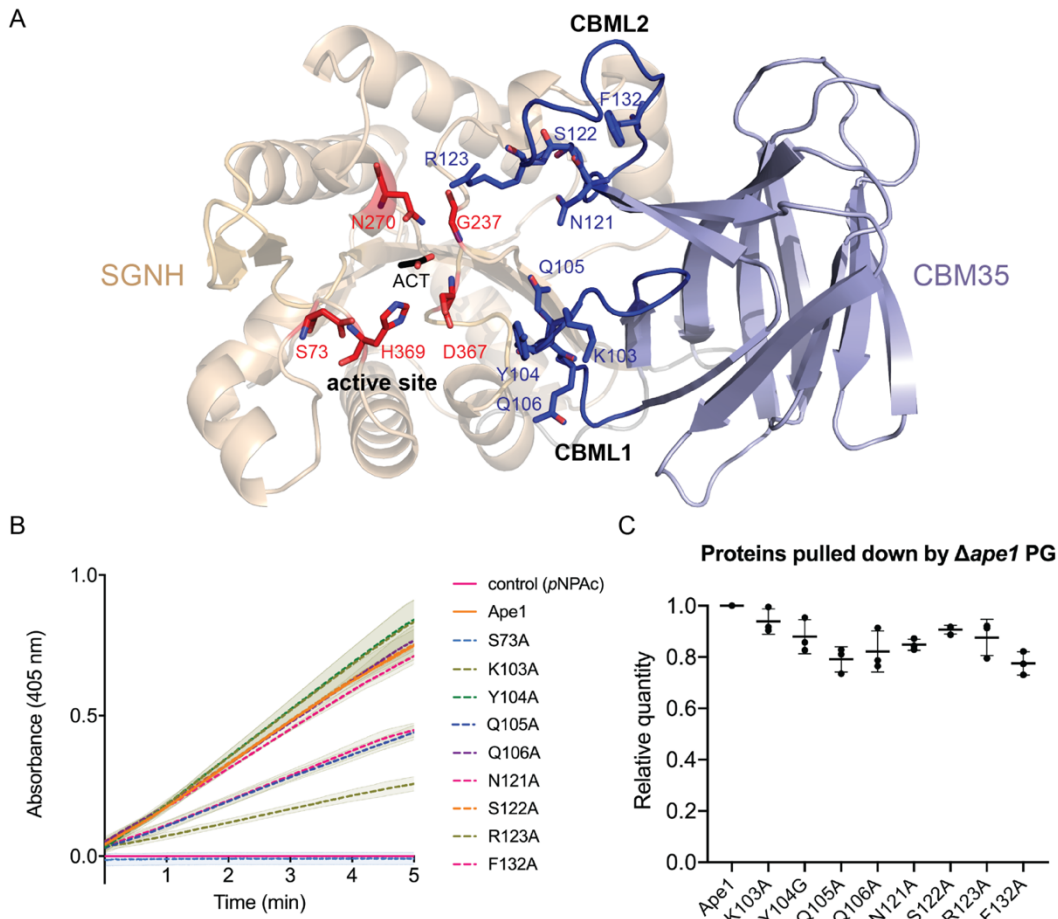


Figure 4-4. Assays of *O*-acetyl esterase activity and PG binding of CBM35 loop variants

(A) Residues predicted to be involved in catalysis of *O*-acetylated PG, shown in stick form. The catalytic triad and oxyanion hole are colored in red. CBM35 loops are colored in blue. (B) *O*-acetyl esterase activity of the *C. jejuni* Ape1 variants. Purified Ape1 and variants were incubated with *p*NPAc in 50 mM Na₂HPO₄/NaH₂PO₄, 50 mM NaCl, pH 6.5 at 25 °C for 5 min. The rate of *p*NP generation was monitored spectrophotometrically at 405 nm. Assays were performed in triplicate, mean data are plotted in lines, errors (within ± standard deviation) are shown as filled area. (C) Binding of CBM35 loop variants to Δ Ape1 PG. Wild-type and variant proteins were incubated with *C. jejuni* Δ Ape1 PG in 50 mM Na₂HPO₄/NaH₂PO₄, 50 mM NaCl, pH 6.5 at 4 °C for 20 min. Unbound proteins were washed with buffer and removed by centrifugation. Proteins pulled-down by PG were recovered using buffer and analyzed by SDS-PAGE. Band intensities were quantified using ImageJ. The relative quantity (%) was calculated as the amounts of pulled-down variants relative to pulled-down wild-type (set as 1). Assays were performed in triplicate, and data are shown as mean ± the standard deviation. Each dot reflects an individual experiment.

Table 4-3. O-acetyl esterase activity of CBM35 loop variants on pNPAc

Group	Enzyme	Specific activity ^a ($\mu\text{mol min}^{-1} \text{mg}^{-1}$)	Residual activity ^b (100%)
	Ape1 wild-type	33 ± 1	100
Nucleophile CBM35 Loop 1	S73A	0 ± 1	0
	K103A	36 ± 3	111
	Y104G	36 ± 3	113
	Q105A	19 ± 1	59
	Q106A	33 ± 2	102
CBM35 Loop 2	N121A	19 ± 1	60
	S122A	32 ± 2	101
	R123A	11 ± 1	34
	F132A	31 ± 1	95

^aEnzyme assay was measured at 25 °C in triplicate using 20 nM Ape1 enzyme and 2 mM pNPAc substrate in buffer (50 mM sodium phosphate, 50 mM NaCl, pH 6.5).

^bResidual activity is defined as the percentage of Ape1 wild-type activity.

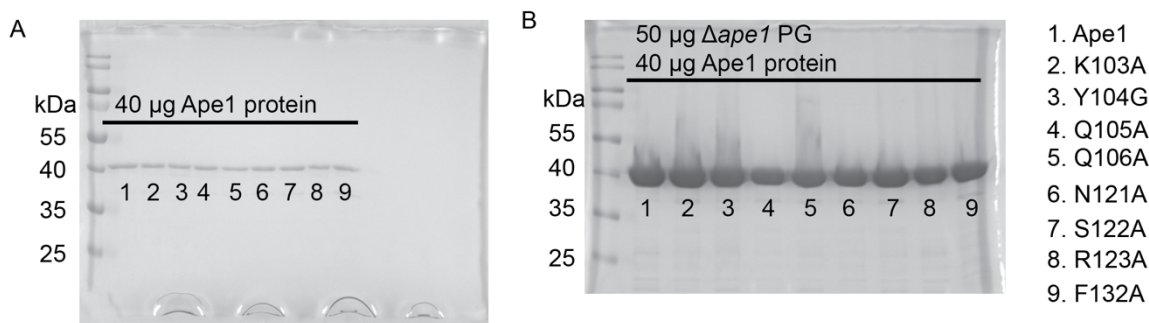


Figure 4-5. Δ ape1 PG pull-down assay

40 µg CjApe1 and variant proteins were incubated in the absence (A) or presence (B) of Δ ape1 PG in 250 µl buffer (50 mM sodium phosphate buffer, 50 mM NaCl, pH 6.5) at 4 °C for 20 min, followed by three times wash with 1 mL of buffer using centrifugation. The pellet was resuspended in 30 µl of 1× SDS dye (1% (w/v) β- mercaptoethanol, 0.02% (w/v) bromophenol blue, 30% (v/v) glycerol, 10% (w/v) SDS, 250 mM Tris pH6.8). 20 µl of the sample was ran on a 12% SDS-PAGE. The number labelled on each lane indicates the corresponding protein (shown as text in right side).

4.2.4 Ape1-PG binding mode by mechanism-guided HADDOCK docking

To obtain a plausible binding mode of CjApe1 to PG, docking experiments were performed using HADDOCK2.2 with active site restraints (184,189). The CjApe1 crystal structure and an ensemble of 10 *O*-acetyl PG conformers were used for docking. The *O*-acetyl PG model was prepared as a hexasaccharide to approximately match the length of the putative substrate binding groove (20- 30Å) on the CjApe1 protein surface. Considering ~10% of total *Δape1* PG is acetylated (54), only the second MurNAc residue in the hexasaccharide was acetylated. A total of six unambiguous distance restraints were applied for the CjApe1-PG complex to maintain catalytically reasonable distances between the catalytic triad, oxyanion hole and the acetyl group of the hexasaccharide (see methods for details).

Of the final 200 docking solutions, 188 were grouped into 7 clusters using a fraction of common contacts (FCC) cut-off of 0.79 (**Table 4-4**). All of the clusters showed a convergent binding mode with an RMSD < 2.5 Å to the model with the best HADDOCK score (lowest energy) (**Figure 4-6A**). Importantly, each cluster featured the *O*-acetyl glycan strand sitting along the interface of the SGNH and CBM35 domains (**Figure 4-7**). The main difference among the 7 clusters was the direction of *O*-acetyl hexasaccharide (**Figure 4-6B**), in which the reducing end of the hexasaccharide, containing the free hydroxyl group at carbon 1, is either close to the CBML1 loop (named as O1→O4) or close to the CBML2 loop (named as O4←O1) (**Figure 4-7**). 91% of the 188 solutions, including the best HADDOCK score, belongs to O1→O4; 9% of the 188 solutions were oriented as O4←O1. However, the direction preference cannot be discerned in the docking experiment. Repeating the docking experiment with another random set of simulated PG conformers resulted in the highest scoring model with the opposite glycan direction, suggesting the glycan orientation bound to Ape1 varies depending on the

input glycan conformers. Between the top docking solutions, only subtle changes were observed in the phi-psi angle of glycan strands. The phi-psi angle of the bound glycan strand is comparable to that of the starting backbone of glycan strand conformers, suggesting the binding pose maintains the low energy conformer state of the PG hexasaccharide.

The protein surface of a representative complex (**Figure 4-7**) is colored by the amino acid conservation derived from ConSurf analysis (194). The bound glycan strand runs the length of the putative substrate groove on the CjApe1 surface, and the *O*-acetylated MurNAc sits adjacent to the catalytic center of the enzyme. Each MurNAc O3 atom is exposed to the solvent, allowing the peptide stem to point away from Ape1 without steric clashes.

In the docked model, surface loops of CjApe1 are predicted to act like clamps that hold the glycan strand in place adjacent to the catalytic residues. Loops with residues less than 15 Å from the bound *O*-acetylated MurNAc include SGNHL1 (loop that connects β 2 and α 3), SGNHL2 loop (between β 16 and α 7) and the two CBM35 loops CBML1 and CBML2 (**Figure 4-7**). Loop SGNHL2 contains several conserved residues (K313, Y316 and K318), which may involve in Ape1 activity through an unidentified mechanism. Residues Q105, N121 and R123 of CBML1 and CBML2, in which mutations reduced catalytic activity, are within 15 Å from *O*-acetylated MurNAc.

Table 4-4. HADDOCK calculation statistics of CjApe1-PG complex

Docking experiment	CjApe1- <i>O</i> -acetylated PG						
AIR^a							
Ape1 active residues ^b	73,77,79,82,86,87,90,91,101,103,104,105,106,108,111,112,113,114,121,123,236,237,239,241,272,273,276,277,323,325,328,365,367,369,370,371,372,373,376,380						
Ape1 passive residues ^b	62,88,92,110,115,116,117,118,119,122,124,125,126,127,128,147,149,151,153,154,156,244,245,246,274,275,278,279,280,281,285,312,313,318,320,322,326,329,332,333,347,350,359,361,362,366,377,384,392						
<i>O</i> -acetylated PG active residues ^b							
<i>O</i> -acetylated PG passive residues ^b	1,2,3,4,5,6						
Cluster^c							
Cluster no.	Cluster 1	Cluster 2	Cluster 3	Cluster 4	Cluster 5	Cluster 6	Cluster 7
HADDOCK score	-69.2 ± 4.3	-57.2 ± 3.2	-50.9 ± 9.3	-60.0 ± 7.0	-45.8 ± 10	-50.7 ± 8.9	-54 ± 10.4
Average RMSD (Å) between structures in the cluster	0.5 ± 0.2	0.6 ± 0.2	0.4 ± 0.1	0.5 ± 0.2	0.4 ± 0.2	0.4 ± 0.2	0.3 ± 0.2
Number of structures in the cluster	113	36	11	11	6	6	5
Buried surface area (Å ²)	1346 ± 54	1316 ± 106	1281 ± 63	1393 ± 57	1292 ± 50	1327 ± 74	1296 ± 21
E _{intermolecular} (kcal/mol)	131 ± 68	148 ± 52	230 ± 72	162 ± 39	128 ± 44	200 ± 50	130 ± 63
E _{non-bonded} (kcal/mol)	-120 ± 22	-135 ± 21	-79 ± 16	-124 ± 20	-109 ± 24	-119 ± 11	-100 ± 11
Evan der Waals (kcal/mol)	-45 ± 4	-42 ± 4	-44 ± 5	-42 ± 3	-39 ± 8	-41 ± 4	-34 ± 4
Electrostatic (kcal/mol)	-75 ± 24	-93 ± 20	-35 ± 16	-82 ± 21	-71 ± 18	-79 ± 11	-66 ± 8
Eambiguous intermolecular restraints (kcal/mol)	251 ± 52	282 ± 47	309 ± 68	286 ± 29	237 ± 37	319 ± 54	230 ± 72
Number of AIR violations	6.1 ± 1.3	6.8 ± 1.3	7.3 ± 1.8	6.8 ± 0.9	5.8 ± 1.1	8.3 ± 1.4	5.4 ± 1.6

^aThe AIR residues were defined based on the binning interface predicted from CPoRT server using Ape1 structure and sequence as input information.

^bThe number for Ape1 corresponds to the amino acid number in the native sequence. The number 1, 3, 5 and 2, 4, 6 for corresponds to the residues GlcNAc and MurNAc, respectively. Residue 3 is *O*-acetylated MurNAc.

^cIn each cluster, the energetic statistics were calculated over the 10 structures with the best HADDOCK scores.

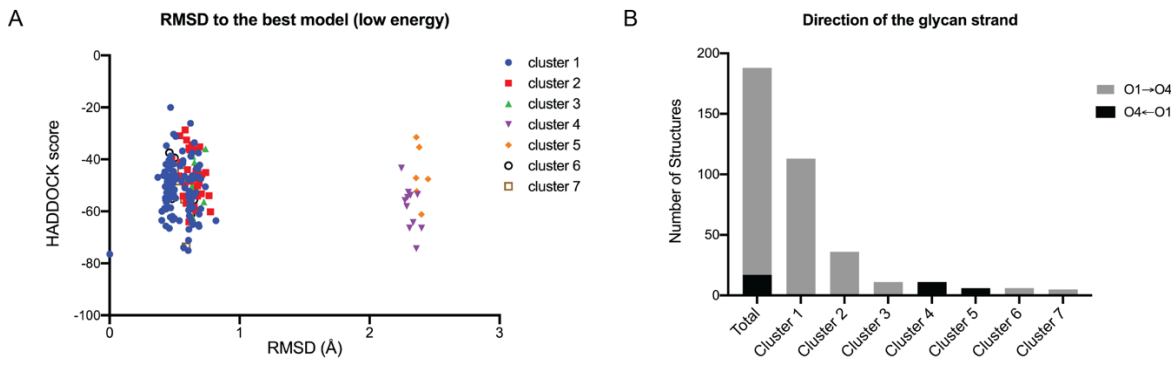


Figure 4-6. Seven clusters of Ape1-*O*-acetyl hexasaccharide docking models from HADDOCK

(A) The final 200 water-refined models are presented as HADDOCK score in the function of RMSD deviation from the best HADDOCK score model (lowest energy). Models with FCC higher than cut-off (FCC=0.79) are clustered and are shown in same color. (B) Clusters 4 and 5 which show large RMSD deviation from the best model contain the glycan strand position in the opposite direction of the best model.

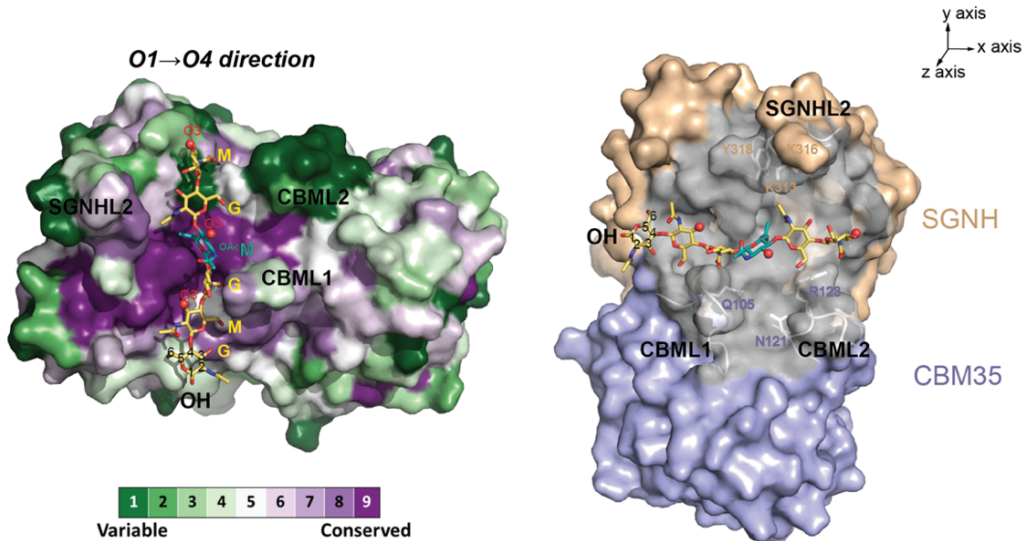


Figure 4-7. HADDOCK model of the CjApe1-*O*-acetyl hexasaccharide complex

The CjApe1-*O*-acetyl hexasaccharide model presents the best HADDOCK scoring solution in the docking experiment. Two views are rotated by 90° along z axis as to emphasize that the proximal loops form a clamp that holds a hexasaccharide. In the left panel, CjApe1 is shown in the surface representation colored by amino acid conservation. The *O*-acetyl hexasaccharide is shown in stick form and saccharide residues (MurNAc=M; GlcNAc=G; *O*-acetylated MurNAc=^{OAc}M) are labelled. MurNAc O3 atoms are highlighted as red spheres. In the right panel, residues that are within 15 Å to *O*-acetylated MurNAc are colored in grey, including SGNHL1, CBML1 and CBML2. The predicated functional residues in these loops are labelled.

Structural comparison of Ape1 homologs

To study whether the loops in the active site of CjApe1 determine substrate entry and binding, CjApe1 was compared to its structural homologs. From a search in the PDB database using Dali, the *N. meningitidis* (NmApe1; PDB ID: 4K7J) is the closest structural homolog of CjApe1, with an RMSD of 2.0 Å over 267 aligned C α positions. A carbohydrate esterase of the SGNH superfamily from *Clostridium thermocellum* (CtCE2; PDB ID: 2WAB) showed an RMSD of 2.7 Å over 98 aligned C α positions.

The concave surface that forms the active groove of the CjApe1 and NmApe1 are generally similar (**Figure 4-8A and Figure 4-8B**). Both CjApe1 and NmApe1 contain long SGNHL2 (17 amino acids) and short SGNHL1 loops (8 amino acids). CjApe1 and NmApe1 had the largest structural deviation at loop SGNHL2. In NmApe1, the SGNHL2 loop conformation is nearly 90 ° from of the equivalent position of this loop in CjApe1 (**Figure 4-9**). The difference in the conformation of this loop is likely caused by a disulfide bond between Cys316 and Cys352 observed in the NmApe1 structure (PDB ID: 4K7J). The cysteine residues are conserved in several bacteria but not in *C. jejuni* (**Figure 4-10**).

The surface of CtCE2 near the active site is significantly different as compared to CjApe1 and NmApe1. In CtCE2, the SGNHL2 loop is 6 residues long, which is 11 amino acids shorter than in CjApe1. Conversely, CtCE2 loop SGNHL1 is 4 amino acid longer than the equivalent loop in CjApe1 (**Figure 4-8A & Figure 4-8C**). The shorter SGNHL2 and longer SGNHL1 loops of CtCE2 restructure the substrate binding groove to be 90° from that in Ape1. The consequence of the altered loops is illustrated by the orientation of bound cellobiohexose to CtCE2 which is perpendicular in comparison to the glycan in the CjApe1 docking model. Collectively, we propose the orientation of substrate binding groove in Ape1 is divergent from

that of CtCE2 because of altered loop lengths in the active cleft. Such changes might indicate an adaptation to substrate specificity.

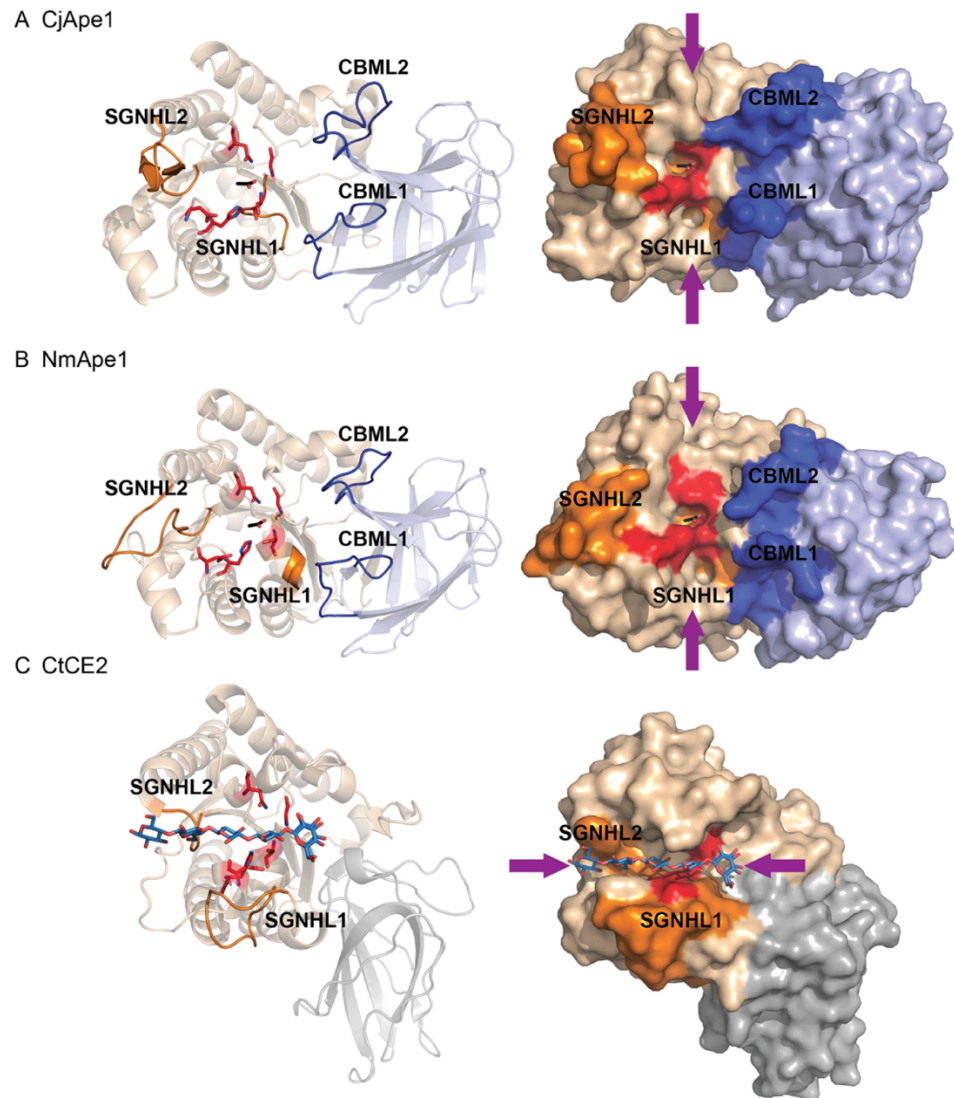


Figure 4-8. Comparison of proposed substrate binding orientations within the SGNH hydrolase superfamily

Structures of (A) CjApe1, (B) NmApe1 (PDB 4K7J) and (C) CtCE2 (PBD: 2WAB) are shown as cartoons (left) and surface representations (right). These structures are aligned based on the orientation of the SGNH domains. The orientation of glycan substrates bound in the active site grooves are indicated using purple arrows. Loops involved in determining the substrate orientation are highlighted (SGNHL1 and SGNHL2, orange; CBML1 and CBML2; blue). Conserved SGNH domain catalytic residues are shown in stick form and colored red.

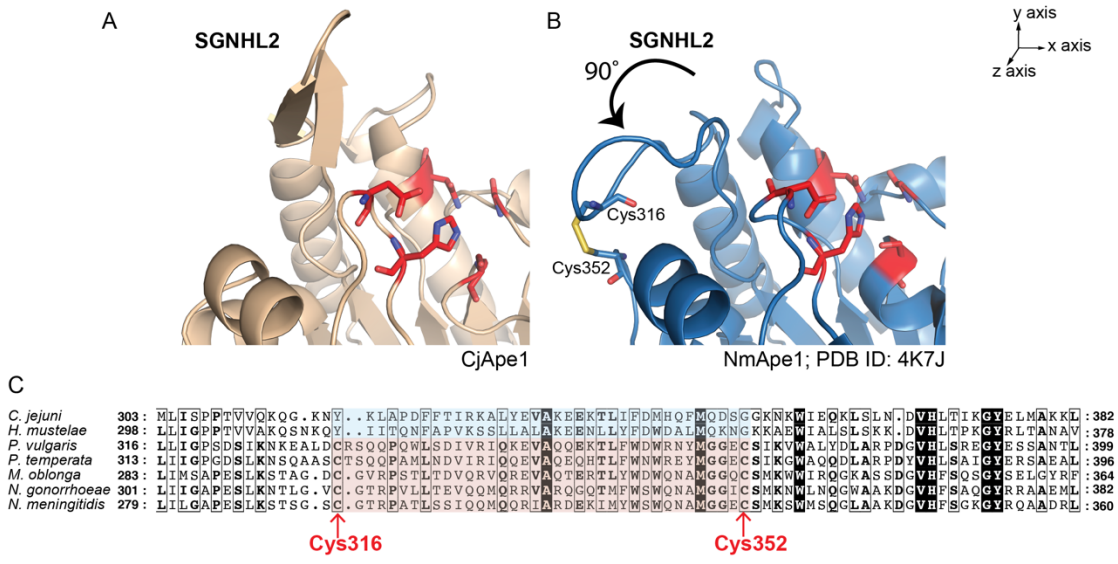


Figure 4-9. Structure of the SGNHL2 loop and sequence alignment

(A) Cartoon representation of the SGNHL2 loop from CjApe1. Conserved SGNH domain catalytic residues are shown as sticks and colored red. (B) NmApe1 (PDB 4K7J blue; 4K9S green). The SGNHL2 loop of CjApe1 is orientated 90° about the z-axis in comparison to the loops in the NmApe1 structure. Residues constituting the disulfide bond are shown in stick form (nitrogen, blue; oxygen, red; sulfur, yellow). (C) Sequence alignment of CjApe1 homologs performed in Clustal Omega and presented by ESPript. Highlighted in this partial alignment is the Cys-Cys bond of the SGNHL2 loop. Ape1 homologs: *Helicobacter mustelae* (WP_013022746.1); *Proteus vulgaris* (WP_185901317.1); *Photorhabdus temperata* (WP_023045068.1); *Moraxella oblonga* (WP_066805747.1); *Neisseria gonorrhoeae* (WP_003695451.1); *Neisseria meningitidis* (WP_049224741.1).

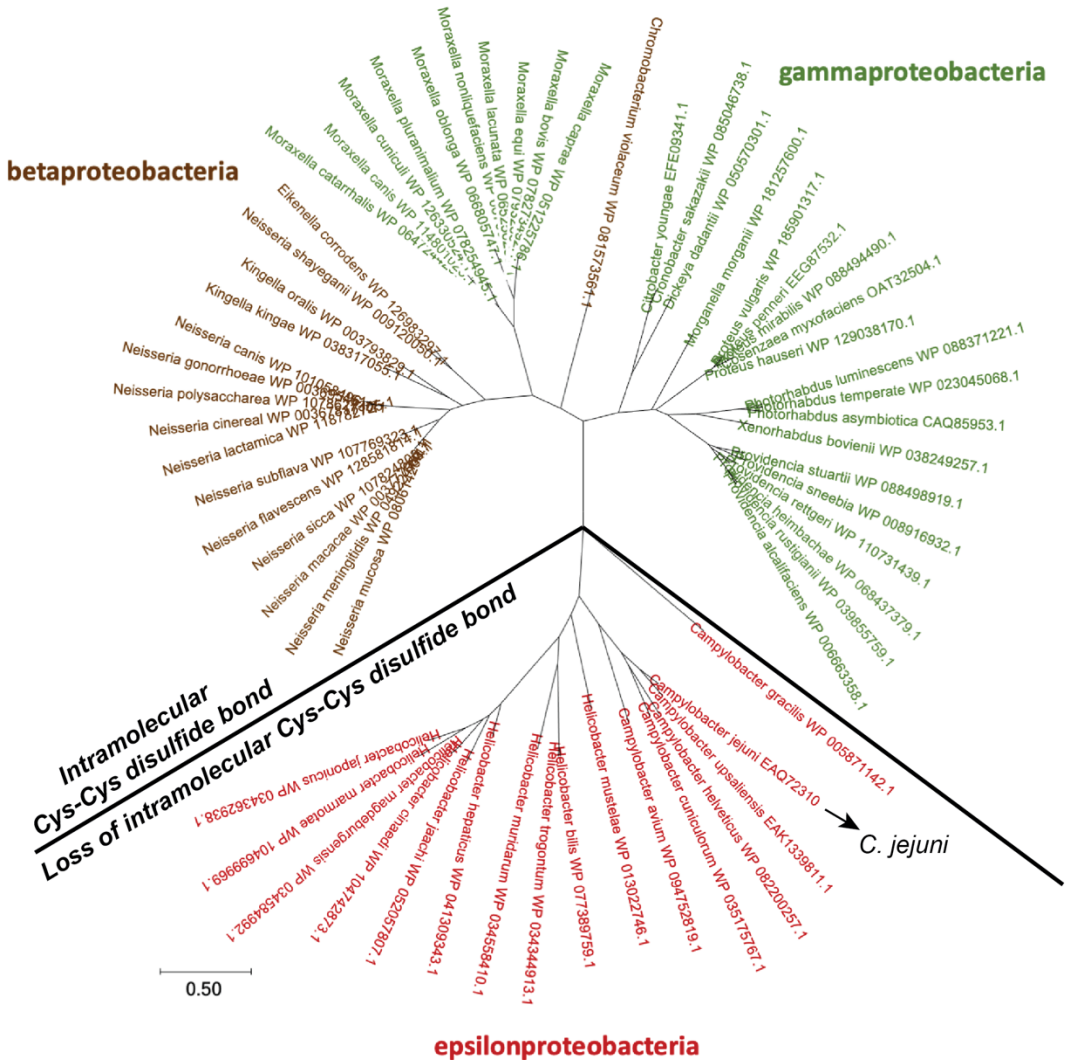


Figure 4-10. Ape1 phylogenetic tree showing the evolution of the intramolecular disulfide bond of loop SGNHL2

Ape1 homologous sequences (sequence identity: 25%–80%) were searched in UniRef90 database using ConSurf. Sequences showing \pm 20 of amino acids of the length of *C. jejuni* Ape1 (*CJJ81176_0638*) were manually removed. The final 61 sequences were aligned using MUSCLE alignment algorithm, and a maximum likelihood tree was constructed based the aligned sequences in MEGA X. Ape1 homologs in betaproteobacteria and gammaproteobacteria contains the intramolecular disulfide bond, whereas Ape1 homologs of epsilonproteobacteria (e.g., *Campylobacter* and *Helicobacter* species) evolved to loss this disulfide bond.

4.3 Discussion

CBM35 domains are proposed to bind sugars and assist in catalytic efficiency of glycoside hydrolases (165,211). The domain displays a jelly roll/β-sandwich fold with two conserved calcium ions binding sites. The first calcium ion is considered a structural site coordinated by conserved acidic residues. The second calcium ion is typically involved in sugar binding. The bound sugar is coordinated by the calcium ion and interacts with conserved residues such as stacking interactions with aromatic residues (Trp and Phe) (164,211,212) and charged interactions with arginine residues (164,165). The structure of CBM35 in CjApe1 diverges from CBM35 domains in other glycoside hydrolases. We did not observe bound metal ions nor the conserved amino acids for metal ion binding, consistent with the observation that EDTA treatment of *Neisseria gonorrhoeae* Ape1 did not inhibit Ape1 activity (162). The absence of metal binding is reflected in the low level of sequence identity of the Ape1 CBM35 and the CBM35 domains from other glycoside hydrolases.

We showed that the CjApe1 CBM35 has two big loops positioned near to the catalytic triad. The length of these loops is longer than the equivalent loops in other CBM35 domains suggesting that these long loops evolved for distinct biological function. The catalytic domain of SGNH hydrolase superfamily is characterized with a canonical α/β/α fold. Interestingly, The CjApe1 CBM35 domain is inserted between helix α2 and strand β14 in the α/β/α fold. This insertion places the big loops of the CBM35 domain in proximity to the active site. Our mutagenesis results confirmed that residues of the CjApe1 CBM35 domain are important for catalysis. The insertion of CBM35 domain might be an adaptation for CjApe1 for hydrolysis of the PG substrate.

The proposed CjApe1-PG binding model features a long putative substrate binding groove docked with a six-saccharide polymer. *C. jejuni* Δ *ape1* showed increased *O*-acetylated MurNAc linked to dipeptides, tripeptides, and tetrapeptides when compared to the wild-type strain (54), suggesting that muropeptide length has little effect on CjApe1 de-*O*-acetylase activity. Purified NmApe1 is active against various *O*-acetylated muropeptides *in vitro*, but deletion of *N. meningitidis* *ape1* displayed accumulated *O*-acetylated tripeptide levels, suggesting a preference for *O*-acetylated tripeptides in cell (213). However, the mechanism leading to a preference for tripeptide substrates in *N. meningitidis* is not known. Our Ape1-PG complex model suggested that the peptides are positioned away from the protein and do not form specific interactions. Ape1 is proposed to act as a prerequisite enzyme for LT to control glycan strand length in the cell (54,157,213). LTs cleave the glycosidic bond between MurNAc and GlcNAc, and catalyze the concomitant formation of a 1,6-anhydroMurNAc end. During PG turnover, CjApe1 might efficiently de-*O*-acetylate PG containing glycan strands that are longer than six saccharides and initiate LT activity for subsequent biological events.

A direct binding between Ape1 and LT was recently identified by gel filtration in *N. meningitidis*, revealing a 105 kDa complex from co-elution of NmApe1(40 kDa) and the LT LtgA (65 kDa) (214). The authors monitored NmApe1 *O*-acetyl esterase activity on *p*NPAc in the presence of LtgA, finding that maximal NmApe1 activity is dependent on the presence of LtgA. BLAST searches with LtgA in *C. jejuni* found Slt (CJJ81176_0859) shares 30% with LtgA, and the recombinant Slt was expressed as described (215). We did not observe a change in CjApe1 *O*-acetyl esterase activity in the presence of Slt (**Figure 4-11**). This suggests that the mechanisms of Ape1 in *C. jejuni* and *N. meningitidis* are distinct, possibly due to

requirements of helical shape maintenance in *C. jejuni* that are absent in spherical *N. meningitidis*.

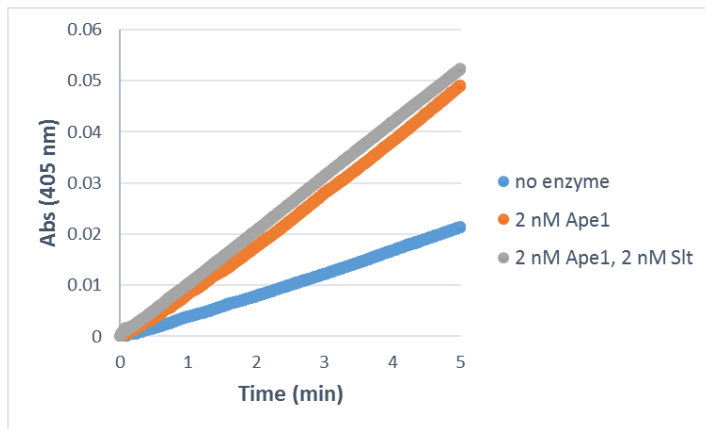


Figure 4-11. *O*-acetyl esterase activity of CjApe1 and Slt

CjApe1 *O*-acetyl esterase activity with 2 mM *p*NPAC in the presence and absence of equimolar Slt from *C. jejuni* in 50 mM sodium phosphate, 50 mM NaCl, pH 6.5.

The SGNHL2 loop of CjApe1 displayed distinct conformation from that of NmApe1. It is important to note that this disulfide bond in SGNHL2 is conserved among NmApe1 homologs from betaproteobacteria and gammaproteobacteria but is absent in epsilonproteobacteria (Figure 4-9 & Figure 4-10). In the CjApe1 and in other *Campylobacter* and *Helicobacter* species, both Cys residues are absent from the SGNHL2 loop. In *N. gonorrhoeae* Ape1 (NgApe1), titration of 5,5'-dithiobis-(2-nitrobenzoic acid) to quantify free thiolate groups indicated that ~65% of SGNHL2 Cys residues formed a disulfide bond (216). The dynamics of the Cys redox state of NgApe1 (and NmApe1) is hypothesized to regulate its activity. Upon the treatment of NgApe1 with thiol oxidizing reagent diamide, activity on *p*NPAC was reduced by 70%. Treatment of NgApe1 with the reducing agent glutathione also showed a 30% reduction in activity. Future work on exploring the function of the SGNHL2 loop on Ape1 activity on PG substrates would help to understand possible regulatory

mechanisms of Ape1 catalysis. Key residues for study by site-directed mutagenesis include introducing Cys residues at equivalent positions in CjApe1 and the substitutions at conserved positively charged residues of the SGNHL2 loop (**Figure 4-7**).

In our CjApe1-PG model, the binding interface consists of a positively charged groove in CjApe1 and the glycan saccharides of PG. A high throughput inhibitor screen using fluorogenic substrate 4-methylumbelliferyl acetate (MU-Ac) identified 7 potential NgApe1 inhibitors (216). These compounds feature phenyl rings and hydroxyl groups, which show similarity to the saccharide structure of PG. One of the inhibitors is purpurin ($K_i=4.8 \mu\text{M}$), an anthraquinone-based compound found in the roots of the plant *Rubia tinctorum*. Attempts to obtain a structure of the CjApe1-purpurin complex was performed by soaking and co-crystallization experiments. Crystals that were soaked with purpurin turned from clear to yellow in color, suggesting possible binding. Crystals of Ape1 were obtained from solution in the presence of inhibitor. However, these crystals showed poor diffraction to $\sim 6.5 \text{ \AA}$, possibly due to local conformational changes disrupting crystal packing upon purpurin binding.

CHAPTER 5: Concluding remarks

Helical shape is preserved in bacteria as a selective advantage for optimal growth in the environment. The helical shape of enteropathogenic *C. jejuni* is maintained in part by remodeling of PG structure through the enzymes Pgp2 and Ape1. This thesis examined the interaction between PG and these two enzymes, which increases our knowledge on PG selectivity by Pgp2 and Ape1. The current work informs a helical shape generation model resulting from local PG hydrolysis in *C. jejuni*.

5.1 Role of Pgp2 in helical shape generation

5.1.1 Overview

C. jejuni helical shape is determined by PG trimming by Pgp2 LD-carboxypeptidase activity. In Chapter 3, I demonstrate that the accessory NTF2 domain of Pgp2 is required for full Pgp2 activity and formation of the helical shape. A pocket within the NTF2 domain, ~40 Å away from the catalytic cleft, is formed by conserved residues (Y233, F242, K257, K307 and E324). This conserved pocket allows Pgp2 to bind PG tightly. Using NMR to define PG interaction interfaces of Pgp2, the catalytic cleft and the NTF2 pocket are identified as the two PG binding sites. Pgp2 likely forms a dimeric protein in the cell, thus up to four PG binding sites are present in the dimer. Based on these results, we propose Pgp2 may use two conserved PG binding sites to recognize PG tertiary structure to produce *C. jejuni* helical shape.

5.1.2 Future directions

The specific PG substructure recognized by the NTF2 domain has not been defined. To characterize the PG motif recognized by the NTF2 domain, we attempted to prepare

isotope-labeled PG fragments and a recombinant construct of the NTF2 domain alone for an NMR affinity experiment. Isotope-labeled PG can be prepared from bacteria cultured in M9 medium containing ¹³C-glucose and ¹⁵N-ammonium chloride as sole carbon and nitrogen sources (217). The NTF2 domain construct was prepared by removing the N-terminal residues consisting of the LD-CPase domain of Pgp2. Two recombinant NTF2 constructs containing residues 201–325 or 207–325 were expressed in *E. coli* as inclusion bodies, indicating these recombinant proteins were misfolded. Inspection of the Pgp2 structure shows that 11 buried hydrophobic residues (I211, L215, I274, N275, S277, P278, Y279, P280, R289, I308, Y310) become exposed in the recombinant NTF2 domain constructs. To obtain a soluble form of the NTF2 domain, future work can focus on point mutations of the buried residues to polar residues to increase hydrophilicity. Alternatively, solubility of the NTF2 domain may be improved by adding a solubility enhancement tag such as the MBP and GST proteins at the N-terminus (218).

We found that some NTF2 variants (K257A, K307A, and E324Q) greatly reduced enzyme activity on monomeric tetrapeptides compared to cross-linked tetrapeptides, implying Pgp2 selectively cleaves muropeptides in PG. The site of where Pgp2 trims peptides is likely important to understand how helical shape is achieved. A biophysical model suggests that helical cell shape could be generated by asymmetrical levels of cross-linking along one helical axis (209). The 4-3 cross-linkage catalyzed by DD-transpeptidase (DD-TPase) uses tetrapeptide as the acyl receptor. As Pgp2 trims tetrapeptides to tripeptides which would reduce available substrates for DD-TPase, localized Pgp2 activity could reduce cross-linking along one helical axis in the cell to generate the helical shape.

Pgp2 cellular localization can be visualized by microscopy using a HaloTag-Pgp2 fusion protein coupled to a fluorescent dye. The HaloTag is a 33 kDa modified haloalkane dehalogenase which irreversibly binds to a chloroalkane reactive linker (219). The linker is attached to different functional molecules, including a fluorescent dye that illuminates when excited by a specific wavelength. A commonly used dye TMR ligand is added externally to the growth media and the dye penetrates through the outer membrane to the periplasm of bacteria. We have successfully expressed a functional HaloTag-Pgp2 recombinant protein in *C. jejuni*. The localization of Halo-Pgp2 was visualized using TMR dye with a confocal microscope (Ziess LSM900). The preliminary results suggest Pgp2 is localized to regions within the cell. The next step is to quantify the fluorescent signal as the function of the Gaussian curvature over the *C. jejuni* cell. Examples of this quantification method are available for localization studies of CrvA (123) and CcmA (130). Briefly, Gaussian curvature of the *C. jejuni* cell is defined by principal component analysis of curvature parameters (helical radius and helical pitch) at points on the cell surface. Relative fluorescence intensity compared to the average intensity is calculated at each point. Analysis of the fluorescent signal in reference to the Gaussian curvature can define Pgp2 subcellular localization at the cell surface.

PG binding to the NTF2 domain may guide Pgp2 localization to regions of PG. Accessory PG binding domains such as the SPOR domain were shown to direct septum localization of cell division proteins (220). The SPOR domain recognizes PG without peptide stems (221). The NTF2 domain of Pgp2 may act by a similar mechanism, in which the NTF2 domain recognizes a specific PG substructure and guides spatial localization of Pgp2. Comparison of the localization of wild-type and NTF2 variants (Y233A, F242A, K257A,

K307A, E324Q) in *C. jejuni* or to purified PG sacculi by microscopy could address this question.

Defining the distribution of monomeric tetrapeptides in PG could be an alternative method to study Pgp2 localization. In the *C. jejuni* sacculus, the tetrapeptides present represent muropeptides protected from Pgp2 cleavage. Tetrapeptides can be detected *in vitro* using LD-transpeptidase (LD-TPase) and fluorescent D-amino acids (222). LD-TPase catalyzes labelling of tetrapeptides in two steps. First, LD-TPase performs nucleophilic attack to the carbonyl of third residue in a tetrapeptide (acyl donor), forming an acylenzyme intermediate; the free amino group of the fluorescent D-amino acid (acyl receptor) then attacks the intermediate, releasing LD-TPase and forming a fluorescent tetrapeptide. From our model for Pgp2 activity, I expect that monomeric tetrapeptides are enriched along one helical axis in the cell.

Pgp2 is likely an *N*-glycosylated protein. Up to three Pgp2 isoforms are observed on our Western blot (223) and in 2D-PAGE experiment by another group (195). Based on the *N*-glycosylation consensus sequon (N-X-S/T), we predicted four possible sites for *N*-linked glycosylation of Pgp2: ⁵³DKNIS⁵⁷, ⁶⁹LTNKT⁷³, ²⁷³DINIS²⁷⁷, ²⁸²LENET²⁸⁶. Among these sites, two sequences meet the consensus sequence (D/E-X1-N-X2-S/T, where X1, X2≠Proline) recognized by *C. jejuni* PglB *N*-oligosaccharyltransferase (224,225). The *N*-glycosylation site ⁵³DKNIS⁵⁷ has already been experimentally validated (226). Pgp2 was shown to bind to a soybean agglutinin affinity column specific for GalNAc residues (195). PglB transfers a heptasaccharide (GalNAc- α 1,4-GalNAc-[Glc β 1,3-]GalNAc- α 1,4-GalNAc- α 1,4-GalNAc- α 1,3-diBacNAc- β 1, where diBacNAc is 2,4-diacetamido-2,4,6-trideoxyglucopyranose) from a lipid carrier to over 50 proteins within the periplasm of *C. jejuni* (226). These results imply that Pgp2 is glycosylated by PglB.

The role of *N*-glycosylation in Pgp2 function is unclear. Many PG biosynthesis proteins are also *N*-glycosylated, including Pgp1 (Cj1345c), MreC (Cj0277), PatB (Cj0610c), Slt (Cj0843c), and the penicillin-binding proteins PbpA (Cj0508) and PbpC (Cj0652) (226). One hypothesis is that *N*-glycosylation contributes to protein stability in *C. jejuni* (227). Proteome analysis showed that $\Delta pgpB$ had accumulation of chaperons and proteases compared with wild-type, implying that misfolded proteins were produced with the loss of *N*-glycosylation. Interestingly, $\Delta pgpB$ demonstrated a straight shape, suggesting a potential link between *N*-glycosylation and cell shape maintenance (227). Assessment of Pgp2 stability and examination of the morphology restoration to $\Delta pgpB$ using variants within the predicted glycosylation sites would inform the mechanism of *N*-glycosylation in Pgp2 function and in helical shape generation.

5.2 Mechanism of Ape1 in cell wall turnover

5.2.1 Overview

Activity of the *O*-acetyl esterase Ape1 contributes to *C. jejuni* helical shape and pathogenesis. In Chapter 4, I present the structure of Ape1 and biochemical studies. The Ape1 structure consists of a catalytic SGNH hydrolase domain and a CBM35 domain. I investigated the function of the loops adjacent to the Ape1 active site. Two big loops, CBML1 and CBML2 of the CBM35 domain, are found to be required along with the conserved catalytic triad for catalysis. The length of loops SGNHL1 and SGNHL2 diverge from members of SGNH hydrolase family, which likely changes the orientation of the substrate binding groove in the active site. I propose that the putative Ape1 substrate binding groove can accommodate a hexasaccharide and infer that Ape1 may gain substrate specificity to control subsequent

biological events in the cell. The proposed model also suggests the PG peptide stems are not directly interacting with the active cleft, providing a guidance for the design of a mechanism-based inhibitor.

5.2.2 Future directions

Our Ape1-PG model implies that Ape1 activity is dependent on the length of PG strand. To test this hypothesis, PG substrates containing long and short glycan strands can be prepared by digesting whole Δ *ape1* PG with DL-endopeptidase (*P. aeruginosa* Tse1) (200), DD-endopeptidase (*P. aeruginosa* Tae2) (228) and muramidase, producing long PG strands with dipeptides, long PG strands with peptides, and a mixture of monomeric and crosslinked muropeptides, respectively. The rate of acetate released from these different PG fragments by Ape1 can be measured using an acetic acid assay kit (Megazyme). Our preliminary result showed that Ape1 cleaved more efficiently substrates containing long PG strands, consistent with the prediction from our structural study. Future work is needed to repeat the experiments and confirm the results.

The proposed Ape1-PG complex provides a direction to design a mechanism based Ape1 inhibitor. Previously, seven Ape1 inhibitors were found from a Canadian Compound Collection (216). These inhibitors vary in molecular mass and contain one phenyl ring and a hydroxyl group. The mechanism of Ape1 inhibition by these inhibitors is not known. Most of these inhibitors carry a very reactive electrophile. As these inhibitors are dissimilar to PG in structure, they may inhibit other enzymes. An inhibitor that mimics the PG substrate may be a more specific. This requires the knowledge of the PG motif required for binding to Ape1. The current complex model suggests that the saccharides of PG, but not the peptide stems, are

important for interacting with Ape1. We suggest the design of an Ape1 inhibitor should focus on mimicking the polysaccharide component of PG.

De-*O*-acetylation of PG by Ape1 is important for transglycosylase (LT) activity. Often multiple genes encoding LT enzymes are found in bacterial genomes. For example, Gram-negative *P. aeruginosa* has 11 LTs (229) and *H. pylori* has two non-redundant LT enzymes (230). Based on the site of cleavage, LTs are classified as either exo and endo. We found three LT homologs in *C. jejuni* strain 81-176, *slt* (*CJJ81176_0859*), *mltD* (*CJJ81176_0673*) and *rlpA* (*CJJ81176_0674*). The amino acid sequence of Slt has 31% identity to exo-lytic *H. pylori* Slt; MltD has 43% identity to endo-lytic *H. pylori* MltD; the RlpA has 54% identity to the catalytic domain of *P. aeruginosa* RlpA (231). Our Ape1-PG model suggests Ape1 favours hydrolysis of the *O*-acetylated MurNAc residue in the third or fourth position of a hexasaccharide, indicating the produced de-*O*-acetylated PG is suitable for endo-lytic cleavage by an LT enzyme. It will be informative to elucidate which *C. jejuni* LT enzyme is dependent on Ape1 activity to further understand the role of de-*O*-acetylation in regulating cell wall metabolism.

References

1. World Health Organization. (2015) WHO estimates of the global burden of foodborne diseases: foodborne disease burden epidemiology reference group 2007-2015.
2. Scallan, E., Hoekstra, R. M., Angulo, F. J., Tauxe, R. V., Widdowson, M. A., Roy, S. L., Jones, J. L., and Griffin, P. M. (2011) Foodborne illness acquired in the United States--major pathogens. *Emerg. Infect. Dis.* **17**, 7-15
3. EFSA. (2019) The European Union One Health 2018 Zoonoses Report. *EFSA Journal* **17(12):5926**
4. Thomas, M. K., Murray, R., Flockhart, L., Pintar, K., Pollari, F., Fazil, A., Nesbitt, A., and Marshall, B. (2013) Estimates of the burden of foodborne illness in Canada for 30 specified pathogens and unspecified agents, circa 2006. *Foodborne Pathog. Dis.* **10**, 639-648
5. Hald, T., Aspinall, W., Devleesschauwer, B., Cooke, R., Corrigan, T., Havelaar, A. H., Gibb, H. J., Torgerson, P. R., Kirk, M. D., Angulo, F. J., Lake, R. J., Speybroeck, N., and Hoffmann, S. (2016) World Health Organization Estimates of the Relative Contributions of Food to the Burden of Disease Due to Selected Foodborne Hazards: A Structured Expert Elicitation. *PLoS One* **11**, e0145839
6. Montgomery, M. P., Robertson, S., Koski, L., Salehi, E., Stevenson, L. M., Silver, R., Sundararaman, P., Singh, A., Joseph, L. A., Weisner, M. B., Brandt, E., Prarat, M., Bokanyi, R., Chen, J. C., Folster, J. P., Bennett, C. T., Francois Watkins, L. K., Aubert, R. D., Chu, A., Jackson, J., Blanton, J., Ginn, A., Ramadugu, K., Stanek, D., DeMent, J., Cui, J., Zhang, Y., Basler, C., Friedman, C. R., Geissler, A. L., Crowe, S. J., Dowell, N., Dixon, S., Whitlock, L., Williams, I., Jhung, M. A., Nichols, M. C., de Fijter, S., and Laughlin, M. E. (2018) Multidrug-Resistant *Campylobacter jejuni* Outbreak Linked to Puppy Exposure - United States, 2016-2018. *MMWR Morb. Mortal. Wkly. Rep.* **67**, 1032-1035
7. Kaakoush, N. O., Castano-Rodriguez, N., Mitchell, H. M., and Man, S. M. (2015) Global Epidemiology of *Campylobacter* Infection. *Clin. Microbiol. Rev.* **28**, 687-720
8. van den Berg, B., Bunschoten, C., van Doorn, P. A., and Jacobs, B. C. (2013) Mortality in Guillain-Barre syndrome. *Neurology* **80**, 1650-1654
9. Sejvar, J. J., Baughman, A. L., Wise, M., and Morgan, O. W. (2011) Population incidence of Guillain-Barre syndrome: a systematic review and meta-analysis. *Neuroepidemiology* **36**, 123-133
10. Moran, A. P., Annuk, H., and Prendergast, M. M. (2005) Antibodies induced by ganglioside-mimicking *Campylobacter jejuni* lipooligosaccharides recognise epitopes at the nodes of Ranvier. *J. Neuroimmunol.* **165**, 179-185
11. Buzby, J. C., Allos, B. M., and Roberts, T. (1997) The economic burden of *Campylobacter*-associated Guillain-Barre syndrome. *J. Infect. Dis.* **176 Suppl 2**, S192-197
12. Devleesschauwer, B., Bouwknegt, M., Mangen, M.-J., and Havelaar, A. (2017) Chapter 2 - Health and economic burden of *Campylobacter*. in *Campylobacter* (Klein, G. ed.), Academic Press. pp 27 - 40

13. Yang, Y., Feye, K. M., Shi, Z., Pavlidis, H. O., Kogut, M., A, J. A., and Ricke, S. C. (2019) A Historical Review on Antibiotic Resistance of Foodborne *Campylobacter*. *Front. Microbiol.* **10**, 1509
14. Casewell, M., Friis, C., Marco, E., McMullin, P., and Phillips, I. (2003) The European ban on growth-promoting antibiotics and emerging consequences for human and animal health. *J. Antimicrob. Chemother.* **52**, 159-161
15. Centner, T. J. (2016) Recent government regulations in the United States seek to ensure the effectiveness of antibiotics by limiting their agricultural use. *Environ. Int.* **94**, 1-7
16. Sears, A., Baker, M. G., Wilson, N., Marshall, J., Muellner, P., Campbell, D. M., Lake, R. J., and French, N. P. (2011) Marked campylobacteriosis decline after interventions aimed at poultry, New Zealand. *Emerg. Infect. Dis.* **17**, 1007-1015
17. Abd El-Hack, M. E., El-Saadony, M. T., Shehata, A. M., Arif, M., Paswan, V. K., Batiha, G. E., Khafaga, A. F., and Elbestawy, A. R. (2020) Approaches to prevent and control *Campylobacter* spp. colonization in broiler chickens: a review. *Environ. Sci. Pollut. Res. Int.*
18. Awad, W. A., Hess, C., and Hess, M. (2018) Re-thinking the chicken-*Campylobacter jejuni* interaction: a review. *Avian Pathol.* **47**, 352-363
19. Black, R. E., Levine, M. M., Clements, M. L., Hughes, T. P., and Blaser, M. J. (1988) Experimental *Campylobacter jejuni* infection in humans. *J. Infect. Dis.* **157**, 472-479
20. Robinson, D. A. (1981) Infective dose of *Campylobacter jejuni* in milk. *Br. Med. J. (Clin. Res. Ed)* **282**, 1584
21. Man, S. M. (2011) The clinical importance of emerging *Campylobacter* species. *Nat. Rev. Gastroenterol. Hepatol.* **8**, 669-685
22. Pead, P. J. (1979) Electron microscopy of *Campylobacter jejuni*. *J. Med. Microbiol.* **12**, 383-385
23. Doyle, M. P., and Roman, D. J. (1981) Growth and Survival of *Campylobacter fetus* subsp. *jejuni* as a Function of Temperature and pH. *J. Food Prot.* **44**, 596-601
24. Bolton, F. J., and Coates, D. (1983) A study of the oxygen and carbon dioxide requirements of thermophilic campylobacters. *J. Clin. Pathol.* **36**, 829-834
25. Shimada, K., and Tsuji, H. (1986) Enrichment for detection of *Campylobacter jejuni*. *J. Clin. Microbiol.* **23**, 887-890
26. Johansson, M. E., Phillipson, M., Petersson, J., Velcich, A., Holm, L., and Hansson, G. C. (2008) The inner of the two Muc2 mucin-dependent mucus layers in colon is devoid of bacteria. *Proc. Natl. Acad. Sci. U. S. A.* **105**, 15064-15069
27. Beery, J. T., Hugdahl, M. B., and Doyle, M. P. (1988) Colonization of gastrointestinal tracts of chicks by *Campylobacter jejuni*. *Appl Environ Microbiol* **54**, 2365-2370
28. Meade, K. G., Narciandi, F., Cahalane, S., Reiman, C., Allan, B., and O'Farrelly, C. (2009) Comparative in vivo infection models yield insights on early host immune response to *Campylobacter* in chickens. *Immunogenetics* **61**, 101-110
29. Stahl, M., Ries, J., Vermeulen, J., Yang, H., Sham, H. P., Crowley, S. M., Badayeva, Y., Turvey, S. E., Gaynor, E. C., Li, X., and Vallance, B. A. (2014) A novel mouse model of *Campylobacter jejuni* gastroenteritis reveals key pro-inflammatory and tissue protective roles for Toll-like receptor signaling during infection. *PLoS Pathog.* **10**, e1004264

30. Lee, A., O'Rourke, J. L., Barrington, P. J., and Trust, T. J. (1986) Mucus colonization as a determinant of pathogenicity in intestinal infection by *Campylobacter jejuni*: a mouse cecal model. *Infect Immun* **51**, 536-546
31. Inglis, G. D., Kalischuk, L. D., Busz, H. W., and Kastelic, J. P. (2005) Colonization of cattle intestines by *Campylobacter jejuni* and *Campylobacter lanienae*. *Appl Environ Microbiol* **71**, 5145-5153
32. Zheng, L., Kelly, C. J., and Colgan, S. P. (2015) Physiologic hypoxia and oxygen homeostasis in the healthy intestine. A Review in the Theme: Cellular Responses to Hypoxia. *Am. J. Physiol. Cell Physiol.* **309**, C350-360
33. Ferrero, R. L., and Lee, A. (1988) Motility of *Campylobacter jejuni* in a viscous environment: comparison with conventional rod-shaped bacteria. *J. Gen. Microbiol.* **134**, 53-59
34. Cohen, E. J., Nakane, D., Kabata, Y., Hendrixson, D. R., Nishizaka, T., and Beeby, M. (2020) *Campylobacter jejuni* motility integrates specialized cell shape, flagellar filament, and motor, to coordinate action of its opposed flagella. *PLoS Pathog.* **16**, e1008620
35. Szymanski, C. M., King, M., Haardt, M., and Armstrong, G. D. (1995) *Campylobacter jejuni* motility and invasion of Caco-2 cells. *Infect Immun* **63**, 4295-4300
36. Van Deun, K., Pasmans, F., Ducatelle, R., Flahou, B., Vissenberg, K., Martel, A., Van den Broeck, W., Van Immerseel, F., and Haesebrouck, F. (2008) Colonization strategy of *Campylobacter jejuni* results in persistent infection of the chicken gut. *Vet. Microbiol.* **130**, 285-297
37. Alemka, A., Clyne, M., Shanahan, F., Tompkins, T., Corcionivoschi, N., and Bourke, B. (2010) Probiotic colonization of the adherent mucus layer of HT29MTXE12 cells attenuates *Campylobacter jejuni* virulence properties. *Infect Immun* **78**, 2812-2822
38. Parkhill, J., Wren, B. W., Mungall, K., Ketley, J. M., Churcher, C., Basham, D., Chillingworth, T., Davies, R. M., Feltwell, T., Holroyd, S., Jagels, K., Karlyshev, A. V., Moule, S., Pallen, M. J., Penn, C. W., Quail, M. A., Rajandream, M. A., Rutherford, K. M., van Vliet, A. H., Whitehead, S., and Barrell, B. G. (2000) The genome sequence of the food-borne pathogen *Campylobacter jejuni* reveals hypervariable sequences. *Nature* **403**, 665-668
39. Stahl, M., Friis, L. M., Nothaft, H., Liu, X., Li, J., Szymanski, C. M., and Stintzi, A. (2011) L-fucose utilization provides *Campylobacter jejuni* with a competitive advantage. *Proc. Natl. Acad. Sci. U. S. A.* **108**, 7194-7199
40. Yamada, T., Hino, S., Iijima, H., Genda, T., Aoki, R., Nagata, R., Han, K. H., Hirota, M., Kinashi, Y., Oguchi, H., Suda, W., Furusawa, Y., Fujimura, Y., Kunisawa, J., Hattori, M., Fukushima, M., Morita, T., and Hase, K. (2019) Mucin O-glycans facilitate symbiosynthesis to maintain gut immune homeostasis. *EBioMedicine* **48**, 513-525
41. Hugdahl, M. B., Beery, J. T., and Doyle, M. P. (1988) Chemotactic behavior of *Campylobacter jejuni*. *Infect Immun* **56**, 1560-1566
42. Guccione, E., Leon-Kempis Mdel, R., Pearson, B. M., Hitchin, E., Mulholland, F., van Diemen, P. M., Stevens, M. P., and Kelly, D. J. (2008) Amino acid-dependent growth of *Campylobacter jejuni*: key roles for aspartase (AspA) under microaerobic

- and oxygen-limited conditions and identification of AspB (Cj0762), essential for growth on glutamate. *Mol. Microbiol.* **69**, 77-93
43. Leach, S., Harvey, P., and Wali, R. (1997) Changes with growth rate in the membrane lipid composition of and amino acid utilization by continuous cultures of *Campylobacter jejuni*. *J. Appl. Microbiol.* **82**, 631-640
44. Martinez, L. E., Hardcastle, J. M., Wang, J., Pincus, Z., Tsang, J., Hoover, T. R., Bansil, R., and Salama, N. R. (2016) *Helicobacter pylori* strains vary cell shape and flagellum number to maintain robust motility in viscous environments. *Mol. Microbiol.* **99**, 88-110
45. Constantino, M. A., Jabbarzadeh, M., Fu, H. C., and Bansil, R. (2016) Helical and rod-shaped bacteria swim in helical trajectories with little additional propulsion from helical shape. *Sci Adv* **2**, e1601661
46. Frirdich, E., Biboy, J., Adams, C., Lee, J., Ellermeier, J., Gieda, L. D., DiRita, V. J., Girardin, S. E., Vollmer, W., and Gaynor, E. C. (2012) Peptidoglycan-modifying enzyme Pgp1 is required for helical cell shape and pathogenicity traits in *Campylobacter jejuni*. *PLoS Pathog.* **8**, e1002602
47. Esson, D., Mather, A. E., Scanlan, E., Gupta, S., de Vries, S. P., Bailey, D., Harris, S. R., McKinley, T. J., Meric, G., Berry, S. K., Mastroeni, P., Sheppard, S. K., Christie, G., Thomson, N. R., Parkhill, J., Maskell, D. J., and Grant, A. J. (2016) Genomic variations leading to alterations in cell morphology of *Campylobacter* spp. *Sci. Rep.* **6**, 38303
48. Frirdich, E., Biboy, J., Huynh, S., Parker, C. T., Vollmer, W., and Gaynor, E. C. (2017) Morphology heterogeneity within a *Campylobacter jejuni* helical population: the use of calcofluor white to generate rod-shaped *C. jejuni* 81-176 clones and the genetic determinants responsible for differences in morphology within 11168 strains. *Mol. Microbiol.* **104**, 948-971
49. Frirdich, E., Vermeulen, J., Biboy, J., Soares, F., Taveirne, M. E., Johnson, J. G., DiRita, V. J., Girardin, S. E., Vollmer, W., and Gaynor, E. C. (2014) Peptidoglycan LD-carboxypeptidase Pgp2 influences *Campylobacter jejuni* helical cell shape and pathogenic properties and provides the substrate for the DL-carboxypeptidase Pgp1. *J. Biol. Chem.* **289**, 8007-8018
50. Min, K., An, D. R., Yoon, H. J., Rana, N., Park, J. S., Kim, J., Lee, M., Hesek, D., Ryu, S., Kim, B. M., Mobashery, S., Suh, S. W., and Lee, H. H. (2020) Peptidoglycan reshaping by a noncanonical peptidase for helical cell shape in *Campylobacter jejuni*. *Nat Commun* **11**, 458
51. Esson, D., Gupta, S., Bailey, D., Wigley, P., Wedley, A., Mather, A. E., Meric, G., Mastroeni, P., Sheppard, S. K., Thomson, N. R., Parkhill, J., Maskell, D. J., Christie, G., and Grant, A. J. (2017) Identification and initial characterisation of a protein involved in *Campylobacter jejuni* cell shape. *Microb. Pathog.* **104**, 202-211
52. Sycuro, L. K., Pincus, Z., Gutierrez, K. D., Biboy, J., Stern, C. A., Vollmer, W., and Salama, N. R. (2010) Peptidoglycan crosslinking relaxation promotes *Helicobacter pylori*'s helical shape and stomach colonization. *Cell* **141**, 822-833
53. Stahl, M., Frirdich, E., Vermeulen, J., Badayeva, Y., Li, X., Vallance, B. A., and Gaynor, E. C. (2016) The Helical Shape of *Campylobacter jejuni* Promotes In Vivo Pathogenesis by Aiding Transit through Intestinal Mucus and Colonization of Crypts. *Infect Immun* **84**, 3399-3407

54. Ha, R., Frirdich, E., Sychantha, D., Biboy, J., Taveirne, M. E., Johnson, J. G., DiRita, V. J., Vollmer, W., Clarke, A. J., and Gaynor, E. C. (2016) Accumulation of Peptidoglycan O-Acetylation Leads to Altered Cell Wall Biochemistry and Negatively Impacts Pathogenesis Factors of *Campylobacter jejuni*. *J. Biol. Chem.* **291**, 22686-22702
55. Shigematsu, M., Umeda, A., Fujimoto, S., and Amako, K. (1998) Spirochaete-like swimming mode of *Campylobacter jejuni* in a viscous environment. *J. Med. Microbiol.* **47**, 521-526
56. Sahin, O., Luo, N., Huang, S., and Zhang, Q. (2003) Effect of *Campylobacter*-specific maternal antibodies on *Campylobacter jejuni* colonization in young chickens. *Appl Environ Microbiol* **69**, 5372-5379
57. Zilbauer, M., Dorrell, N., Elmi, A., Lindley, K. J., Schuller, S., Jones, H. E., Klein, N. J., Nunez, G., Wren, B. W., and Bajaj-Elliott, M. (2007) A major role for intestinal epithelial nucleotide oligomerization domain 1 (NOD1) in eliciting host bactericidal immune responses to *Campylobacter jejuni*. *Cell. Microbiol.* **9**, 2404-2416
58. Sun, X., and Jobin, C. (2014) Nucleotide-binding oligomerization domain-containing protein 2 controls host response to *Campylobacter jejuni* in IL10^{-/-} mice. *J. Infect. Dis.* **210**, 1145-1154
59. Moreira, L. O., and Zamboni, D. S. (2012) NOD1 and NOD2 Signaling in Infection and Inflammation. *Front. Immunol.* **3**, 328
60. Frirdich, E., Biboy, J., Pryjma, M., Lee, J., Huynh, S., Parker, C. T., Girardin, S. E., Vollmer, W., and Gaynor, E. C. (2019) The *Campylobacter jejuni* helical to coccoid transition involves changes to peptidoglycan and the ability to elicit an immune response. *Mol. Microbiol.* **112**, 280-301
61. Hickey, T. E., Baqar, S., Bourgeois, A. L., Ewing, C. P., and Guerry, P. (1999) *Campylobacter jejuni*-stimulated secretion of interleukin-8 by INT407 cells. *Infect Immun* **67**, 88-93
62. Hickey, T. E., McVeigh, A. L., Scott, D. A., Michielutti, R. E., Bixby, A., Carroll, S. A., Bourgeois, A. L., and Guerry, P. (2000) *Campylobacter jejuni* cytolethal distending toxin mediates release of interleukin-8 from intestinal epithelial cells. *Infect Immun* **68**, 6535-6541
63. Braun, V., and Rehn, K. (1969) Chemical characterization, spatial distribution and function of a lipoprotein (murein-lipoprotein) of the *E. coli* cell wall. The specific effect of trypsin on the membrane structure. *Eur. J. Biochem.* **10**, 426-438
64. Braun, V. (1975) Covalent lipoprotein from the outer membrane of *Escherichia coli*. *Biochim Biophys Acta* **415**, 335-377
65. Cohen, E. J., Ferreira, J. L., Ladinsky, M. S., Beeby, M., and Hughes, K. T. (2017) Nanoscale-length control of the flagellar driveshaft requires hitting the tethered outer membrane. *Science* **356**, 197-200
66. Swoboda, J. G., Campbell, J., Meredith, T. C., and Walker, S. (2010) Wall teichoic acid function, biosynthesis, and inhibition. *ChemBioChem* **11**, 35-45
67. Vollmer, W., Blanot, D., and de Pedro, M. A. (2008) Peptidoglycan structure and architecture. *FEMS Microbiol. Rev.* **32**, 149-167
68. Lavollay, M., Fourgeaud, M., Herrmann, J. L., Dubost, L., Marie, A., Gutmann, L., Arthur, M., and Mainardi, J. L. (2011) The peptidoglycan of *Mycobacterium*

- abscessus* is predominantly cross-linked by L,D-transpeptidases. *J. Bacteriol.* **193**, 778-782
69. Peltier, J., Courtin, P., El Meouche, I., Lemee, L., Chapot-Chartier, M. P., and Pons, J. L. (2011) *Clostridium difficile* has an original peptidoglycan structure with a high level of N-acetylglucosamine deacetylation and mainly 3-3 cross-links. *J. Biol. Chem.* **286**, 29053-29062
 70. Barreteau, H., Kovac, A., Boniface, A., Sova, M., Gobec, S., and Blanot, D. (2008) Cytoplasmic steps of peptidoglycan biosynthesis. *FEMS Microbiol. Rev.* **32**, 168-207
 71. Radkov, A. D., and Moe, L. A. (2014) Bacterial synthesis of D-amino acids. *Applied microbiology and biotechnology* **98**, 5363-5374
 72. Bouhss, A., Trunkfield, A. E., Bugg, T. D., and Mengin-Lecreulx, D. (2008) The biosynthesis of peptidoglycan lipid-linked intermediates. *FEMS Microbiol. Rev.* **32**, 208-233
 73. Ruiz, N. (2015) Lipid Flippases for Bacterial Peptidoglycan Biosynthesis. *Lipid Insights* **8**, 21-31
 74. Sham, L. T., Butler, E. K., Lebar, M. D., Kahne, D., Bernhardt, T. G., and Ruiz, N. (2014) Bacterial cell wall. MurJ is the flippase of lipid-linked precursors for peptidoglycan biogenesis. *Science* **345**, 220-222
 75. Inoue, A., Murata, Y., Takahashi, H., Tsuji, N., Fujisaki, S., and Kato, J. (2008) Involvement of an essential gene, mviN, in murein synthesis in *Escherichia coli*. *J. Bacteriol.* **190**, 7298-7301
 76. Bolla, J. R., Sauer, J. B., Wu, D., Mehmood, S., Allison, T. M., and Robinson, C. V. (2018) Direct observation of the influence of cardiolipin and antibiotics on lipid II binding to MurJ. *Nat. Chem.* **10**, 363-371
 77. Mohammadi, T., van Dam, V., Sijbrandi, R., Vernet, T., Zapun, A., Bouhss, A., Diepeveen-de Bruin, M., Nguyen-Disteche, M., de Kruijff, B., and Breukink, E. (2011) Identification of FtsW as a transporter of lipid-linked cell wall precursors across the membrane. *EMBO J.* **30**, 1425-1432
 78. Taguchi, A., Welsh, M. A., Marmont, L. S., Lee, W., Sjodt, M., Kruse, A. C., Kahne, D., Bernhardt, T. G., and Walker, S. (2019) FtsW is a peptidoglycan polymerase that is functional only in complex with its cognate penicillin-binding protein. *Nat. Microbiol.* **4**, 587-594
 79. Welsh, M. A., Schaefer, K., Taguchi, A., Kahne, D., and Walker, S. (2019) Direction of Chain Growth and Substrate Preferences of Shape, Elongation, Division, and Sporulation-Family Peptidoglycan Glycosyltransferases. *J. Am. Chem. Soc.* **141**, 12994-12997
 80. Perlstein, D. L., Zhang, Y., Wang, T. S., Kahne, D. E., and Walker, S. (2007) The direction of glycan chain elongation by peptidoglycan glycosyltransferases. *J. Am. Chem. Soc.* **129**, 12674-12675
 81. Lovering, A. L., de Castro, L. H., Lim, D., and Strynadka, N. C. (2007) Structural insight into the transglycosylation step of bacterial cell-wall biosynthesis. *Science* **315**, 1402-1405
 82. Manat, G., Roure, S., Auger, R., Bouhss, A., Barreteau, H., Mengin-Lecreulx, D., and Touze, T. (2014) Deciphering the metabolism of undecaprenyl-phosphate: the bacterial cell-wall unit carrier at the membrane frontier. *Microb. Drug Resist.* **20**, 199-214

83. Workman, S. D., Worrall, L. J., and Strynadka, N. C. J. (2018) Crystal structure of an intramembranal phosphatase central to bacterial cell-wall peptidoglycan biosynthesis and lipid recycling. *Nat Commun* **9**, 1159
84. El Ghachi, M., Howe, N., Huang, C. Y., Olieric, V., Warshamanager, R., Touze, T., Weichert, D., Stansfeld, P. J., Wang, M., Kerff, F., and Caffrey, M. (2018) Crystal structure of undecaprenyl-pyrophosphate phosphatase and its role in peptidoglycan biosynthesis. *Nat Commun* **9**, 1078
85. Sauvage, E., Kerff, F., Terrak, M., Ayala, J. A., and Charlier, P. (2008) The penicillin-binding proteins: structure and role in peptidoglycan biosynthesis. *FEMS Microbiol. Rev.* **32**, 234-258
86. Meeske, A. J., Riley, E. P., Robins, W. P., Uehara, T., Mekalanos, J. J., Kahne, D., Walker, S., Kruse, A. C., Bernhardt, T. G., and Rudner, D. Z. (2016) SEDS proteins are a widespread family of bacterial cell wall polymerases. *Nature* **537**, 634-638
87. Blumberg, P. M., and Strominger, J. L. (1974) Interaction of penicillin with the bacterial cell: penicillin-binding proteins and penicillin-sensitive enzymes. *Bacteriol. Rev.* **38**, 291-335
88. Mainardi, J. L., Legrand, R., Arthur, M., Schoot, B., van Heijenoort, J., and Gutmann, L. (2000) Novel mechanism of beta-lactam resistance due to bypass of DD-transpeptidation in *Enterococcus faecium*. *J. Biol. Chem.* **275**, 16490-16496
89. Mainardi, J. L., Fourgeaud, M., Hugonnet, J. E., Dubost, L., Brouard, J. P., Ouazzani, J., Rice, L. B., Gutmann, L., and Arthur, M. (2005) A novel peptidoglycan cross-linking enzyme for a beta-lactam-resistant transpeptidation pathway. *J. Biol. Chem.* **280**, 38146-38152
90. Gupta, R., Lavollay, M., Mainardi, J. L., Arthur, M., Bishai, W. R., and Lamichhane, G. (2010) The *Mycobacterium tuberculosis* protein LdtMt2 is a nonclassical transpeptidase required for virulence and resistance to amoxicillin. *Nat. Med.* **16**, 466-469
91. Singh, S. K., SaiSree, L., Amrutha, R. N., and Reddy, M. (2012) Three redundant murein endopeptidases catalyse an essential cleavage step in peptidoglycan synthesis of *Escherichia coli* K12. *Mol. Microbiol.* **86**, 1036-1051
92. Heidrich, C., Templin, M. F., Ursinus, A., Merdanovic, M., Berger, J., Schwarz, H., de Pedro, M. A., and Holtje, J. V. (2001) Involvement of N-acetylmuramyl-L-alanine amidases in cell separation and antibiotic-induced autolysis of *Escherichia coli*. *Mol. Microbiol.* **41**, 167-178
93. Herlihey, F. A., and Clarke, A. J. (2017) Controlling Autolysis During Flagella Insertion in Gram-Negative Bacteria. *Adv Exp Med Biol* **925**, 41-56
94. Scheurwater, E. M., and Burrows, L. L. (2011) Maintaining network security: how macromolecular structures cross the peptidoglycan layer. *FEMS Microbiol. Lett.* **318**, 1-9
95. Vollmer, W., Joris, B., Charlier, P., and Foster, S. (2008) Bacterial peptidoglycan (murein) hydrolases. *FEMS Microbiol. Rev.* **32**, 259-286
96. Vermassen, A., Leroy, S., Talon, R., Provot, C., Popowska, M., and Desvaux, M. (2019) Cell Wall Hydrolases in Bacteria: Insight on the Diversity of Cell Wall Amidases, Glycosidases and Peptidases Toward Peptidoglycan. *Front. Microbiol.* **10**, 331

97. Do, T., Page, J. E., and Walker, S. (2020) Uncovering the activities, biological roles, and regulation of bacterial cell wall hydrolases and tailoring enzymes. *J. Biol. Chem.* **295**, 3347-3361
98. Yadav, A. K., Espaillat, A., and Cava, F. (2018) Bacterial Strategies to Preserve Cell Wall Integrity Against Environmental Threats. *Front. Microbiol.* **9**, 2064
99. Gilmore, M. E., Bandyopadhyay, D., Dean, A. M., Linnstaedt, S. D., and Popham, D. L. (2004) Production of muramic delta-lactam in *Bacillus subtilis* spore peptidoglycan. *J. Bacteriol.* **186**, 80-89
100. Bernard, E., Rolain, T., Courtin, P., Guillot, A., Langella, P., Hols, P., and Chapot-Chartier, M. P. (2011) Characterization of O-acetylation of N-acetylglucosamine: a novel structural variation of bacterial peptidoglycan. *J. Biol. Chem.* **286**, 23950-23958
101. Egan, A. J. F., Errington, J., and Vollmer, W. (2020) Regulation of peptidoglycan synthesis and remodelling. *Nat. Rev. Microbiol.* **18**, 446-460
102. Sanchez-Gorostiaga, A., Palacios, P., Martinez-Arteaga, R., Sanchez, M., Casanova, M., and Vicente, M. (2016) Life without Division: Physiology of *Escherichia coli* FtsZ-Deprived Filaments. *mBio* **7**(5), e01620-16
103. Margolin, W. (2009) Sculpting the bacterial cell. *Curr. Biol.* **19**, R812-822
104. Wachi, M., Doi, M., Tamaki, S., Park, W., Nakajima-Iijima, S., and Matsuhashi, M. (1987) Mutant isolation and molecular cloning of mre genes, which determine cell shape, sensitivity to mecillinam, and amount of penicillin-binding proteins in *Escherichia coli*. *J. Bacteriol.* **169**, 4935-4940
105. Kruse, T., Bork-Jensen, J., and Gerdes, K. (2005) The morphogenetic MreBCD proteins of *Escherichia coli* form an essential membrane-bound complex. *Mol. Microbiol.* **55**, 78-89
106. Jones, L. J., Carballido-Lopez, R., and Errington, J. (2001) Control of cell shape in bacteria: helical, actin-like filaments in *Bacillus subtilis*. *Cell* **104**, 913-922
107. Kawai, Y., Asai, K., and Errington, J. (2009) Partial functional redundancy of MreB isoforms, MreB, Mbl and MreBH, in cell morphogenesis of *Bacillus subtilis*. *Mol. Microbiol.* **73**, 719-731
108. van den Ent, F., Amos, L. A., and Lowe, J. (2001) Prokaryotic origin of the actin cytoskeleton. *Nature* **413**, 39-44
109. Salje, J., van den Ent, F., de Boer, P., and Lowe, J. (2011) Direct membrane binding by bacterial actin MreB. *Mol. Cell* **43**, 478-487
110. van den Ent, F., Izore, T., Bharat, T. A., Johnson, C. M., and Lowe, J. (2014) Bacterial actin MreB forms antiparallel double filaments. *Elife* **3**, e02634
111. Popp, D., Narita, A., Maeda, K., Fujisawa, T., Ghoshdastider, U., Iwasa, M., Maeda, Y., and Robinson, R. C. (2010) Filament structure, organization, and dynamics in MreB sheets. *J. Biol. Chem.* **285**, 15858-15865
112. Garner, E. C., Bernard, R., Wang, W., Zhuang, X., Rudner, D. Z., and Mitchison, T. (2011) Coupled, circumferential motions of the cell wall synthesis machinery and MreB filaments in *B. subtilis*. *Science* **333**, 222-225
113. Dominguez-Escobar, J., Chastanet, A., Crevenna, A. H., Fromion, V., Wedlich-Soldner, R., and Carballido-Lopez, R. (2011) Processive movement of MreB-associated cell wall biosynthetic complexes in bacteria. *Science* **333**, 225-228

114. Errington, J., and Wu, L. J. (2017) Cell Cycle Machinery in *Bacillus subtilis*. *Subcell Biochem.* **84**, 67-101
115. Daniel, R. A., and Errington, J. (2003) Control of cell morphogenesis in bacteria: two distinct ways to make a rod-shaped cell. *Cell* **113**, 767-776
116. Tiyanont, K., Doan, T., Lazarus, M. B., Fang, X., Rudner, D. Z., and Walker, S. (2006) Imaging peptidoglycan biosynthesis in *Bacillus subtilis* with fluorescent antibiotics. *Proc. Natl. Acad. Sci. U. S. A.* **103**, 11033-11038
117. Figge, R. M., Divakaruni, A. V., and Gober, J. W. (2004) MreB, the cell shape-determining bacterial actin homologue, co-ordinates cell wall morphogenesis in *Caulobacter crescentus*. *Mol. Microbiol.* **51**, 1321-1332
118. Ausmees, N., Kuhn, J. R., and Jacobs-Wagner, C. (2003) The bacterial cytoskeleton: an intermediate filament-like function in cell shape. *Cell* **115**, 705-713
119. Charbon, G., Cabeen, M. T., and Jacobs-Wagner, C. (2009) Bacterial intermediate filaments: in vivo assembly, organization, and dynamics of crescentin. *Genes Dev* **23**, 1131-1144
120. Cabeen, M. T., Charbon, G., Vollmer, W., Born, P., Ausmees, N., Weibel, D. B., and Jacobs-Wagner, C. (2009) Bacterial cell curvature through mechanical control of cell growth. *EMBO J.* **28**, 1208-1219
121. Cabeen, M. T., Murolo, M. A., Briegel, A., Bui, N. K., Vollmer, W., Ausmees, N., Jensen, G. J., and Jacobs-Wagner, C. (2010) Mutations in the Lipopolysaccharide biosynthesis pathway interfere with crescentin-mediated cell curvature in *Caulobacter crescentus*. *J. Bacteriol.* **192**, 3368-3378
122. Ingerson-Mahar, M., Briegel, A., Werner, J. N., Jensen, G. J., and Gitai, Z. (2010) The metabolic enzyme CTP synthase forms cytoskeletal filaments. *Nat. Cell Biol.* **12**, 739-746
123. Bartlett, T. M., Bratton, B. P., Duvshani, A., Miguel, A., Sheng, Y., Martin, N. R., Nguyen, J. P., Persat, A., Desmarais, S. M., VanNieuwenhze, M. S., Huang, K. C., Zhu, J., Shaevitz, J. W., and Gitai, Z. (2017) A Periplasmic Polymer Curves *Vibrio cholerae* and Promotes Pathogenesis. *Cell* **168**, 172-185 e115
124. Fernandez, N. L., Hsueh, B. Y., Nhu, N. T. Q., Franklin, J. L., Dufour, Y. S., and Waters, C. M. (2020) *Vibrio cholerae* adapts to sessile and motile lifestyles by cyclic di-GMP regulation of cell shape. *Proc. Natl. Acad. Sci. U. S. A.* **117**, 29046-29054
125. Martin, N. R., Blackman, E., Bratton, B. P., Bartlett, T. M., and Gitai, Z. (2020) The evolution of bacterial shape complexity by a curvature-inducing module. *bioRxiv*, 2020.02.20.954503
126. Sycuro, L. K., Wyckoff, T. J., Biboy, J., Born, P., Pincus, Z., Vollmer, W., and Salama, N. R. (2012) Multiple peptidoglycan modification networks modulate *Helicobacter pylori*'s cell shape, motility, and colonization potential. *PLoS Pathog.* **8**, e1002603
127. Sycuro, L. K., Rule, C. S., Petersen, T. W., Wyckoff, T. J., Sessler, T., Nagarkar, D. B., Khalid, F., Pincus, Z., Biboy, J., Vollmer, W., and Salama, N. R. (2013) Flow cytometry-based enrichment for cell shape mutants identifies multiple genes that influence *Helicobacter pylori* morphology. *Mol. Microbiol.* **90**, 869-883
128. Yang, D. C., Blair, K. M., Taylor, J. A., Petersen, T. W., Sessler, T., Tull, C. M., Leverich, C. K., Collar, A. L., Wyckoff, T. J., Biboy, J., Vollmer, W., and Salama, N.

- R. (2019) A Genome-Wide *Helicobacter pylori* Morphology Screen Uncovers a Membrane-Spanning Helical Cell Shape Complex. *J. Bacteriol.* **201**
129. Bonis, M., Ecobichon, C., Guadagnini, S., Prevost, M. C., and Boneca, I. G. (2010) A M23B family metallopeptidase of *Helicobacter pylori* required for cell shape, pole formation and virulence. *Mol. Microbiol.* **78**, 809-819
130. Taylor, J. A., Bratton, B. P., Sichel, S. R., Blair, K. M., Jacobs, H. M., DeMeester, K. E., Kuru, E., Gray, J., Biboy, J., VanNieuwenhze, M. S., Vollmer, W., Grimes, C. L., Shaevitz, J. W., and Salama, N. R. (2020) Distinct cytoskeletal proteins define zones of enhanced cell wall synthesis in *Helicobacter pylori*. *Elife* **9**
131. Shi, H., Bratton, B. P., Gitai, Z., and Huang, K. C. (2018) How to Build a Bacterial Cell: MreB as the Foreman of *E. coli* Construction. *Cell* **172**, 1294-1305
132. An, D. R., Im, H. N., Jang, J. Y., Kim, H. S., Kim, J., Yoon, H. J., Hesek, D., Lee, M., Mobashery, S., Kim, S. J., and Suh, S. W. (2016) Structural Basis of the Heterodimer Formation between Cell Shape-Determining Proteins Csd1 and Csd2 from *Helicobacter pylori*. *PLoS One* **11**, e0164243
133. Blair, K. M., Mears, K. S., Taylor, J. A., Fero, J., Jones, L. A., Gafken, P. R., Whitney, J. C., and Salama, N. R. (2018) The *Helicobacter pylori* cell shape promoting protein Csd5 interacts with the cell wall, MurF, and the bacterial cytoskeleton. *Mol. Microbiol.* **110**, 114-127
134. An, D. R., Kim, H. S., Kim, J., Im, H. N., Yoon, H. J., Yoon, J. Y., Jang, J. Y., Hesek, D., Lee, M., Mobashery, S., Kim, S. J., Lee, B. I., and Suh, S. W. (2015) Structure of Csd3 from *Helicobacter pylori*, a cell shape-determining metallopeptidase. *Acta Crystallogr. D Biol. Crystallogr.* **71**, 675-686
135. Chan, A. C., Blair, K. M., Liu, Y., Frirdich, E., Gaynor, E. C., Tanner, M. E., Salama, N. R., and Murphy, M. E. (2015) Helical shape of *Helicobacter pylori* requires an atypical glutamine as a zinc ligand in the carboxypeptidase Csd4. *J. Biol. Chem.* **290**, 3622-3638
136. Kim, H. S., Kim, J., Im, H. N., An, D. R., Lee, M., Hesek, D., Mobashery, S., Kim, J. Y., Cho, K., Yoon, H. J., Han, B. W., Lee, B. I., and Suh, S. W. (2014) Structural basis for the recognition of muramyltripeptide by *Helicobacter pylori* Csd4, a D,L-carboxypeptidase controlling the helical cell shape. *Acta Crystallogr. D Biol. Crystallogr.* **70**, 2800-2812
137. Kim, H. S., Im, H. N., An, D. R., Yoon, J. Y., Jang, J. Y., Mobashery, S., Hesek, D., Lee, M., Yoo, J., Cui, M., Choi, S., Kim, C., Lee, N. K., Kim, S. J., Kim, J. Y., Bang, G., Han, B. W., Lee, B. I., Yoon, H. J., and Suh, S. W. (2015) The Cell Shape-determining Csd6 Protein from *Helicobacter pylori* Constitutes a New Family of L,D-Carboxypeptidase. *J. Biol. Chem.* **290**, 25103-25117
138. Gunther, N. W. t., Bono, J. L., and Needleman, D. S. (2015) Complete Genome Sequence of *Campylobacter jejuni* RM1285, a Rod-Shaped Morphological Variant. *Genome Announc* **3**
139. Bochtler, M., Odintsov, S. G., Marcyjaniak, M., and Sabala, I. (2004) Similar active sites in lysostaphins and D-Ala-D-Ala metallopeptidases. *Protein Sci.* **13**, 854-861
140. Grabowska, M., Jagielska, E., Czapinska, H., Bochtler, M., and Sabala, I. (2015) High resolution structure of an M23 peptidase with a substrate analogue. *Sci. Rep.* **5**, 14833

141. Peters, N. T., Morlot, C., Yang, D. C., Uehara, T., Vernet, T., and Bernhardt, T. G. (2013) Structure-function analysis of the LytM domain of EnvC, an activator of cell wall remodelling at the *Escherichia coli* division site. *Mol. Microbiol.* **89**, 690-701
142. Uehara, T., Dinh, T., and Bernhardt, T. G. (2009) LytM-domain factors are required for daughter cell separation and rapid ampicillin-induced lysis in *Escherichia coli*. *J. Bacteriol.* **191**, 5094-5107
143. Lim, D., and Strynadka, N. C. (2002) Structural basis for the beta lactam resistance of PBP2a from methicillin-resistant *Staphylococcus aureus*. *Nat. Struct. Biol.* **9**, 870-876
144. Eberhardt, R. Y., Chang, Y., Bateman, A., Murzin, A. G., Axelrod, H. L., Hwang, W. C., and Aravind, L. (2013) Filling out the structural map of the NTF2-like superfamily. *BMC Bioinformatics* **14**, 327
145. Asakura, H., Churin, Y., Bauer, B., Boettcher, J. P., Bartfeld, S., Hashii, N., Kawasaki, N., Mollenkopf, H. J., Jungblut, P. R., Brinkmann, V., and Meyer, T. F. (2010) *Helicobacter pylori* HP0518 affects flagellin glycosylation to alter bacterial motility. *Mol. Microbiol.* **78**, 1130-1144
146. Bera, A., Biswas, R., Herbert, S., and Gotz, F. (2006) The presence of peptidoglycan O-acetyltransferase in various staphylococcal species correlates with lysozyme resistance and pathogenicity. *Infect Immun* **74**, 4598-4604
147. Hebert, L., Courtin, P., Torelli, R., Sanguinetti, M., Chapot-Chartier, M. P., Auffray, Y., and Benachour, A. (2007) *Enterococcus faecalis* constitutes an unusual bacterial model in lysozyme resistance. *Infect Immun* **75**, 5390-5398
148. Aubry, C., Goulard, C., Nahori, M. A., Cayet, N., Decalf, J., Sachse, M., Boneca, I. G., Cossart, P., and Dussurget, O. (2011) OatA, a peptidoglycan O-acetyltransferase involved in *Listeria monocytogenes* immune escape, is critical for virulence. *J. Infect. Dis.* **204**, 731-740
149. Rosenthal, R. S., Blundell, J. K., and Perkins, H. R. (1982) Strain-related differences in lysozyme sensitivity and extent of O-acetylation of gonococcal peptidoglycan. *Infect Immun* **37**, 826-829
150. Weadge, J. T., Pfeffer, J. M., and Clarke, A. J. (2005) Identification of a new family of enzymes with potential O-acetylpeptidoglycan esterase activity in both Gram-positive and Gram-negative bacteria. *BMC Microbiol.* **5**, 49
151. Bera, A., Herbert, S., Jakob, A., Vollmer, W., and Gotz, F. (2005) Why are pathogenic staphylococci so lysozyme resistant? The peptidoglycan O-acetyltransferase OatA is the major determinant for lysozyme resistance of *Staphylococcus aureus*. *Mol. Microbiol.* **55**, 778-787
152. Sychantha, D., Jones, C. S., Little, D. J., Moynihan, P. J., Robinson, H., Galley, N. F., Roper, D. I., Dowson, C. G., Howell, P. L., and Clarke, A. J. (2017) In vitro characterization of the antivirulence target of Gram-positive pathogens, peptidoglycan O-acetyltransferase A (OatA). *PLoS Pathog.* **13**, e1006667
153. Dillard, J. P., and Hackett, K. T. (2005) Mutations affecting peptidoglycan acetylation in *Neisseria gonorrhoeae* and *Neisseria meningitidis*. *Infect Immun* **73**, 5697-5705
154. Moynihan, P. J., and Clarke, A. J. (2010) O-acetylation of peptidoglycan in gram-negative bacteria: identification and characterization of peptidoglycan O-acetyltransferase in *Neisseria gonorrhoeae*. *J. Biol. Chem.* **285**, 13264-13273

155. Moynihan, P. J., and Clarke, A. J. (2014) Substrate specificity and kinetic characterization of peptidoglycan O-acetyltransferase B from *Neisseria gonorrhoeae*. *J. Biol. Chem.* **289**, 16748-16760
156. Weadge, J. T., and Clarke, A. J. (2006) Identification and characterization of O-acetylpeptidoglycan esterase: a novel enzyme discovered in *Neisseria gonorrhoeae*. *Biochemistry* **45**, 839-851
157. Moynihan, P. J., and Clarke, A. J. (2011) O-Acetylated peptidoglycan: controlling the activity of bacterial autolysins and lytic enzymes of innate immune systems. *Int. J. Biochem. Cell Biol.* **43**, 1655-1659
158. Blackburn, N. T., and Clarke, A. J. (2002) Characterization of soluble and membrane-bound family 3 lytic transglycosylases from *Pseudomonas aeruginosa*. *Biochemistry* **41**, 1001-1013
159. Akoh, C. C., Lee, G. C., Liaw, Y. C., Huang, T. H., and Shaw, J. F. (2004) GDSL family of serine esterases/lipases. *Prog. Lipid Res.* **43**, 534-552
160. Molgaard, A., Kauppinen, S., and Larsen, S. (2000) Rhamnogalacturonan acetylesterase elucidates the structure and function of a new family of hydrolases. *Structure* **8**, 373-383
161. Pfeffer, J. M., Weadge, J. T., and Clarke, A. J. (2013) Mechanism of action of *Neisseria gonorrhoeae* O-acetylpeptidoglycan esterase, an SGNH serine esterase. *J. Biol. Chem.* **288**, 2605-2613
162. Weadge, J. T., and Clarke, A. J. (2007) *Neisseria gonorrhoeae* O-acetylpeptidoglycan esterase, a serine esterase with a Ser-His-Asp catalytic triad. *Biochemistry* **46**, 4932-4941
163. Williams, A. H., Veyrier, F. J., Bonis, M., Michaud, Y., Raynal, B., Taha, M. K., White, S. W., Haouz, A., and Boneca, I. G. (2014) Visualization of a substrate-induced productive conformation of the catalytic triad of the *Neisseria meningitidis* peptidoglycan O-acetylersterase reveals mechanistic conservation in SGNH esterase family members. *Acta Crystallogr. D Biol. Crystallogr.* **70**, 2631-2639
164. Montanier, C., van Bueren, A. L., Dumon, C., Flint, J. E., Correia, M. A., Prates, J. A., Firbank, S. J., Lewis, R. J., Grondin, G. G., Ghinet, M. G., Gloster, T. M., Herve, C., Knox, J. P., Talbot, B. G., Turkenburg, J. P., Kerovuo, J., Brzezinski, R., Fontes, C. M., Davies, G. J., Boraston, A. B., and Gilbert, H. J. (2009) Evidence that family 35 carbohydrate binding modules display conserved specificity but divergent function. *Proc. Natl. Acad. Sci. U. S. A.* **106**, 3065-3070
165. Sainz-Polo, M. A., Valenzuela, S. V., Gonzalez, B., Pastor, F. I., and Sanz-Aparicio, J. (2014) Structural analysis of glucuronoxyran-specific Xyn30D and its attached CBM35 domain gives insights into the role of modularity in specificity. *J. Biol. Chem.* **289**, 31088-31101
166. Liu, Y., Frirdich, E., Taylor, J. A., Chan, A. C., Blair, K. M., Vermeulen, J., Ha, R., Murphy, M. E., Salama, N. R., Gaynor, E. C., and Tanner, M. E. (2016) A Bacterial Cell Shape-Determining Inhibitor. *ACS Chem. Biol.* **11**, 981-991
167. van Teeseling, M. C. F., de Pedro, M. A., and Cava, F. (2017) Determinants of Bacterial Morphology: From Fundamentals to Possibilities for Antimicrobial Targeting. *Front. Microbiol.* **8**, 1264

168. Korlath, J. A., Osterholm, M. T., Judy, L. A., Forfang, J. C., and Robinson, R. A. (1985) A point-source outbreak of campylobacteriosis associated with consumption of raw milk. *J. Infect. Dis.* **152**, 592-596
169. Karlyshev, A. V., and Wren, B. W. (2005) Development and application of an insertional system for gene delivery and expression in *Campylobacter jejuni*. *Appl Environ Microbiol* **71**, 4004-4013
170. Cai, M., Huang, Y., Yang, R., Craigie, R., and Clore, G. M. (2016) A simple and robust protocol for high-yield expression of perdeuterated proteins in *Escherichia coli* grown in shaker flasks. *J. Biomol. NMR* **66**, 85-91
171. Otwinowski, Z., and Minor, W. (1997) Processing of X-ray diffraction data collected in oscillation mode. *Methods Enzymol.* **276**, 307-326
172. Liebschner, D., Afonine, P. V., Baker, M. L., Bunkoczi, G., Chen, V. B., Croll, T. I., Hintze, B., Hung, L. W., Jain, S., McCoy, A. J., Moriarty, N. W., Oeffner, R. D., Poon, B. K., Prisant, M. G., Read, R. J., Richardson, J. S., Richardson, D. C., Sammito, M. D., Sobolev, O. V., Stockwell, D. H., Terwilliger, T. C., Urzhumtsev, A. G., Videau, L. L., Williams, C. J., and Adams, P. D. (2019) Macromolecular structure determination using X-rays, neutrons and electrons: recent developments in Phenix. *Acta Crystallogr D Struct Biol* **75**, 861-877
173. Emsley, P., Lohkamp, B., Scott, W. G., and Cowtan, K. (2010) Features and development of Coot. *Acta Crystallogr. D Biol. Crystallogr.* **66**, 486-501
174. Kabsch, W. (2010) Xds. *Acta Crystallogr. D Biol. Crystallogr.* **66**, 125-132
175. Winn, M. D., Ballard, C. C., Cowtan, K. D., Dodson, E. J., Emsley, P., Evans, P. R., Keegan, R. M., Krissinel, E. B., Leslie, A. G., McCoy, A., McNicholas, S. J., Murshudov, G. N., Pannu, N. S., Potterton, E. A., Powell, H. R., Read, R. J., Vagin, A., and Wilson, K. S. (2011) Overview of the CCP4 suite and current developments. *Acta Crystallogr. D Biol. Crystallogr.* **67**, 235-242
176. Otwinowski, Z., and Minor, W. (1997) [20] Processing of X-ray diffraction data collected in oscillation mode. *Methods Enzymol.* **276**, 307-326
177. Pincus, Z., and Theriot, J. A. (2007) Comparison of quantitative methods for cell-shape analysis. *J Microsc* **227**, 140-156
178. Lescop, E., Schanda, P., and Brutscher, B. (2007) A set of BEST triple-resonance experiments for time-optimized protein resonance assignment. *J. Magn. Reson.* **187**, 163-169
179. Delaglio, F., Grzesiek, S., Vuister, G. W., Zhu, G., Pfeifer, J., and Bax, A. (1995) NMRPipe: a multidimensional spectral processing system based on UNIX pipes. *J. Biomol. NMR* **6**, 277-293
180. Lee, W., Tonelli, M., and Markley, J. L. (2015) NMRFAM-SPARKY: enhanced software for biomolecular NMR spectroscopy. *Bioinformatics* **31**, 1325-1327
181. Bahrami, A., Assadi, A. H., Markley, J. L., and Eghbalnia, H. R. (2009) Probabilistic interaction network of evidence algorithm and its application to complete labeling of peak lists from protein NMR spectroscopy. *PLoS Comput. Biol.* **5**, e1000307
182. Maya-Martinez, R., Alexander, J. A. N., Otten, C. F., Ayala, I., Vollmer, D., Gray, J., Bougault, C. M., Burt, A., Laguri, C., Fonvielle, M., Arthur, M., Strynadka, N. C. J., Vollmer, W., and Simorre, J. P. (2018) Recognition of Peptidoglycan Fragments by the Transpeptidase PBP4 From *Staphylococcus aureus*. *Front. Microbiol.* **9**, 3223

183. Zhang, Z. Y., Clemens, J. C., Schubert, H. L., Stuckey, J. A., Fischer, M. W., Hume, D. M., Saper, M. A., and Dixon, J. E. (1992) Expression, purification, and physicochemical characterization of a recombinant *Yersinia* protein tyrosine phosphatase. *J. Biol. Chem.* **267**, 23759-23766
184. Dominguez, C., Boelens, R., and Bonvin, A. M. (2003) HADDOCK: a protein-protein docking approach based on biochemical or biophysical information. *J. Am. Chem. Soc.* **125**, 1731-1737
185. Meroueh, S. O., Bencze, K. Z., Hesek, D., Lee, M., Fisher, J. F., Stemmler, T. L., and Mobashery, S. (2006) Three-dimensional structure of the bacterial cell wall peptidoglycan. *Proc. Natl. Acad. Sci. U. S. A.* **103**, 4404-4409
186. Schanda, P., Triboulet, S., Laguri, C., Bougault, C. M., Ayala, I., Callon, M., Arthur, M., and Simorre, J. P. (2014) Atomic model of a cell-wall cross-linking enzyme in complex with an intact bacterial peptidoglycan. *J. Am. Chem. Soc.* **136**, 17852-17860
187. Schuttelkopf, A. W., and van Aalten, D. M. (2004) PRODRG: a tool for high-throughput crystallography of protein-ligand complexes. *Acta Crystallogr. D Biol. Crystallogr.* **60**, 1355-1363
188. Brunger, A. T. (2007) Version 1.2 of the Crystallography and NMR system. *Nat. Protoc.* **2**, 2728-2733
189. van Zundert, G. C. P., Rodrigues, J., Trellet, M., Schmitz, C., Kastritis, P. L., Karaca, E., Melquiond, A. S. J., van Dijk, M., de Vries, S. J., and Bonvin, A. (2016) The HADDOCK2.2 Web Server: User-Friendly Integrative Modeling of Biomolecular Complexes. *J. Mol. Biol.* **428**, 720-725
190. de Vries, S. J., and Bonvin, A. M. (2011) CPoRT: a consensus interface predictor and its performance in prediction-driven docking with HADDOCK. *PLoS One* **6**, e17695
191. Soni, A. S., Lin, C. S., Murphy, M. E. P., and Tanner, M. E. (2019) Peptides Containing meso-Oxa-Diaminopimelic Acid as Substrates for the Cell-Shape-Determining Proteases Csd6 and Pgp2. *ChemBioChem* **20**, 1591-1598
192. Krissinel, E., and Henrick, K. (2007) Inference of macromolecular assemblies from crystalline state. *J. Mol. Biol.* **372**, 774-797
193. Holm, L. (2020) DALI and the persistence of protein shape. *Protein Sci.* **29**, 128-140
194. Ashkenazy, H., Erez, E., Martz, E., Pupko, T., and Ben-Tal, N. (2010) ConSurf 2010: calculating evolutionary conservation in sequence and structure of proteins and nucleic acids. *Nucleic Acids Res.* **38**, W529-533
195. Young, N. M., Brisson, J. R., Kelly, J., Watson, D. C., Tessier, L., Lanthier, P. H., Jarrell, H. C., Cadotte, N., St Michael, F., Aberg, E., and Szymanski, C. M. (2002) Structure of the N-linked glycan present on multiple glycoproteins in the Gram-negative bacterium, *Campylobacter jejuni*. *J. Biol. Chem.* **277**, 42530-42539
196. Rocaboy, M., Herman, R., Sauvage, E., Remaut, H., Moonens, K., Terrak, M., Charlier, P., and Kerff, F. (2013) The crystal structure of the cell division amidase AmiC reveals the fold of the AMIN domain, a new peptidoglycan binding domain. *Mol. Microbiol.* **90**, 267-277
197. Mesnage, S., Dellarole, M., Baxter, N. J., Rouget, J. B., Dimitrov, J. D., Wang, N., Fujimoto, Y., Hounslow, A. M., Lacroix-Desmazes, S., Fukase, K., Foster, S. J., and Williamson, M. P. (2014) Molecular basis for bacterial peptidoglycan recognition by LysM domains. *Nat Commun* **5**, 4269

198. Kleckner, I. R., and Foster, M. P. (2011) An introduction to NMR-based approaches for measuring protein dynamics. *Biochim Biophys Acta* **1814**, 942-968
199. Williamson, M. P. (2013) Using chemical shift perturbation to characterise ligand binding. *Prog Nucl Magn Reson Spectrosc* **73**, 1-16
200. Chou, S., Bui, N. K., Russell, A. B., Lexa, K. W., Gardiner, T. E., LeRoux, M., Vollmer, W., and Mougous, J. D. (2012) Structure of a peptidoglycan amidase effector targeted to Gram-negative bacteria by the type VI secretion system. *Cell Rep.* **1**, 656-664
201. Gan, L., Chen, S., and Jensen, G. J. (2008) Molecular organization of Gram-negative peptidoglycan. *Proc. Natl. Acad. Sci. U. S. A.* **105**, 18953-18957
202. Bielnicki, J., Devedjiev, Y., Derewenda, U., Dauter, Z., Joachimiak, A., and Derewenda, Z. S. (2006) *B. subtilis* ykuD protein at 2.0 Å resolution: insights into the structure and function of a novel, ubiquitous family of bacterial enzymes. *Proteins* **62**, 144-151
203. Lecoq, L., Bougault, C., Hugonnet, J. E., Veckerle, C., Pessey, O., Arthur, M., and Simorre, J. P. (2012) Dynamics induced by beta-lactam antibiotics in the active site of *Bacillus subtilis* L,D-transpeptidase. *Structure* **20**, 850-861
204. Magnet, S., Arbeloa, A., Mainardi, J. L., Hugonnet, J. E., Fourgeaud, M., Dubost, L., Marie, A., Delfosse, V., Mayer, C., Rice, L. B., and Arthur, M. (2007) Specificity of L,D-transpeptidases from gram-positive bacteria producing different peptidoglycan chemotypes. *J. Biol. Chem.* **282**, 13151-13159
205. Macheboeuf, P., Contreras-Martel, C., Job, V., Dideberg, O., and Dessen, A. (2006) Penicillin binding proteins: key players in bacterial cell cycle and drug resistance processes. *FEMS Microbiol. Rev.* **30**, 673-691
206. Gumbart, J. C., Beeby, M., Jensen, G. J., and Roux, B. (2014) *Escherichia coli* peptidoglycan structure and mechanics as predicted by atomic-scale simulations. *PLoS Comput. Biol.* **10**, e1003475
207. Kim, S. J., Chang, J., and Singh, M. (2015) Peptidoglycan architecture of Gram-positive bacteria by solid-state NMR. *Biochim Biophys Acta* **1848**, 350-362
208. Wolgemuth, C. W., Inclan, Y. F., Quan, J., Mukherjee, S., Oster, G., and Koehl, M. A. (2005) How to make a spiral bacterium. *Phys. Biol.* **2**, 189-199
209. Huang, K. C., Mukhopadhyay, R., Wen, B., Gitai, Z., and Wingreen, N. S. (2008) Cell shape and cell-wall organization in Gram-negative bacteria. *Proc. Natl. Acad. Sci. U. S. A.* **105**, 19282-19287
210. Terwilliger, T. C., Grosse-Kunstleve, R. W., Afonine, P. V., Moriarty, N. W., Zwart, P. H., Hung, L. W., Read, R. J., and Adams, P. D. (2008) Iterative model building, structure refinement and density modification with the PHENIX AutoBuild wizard. *Acta Crystallogr. D Biol. Crystallogr.* **64**, 61-69
211. Suzuki, N., Fujimoto, Z., Kim, Y. M., Momma, M., Kishine, N., Suzuki, R., Suzuki, S., Kitamura, S., Kobayashi, M., Kimura, A., and Funane, K. (2014) Structural elucidation of the cyclization mechanism of alpha-1,6-glucan by *Bacillus circulans* T-3040 cycloisomaltooligosaccharide glucanotransferase. *J. Biol. Chem.* **289**, 12040-12051
212. Couturier, M., Roussel, A., Rosengren, A., Leone, P., Stalbrand, H., and Berrin, J. G. (2013) Structural and biochemical analyses of glycoside hydrolase families 5 and 26

- beta-(1,4)-mannanases from *Podospora anserina* reveal differences upon manno-oligosaccharide catalysis. *J. Biol. Chem.* **288**, 14624-14635
213. Veyrier, F. J., Williams, A. H., Mesnage, S., Schmitt, C., Taha, M. K., and Boneca, I. G. (2013) De-O-acetylation of peptidoglycan regulates glycan chain extension and affects in vivo survival of *Neisseria meningitidis*. *Mol. Microbiol.* **87**, 1100-1112
214. Williams, A. H., Wheeler, R., Deghmane, A. E., Santecchia, I., Schaub, R. E., Hicham, S., Moya Nilges, M., Malosse, C., Chamot-Rooke, J., Haouz, A., Dillard, J. P., Robins, W. P., Taha, M. K., and Gomperts Boneca, I. (2020) Defective lytic transglycosylase disrupts cell morphogenesis by hindering cell wall de-O-acetylation in *Neisseria meningitidis*. *Elife* **9**
215. Vijayaraghavan, J., Kumar, V., Krishnan, N. P., Kaufhold, R. T., Zeng, X., Lin, J., and van den Akker, F. (2018) Structural studies and molecular dynamics simulations suggest a processive mechanism of exolytic lytic transglycosylase from *Campylobacter jejuni*. *PLoS One* **13**, e0197136
216. Pfeffer, J. M., and Clarke, A. J. (2012) Identification of the first known inhibitors of O-acetylpeptidoglycan esterase: a potential new antibacterial target. *ChemBioChem* **13**, 722-731
217. Bougault, C., Ayala, I., Vollmer, W., Simorre, J. P., and Schanda, P. (2019) Studying intact bacterial peptidoglycan by proton-detected NMR spectroscopy at 100kHz MAS frequency. *J. Struct. Biol.* **206**, 66-72
218. Paraskevopoulou, V., and Falcone, F. H. (2018) Polyionic Tags as Enhancers of Protein Solubility in Recombinant Protein Expression. *Microorganisms* **6**
219. Los, G. V., Encell, L. P., McDougall, M. G., Hartzell, D. D., Karassina, N., Zimprich, C., Wood, M. G., Learish, R., Ohana, R. F., Urh, M., Simpson, D., Mendez, J., Zimmerman, K., Otto, P., Vidugiris, G., Zhu, J., Darzins, A., Klaubert, D. H., Bulleit, R. F., and Wood, K. V. (2008) HaloTag: a novel protein labeling technology for cell imaging and protein analysis. *ACS Chem. Biol.* **3**, 373-382
220. Yahashiri, A., Jorgenson, M. A., and Weiss, D. S. (2015) Bacterial SPOR domains are recruited to septal peptidoglycan by binding to glycan strands that lack stem peptides. *Proc. Natl. Acad. Sci. U. S. A.* **112**, 11347-11352
221. Alcorlo, M., Dik, D. A., De Benedetti, S., Mahasenan, K. V., Lee, M., Dominguez-Gil, T., Hesek, D., Lastochkin, E., Lopez, D., Boggess, B., Mobashery, S., and Hermoso, J. A. (2019) Structural basis of denuded glycan recognition by SPOR domains in bacterial cell division. *Nat Commun* **10**, 5567
222. Kuru, E., Radkov, A., Meng, X., Egan, A., Alvarez, L., Dowson, A., Booher, G., Breukink, E., Roper, D. I., Cava, F., Vollmer, W., Brun, Y., and VanNieuwenhze, M. S. (2019) Mechanisms of Incorporation for D-Amino Acid Probes That Target Peptidoglycan Biosynthesis. *ACS Chem. Biol.* **14**, 2745-2756
223. Sheng-Huei Lin, C., Chan, A. C. K., Vermeulen, J., Brockerman, J., Soni, A. S., Tanner, M. E., Gaynor, E. C., McIntosh, L. P., Simorre, J. P., and Murphy, M. E. P. (2021) Peptidoglycan binding by a pocket on the accessory NTF2-domain of Pgp2 directs helical cell shape of *Campylobacter jejuni*. *J. Biol. Chem.*, 100528
224. Nita-Lazar, M., Wacker, M., Schegg, B., Amber, S., and Aeby, M. (2005) The N-X-S/T consensus sequence is required but not sufficient for bacterial N-linked protein glycosylation. *Glycobiology* **15**, 361-367

225. Kowarik, M., Young, N. M., Numao, S., Schulz, B. L., Hug, I., Callewaert, N., Mills, D. C., Watson, D. C., Hernandez, M., Kelly, J. F., Wacker, M., and Aeby, M. (2006) Definition of the bacterial N-glycosylation site consensus sequence. *EMBO J.* **25**, 1957-1966
226. Cain, J. A., Dale, A. L., Sumer-Bayraktar, Z., Solis, N., and Cordwell, S. J. (2020) Identifying the targets and functions of N-linked protein glycosylation in *Campylobacter jejuni*. *Mol Omics* **16**, 287-304
227. Abouelhadid, S., North, S. J., Hitchin, P., Vohra, P., Chintoan-Uta, C., Stevens, M., Dell, A., Cuccui, J., and Wren, B. W. (2019) Quantitative Analyses Reveal Novel Roles for N-Glycosylation in a Major Enteric Bacterial Pathogen. *mBio* **10**(2), e00297-19
228. Russell, A. B., Singh, P., Brittnacher, M., Bui, N. K., Hood, R. D., Carl, M. A., Agnello, D. M., Schwarz, S., Goodlett, D. R., Vollmer, W., and Mougous, J. D. (2012) A widespread bacterial type VI secretion effector superfamily identified using a heuristic approach. *Cell Host Microbe* **11**, 538-549
229. Lee, M., Hesek, D., Dik, D. A., Fishovitz, J., Lastochkin, E., Boggess, B., Fisher, J. F., and Mobashery, S. (2017) From Genome to Proteome to Elucidation of Reactions for All Eleven Known Lytic Transglycosylases from *Pseudomonas aeruginosa*. *Angew. Chem. Int. Ed. Engl.* **56**, 2735-2739
230. Chaput, C., Labigne, A., and Boneca, I. G. (2007) Characterization of *Helicobacter pylori* lytic transglycosylases Slt and MltD. *J. Bacteriol.* **189**, 422-429
231. Jorgenson, M. A., Chen, Y., Yahashiri, A., Popham, D. L., and Weiss, D. S. (2014) The bacterial septal ring protein RlpA is a lytic transglycosylase that contributes to rod shape and daughter cell separation in *Pseudomonas aeruginosa*. *Mol. Microbiol.* **93**, 113-128